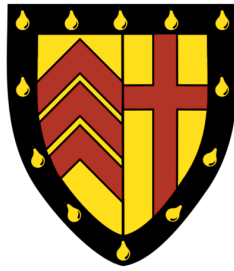


Controlling Viscous Fingering



Tim H. Beeson-Jones

Supervisor: Prof. Andrew W. Woods

BP Institute

University of Cambridge

This dissertation is submitted for the degree of

Doctor of Philosophy

Clare College

April 2018

To Mum, Dad and Jess.

Declaration

I hereby declare that except where specific reference is made to the work of others, the contents of this dissertation are original and have not been submitted in whole or in part for consideration for any other degree or qualification in this, or any other university. This dissertation is my own work and contains nothing which is the outcome of work done in collaboration with others, except as specified in the text and Acknowledgements. This dissertation contains fewer than 40,000 words including appendices, bibliography, footnotes, tables and equations and has fewer than 50 figures.

Tim Beeson-Jones

July 2017

“Climate change presents a unique challenge for economics: it is the greatest and widest-ranging market failure ever seen.”

Sir Howard Stern (2006), *Stern Review: The Economics of Climate Change*

Acknowledgements

First and foremost, I thank my supervisor Andy Woods. I am very grateful for the patience, support and guidance he has given me during the course of my studies at the BPI. I hope I have learned something of his approaches to posing problems, solving problems and communicating the results, approaches which are both unique and world class. I also hope his humour and enthusiasm for science will remain with me during my career.

The people at the BPI have created a wonderful community for which I shall soon feel nostalgic. I am very appreciative of Lotty Gladstone's efforts towards managing and keeping safe the brilliant flow labs and also her guidance with experiments. Andrew Pluck's ability to make (fix) the things I've needed (broken) has been crucial. Chris Richardson and Patrick Welche have been incredibly helpful in their provision of a reliable computer system and computing assistance. Finally, I am very grateful to Catherine Pearson who keeps the BPI a well-oiled machine!

As for my colleagues, I thank Alex Evans, Peter Dudfield, Marcus Horsley, Ed Hinton and Neeraja Bhamidipati for their crucial mathematical assistance, Finn Box for sharing his image processing expertise, Caren Lacy and Sefano Rocco for their help in the lab and Martin Lippert, Jeffrey Poon and Richard Alloway for their camaraderie.

As for the wider university, I am extremely grateful to all those at Clare College that have made it my home close to my home for eight short years. It is a beautiful college. In particular, I would like to thank Phil and all the porters for looking out for us students and Lee and Bonna for keeping us well fed. Also, I am very grateful to

Steve & Sarah Morgan for their tireless efforts at the UPC and all the guys at CUSSC for showing me how to ski.

There has not been a dull moment amongst my marvellous friends. I am profoundly grateful to my long-suffering housemates Andy Wedlake, Will Wynn-Mayow, AP Stafford, Alex Fokas, Ben Stretch and Fred Dudbridge but most of all to the longest sufferer Lois Salem, who has endured 5 years.

Finally, I thank my family for their immense love and support.

Abstract

Viscous fingering occurs when one fluid displaces another fluid of a greater viscosity in a porous medium or a Hele-Shaw cell. Linear stability analysis is used to predict methods of suppressing instability. Then, experiments in which nonlinear growth dominates pattern formation are analysed to explore the nonlinear impact of strategies of suppressing finger growth.

Often, chemical treatment fluid is injected into oil reservoirs in order to prevent sand production. This treatment fluid is usually followed by water injection to clean up the well. We explore the potential for viscous instability of the interface between the treatment fluid and the water, and also the treatment fluid and the oil, as a function of the volume of treatment fluid and the injection rate and viscosity ratios of the different fluids. For a given volume of treatment fluid and a given injection rate, we find the optimal viscosity of the treatment fluid to minimise the viscous instability. In the case of axisymmetric injection, the stabilisation associated with the azimuthal stretching of modes leads to a further constraint on the optimisation of the viscosity.

In the case of oil production, polymers may be added to the displacing water in order to reduce adverse viscosity gradients. We also explore the case in which these polymers have a time-dependent viscosity, for example through the slow release from encapsulant. We calculate the injection flow rate profile that minimises the final amplitude of instability in both rectilinear and axisymmetric geometries. In a development of the model, we repeat the calculation for a shear-thinning rheology.

Finally, experiments are analysed in which the nonlinear growth of viscous fingers develops to test the influence of different injection profiles on the development of insta-

bility. Diffusion Limited Aggregation (DLA) simulations are performed for comparison. In all cases, the evolving pattern has a saturation distribution, with an inner zone in which the fingers are static and an outer zone in which the fingers advance and grow. In the very centre of the viscous fingering patterns, there is a small fully-saturated region. In the experiments, the mass distribution in the inner zone varies with radius as a power law which relates to the fractal dimension for the analogue DLA simulations. In the outer region the saturation decreases linearly with radius. The radius of the inner frozen zone is approximately $2/3$ of the outer radius in the cases of DLA and – after a period of evolution – the viscous fingering experiments. This allows the radial extents of the inner and outer zones to be predicted. The ratio of each radius to the extent of the fully-saturated region is independent of the injection profile and corresponds to values for DLA.

Publications

This thesis contains two published studies as follows:

- Chapter 2: Beeson-Jones, T. H. and Woods, A. W. (2015). On the selection of viscosity to suppress the Saffman Taylor instability in a radially spreading annulus. *Journal of Fluid Mechanics*, 782:127–143.
- Chapter 3: Beeson-Jones, T. H. and Woods, A. W. (2017). Control of viscous instability by variation of injection rate in a fluid with time-dependent rheology. *Journal of Fluid Mechanics*, 829:214–235.

“Knowledge is Porridge.”

Stewart Pearson, *The Thick of It*

Table of contents

List of figures	xvii
List of tables	xxvii
1 Introduction	1
1.1 Motivation	1
1.2 Linear Stability Analysis: Predicting Interfacial Control	4
1.3 Nonlinear Growth	9
2 Annular Saffman-Taylor Suppression	13
2.1 Summary	13
2.2 Introduction	14
2.3 Single-Interface Stability: Treatment Injection Phase	17
2.3.1 Formulation	17
2.3.2 Absolute Stability of mode n	18
2.3.3 Dynamic Stability	19
2.3.4 Single-Interface Control	20
2.4 Dual-Interface Stability: Post-Treatment Fluid Injection Phase	22
2.4.1 Formulation	22
2.4.2 Absolute Stability of Mode n	25
2.4.3 Dynamic Stability	30
2.5 Control Strategy	32
2.6 Conclusions	37

3	Viscous instability with time-dependent rheology	39
3.1	Summary	39
3.2	Introduction	40
3.3	Newtonian Flow in a Rectilinear Geometry	44
3.3.1	Formulation	44
3.3.2	Effect of a Gradual Increase in Viscosity	46
3.4	Injection from a point source	51
3.4.1	The Constant Viscosity Regime	52
3.4.2	Effect of a Gradual Increase in Viscosity	60
3.5	Injection of a Shear-Thinning Fluid	63
3.6	Discussion	69
4	Dynamics of Fractal Growth	71
4.1	Summary	71
4.2	Introduction	72
4.2.1	Viscous Fingering and the Confinement of Growth	72
4.2.2	Fractal Objects, Diffusion Limited Aggregation and the Determination of the Fractal Dimension	73
4.2.3	The Fractal Dimension of Viscous Fingering Patterns	75
4.2.4	Chapter Outline	78
4.3	Experiments	79
4.3.1	Apparatus, Experimental Conditions and Protocol	79
4.4	Results	80
4.4.1	Measured Flow Rates	80
4.4.2	VF Pattern Formation	82
4.4.3	An Empirical Saturation Model	83
4.4.4	Comparison to Diffusion Limited Aggregation	93
4.5	Discussion	96
4.6	Conclusions	102
4.7	Appendix	104

5

Conclusions

105

5.1

Main contributions

105

5.2

Further Work

108

References

111

List of figures

1.1	The displacement of stable displacement of oil by water and the unstable displacement of water by oil in a Hele-Shaw cell five-spot pattern. From Mungan (1971).	3
1.2	The displacement of glycerol by air in a rectilinear Hele-Shaw cell at the onset of instability (a) and after the development of a dominant finger (b). From Saffman and Taylor (1958).	10
2.1	Dual-interface variable definitions. The reservoir fluid (fluid 3) and post-treatment fluid (fluid 1) are separated by an annulus of treatment fluid (fluid 2). The leading and trailing interfacial base states are at radii R_2 and R_1 respectively, with perturbation amplitudes $B_n(t)$ and $A_n(t)$	17
2.2	Variation of the maximum value of P at which the labelled mode, $n = 2, \dots, 6$, becomes absolutely stable as a function of V . For a given mode n , then for values of P smaller than this maximum, all modes n' such that $n' < n$ are absolutely stable.	19

- 2.3 Stability diagram for a radial displacement flow with $V = 0.1$, showing the highest $\Gamma(n) = Q_n^*(R_2^*)R_2^*$ for which the flow is stable to perturbations of mode n (dashed lines) plotted as a function of the ratio of the viscosity difference between the reservoir fluid and the treatment fluid, to the viscosity difference between the post-treatment fluid and the reservoir fluid. Solid line represents the locus of stability for all modes $\Gamma(n_{\min})$ as a function of P . If a more viscous displacing fluid is used, higher flow rates are permitted. 21
- 2.4 The non-dimensional difference in viscosity across the leading interface, P , at which the trailing (dashed) and leading (solid) interfaces become absolutely stable to the given mode as a function of the bounding viscosity ratio, V for the limit $\hat{R} \rightarrow 0$. In (a) we show which interface is absolutely stable for mode 2. In regions (i) and (iii) the leading or trailing interface alone is respectively absolutely stable, whereas in region (ii) both interfaces are absolutely stable and in region (iv) both interfaces impose a flow rate limitation for stability. In (b) we show how this extends to higher modes. 27
- 2.5 The critical values of the non-dimensional leading viscosity jump, P , for absolute stability as a function of \hat{R} for $V = 0.3$. In regions (ii) and (iii) modes 2 and 3 are absolutely stable respectively. As time and hence \hat{R} increase, the annulus thins and these lines converge. As such, absolute stability is transient for modes 2 and 3 for this value of V 28

2.6	The critical values of the non-dimensional difference in viscosity across the leading interface, P , at which the dual-interface system is absolutely stable as a function of V for modes 2 (solid lines) and 3 (broken lines) for three values of \hat{R} . The $\hat{R} = 0$ curves can be recognised from figure 2.4 with cusps at $V_{\text{lower}}(n)$. As \hat{R} increases, the annulus thins and the stability tends to that of a single interface in a system in which the post-treatment fluid displaces the reservoir fluid, with a vertical boundary at $V_{\text{upper}}(n)$	29
-----	--	----

- 2.7 Variation of the maximum flow rate, $\Gamma = QR_2$, for stability of the system to all modes (thick solid line) as a function of the non-dimensional leading viscosity jump, P , for $V = 0.1$ and for two values of \hat{R} , $\hat{R} = 0.1, 0.5$. Also shown in the figures are a series of thin lines on which $\text{Det}(\mathbf{M}) = 0$ for each of modes 2,...,6. In (a), for $n > 2$, there are two dashed lines for each mode: one of these lines has relatively small values of Γ for small P and Γ then increases monotonically with P , whilst the other has relatively small values of Γ for large P and Γ then decreases monotonically with P . The point of intersection of these two solution branches corresponds to the point $\text{Det}(\mathbf{M}) = 0$ and $\text{Tr}(\mathbf{M}) = 0$. However, for $n = 2$, there are two non-intersecting lines for which $\text{Det}(\mathbf{M}) = 0$ and these are shown as solid thin lines. The lower branch corresponds to the maximum value of Γ for which all perturbations of mode 2 are stable, while the upper branch corresponds to the minimum value of Γ for which all perturbations of mode 2 are unstable. In (b), we show solutions for $\text{Det}(\mathbf{M}) = 0$ for modes $n = 2, \dots, 5$ as thin solid lines, and for each such mode, there is a lower branch on which $\text{Tr}(\mathbf{M}) < 0$ and an upper branch on which $\text{Tr}(\mathbf{M}) > 0$, and these branches do not intersect. Note, however, that owing to the finite vertical scale, the upper branch of mode 2 does not appear in the graph. Also shown are two dashed thin lines, corresponding to $\text{Det}(\mathbf{M}) = 0$ for mode 6. The value of Γ on these two dashed lines increase and decrease monotonically with P , respectively, and their point of intersection again corresponds to the point $\text{Det}(\mathbf{M}) = 0$ and $\text{Tr}(\mathbf{M}) = 0$ 33
- 2.8 The mode that requires the lowest flow rate to remain stable (n_{\min}) as a function of P for $V = 0.1$ and $\hat{R} = 0.1, 0.3, 0.5$. As \hat{R} increases coupling causes lower modes to impose the strictest limit on flow rate. There are some small spikes in n_{\min} when the respective range of values of P is narrow. 34

- 2.9 (a) The maximum stable $\Gamma = QR_2$ as a function of P for a series of increasing R_2 where $V = 0.1$. The post-treatment fluid is injected at $R_2 = 5$. As such, for $1 \leq R_2 \leq 5$ the stability of the system is bounded by the single-interface analysis (broken line). Subsequently, the stability of the trailing interface must be considered and the stability is bounded by the dual-interface analysis (solid lines). (b) The maximum Q for stability varying with R_2 for the cases A, B and C in (a). 36
- 2.10 Time to sweep to $R_2 = 10$ scaled with the time taken for a single interface in which post-treatment fluid displaces the original reservoir fluid for a series of increasing S as a function of the ratio of the leading viscosity jump to the global viscosity jump. The optimum viscosity choice balances the adverse viscosity ratios at the leading and trailing interfaces. 37
- 3.1 Left column: $\theta = 1$ (slow gelling). Right column: $\theta = 10$ (rapid gelling). Top row: viscosity ratio profiles with parameters θ , $V_0 = 0.01$ and $V_f = 0.9$ (primary axis) and the optimal velocity profiles (secondary axis). Middle row: the evolution of $\sqrt{\tau}k_{\max}$ for the optimal (dashed lines) and constant (solid lines) flow rate profiles. Bottom row: the evolution of $\sqrt{\tau}\sigma$ 49
- 3.2 (a) The final amplitude of perturbations of wavenumber k for the viscosity invariant case ($\theta = 0$, grey) and a gelling case ($\theta = 1$) for a constant flow rate (solid line) and the optimal flow rate (broken line). (b) The final maximum amplitudes varying as a function of θ for $V_f = 0.9$. (c) The ratio of these two final amplitudes as a function of θ for a series of V_f . (d) The effect of increasing V_0 for a series of V_f and $\theta = 2$. (e) A contour plot of the final amplitude ratio varying with τ and θ for $V_0 = 0.01$ and $V_f = 0.9$ 50

- 3.3 The flow rate, $Q^*(t)$, that minimises $\int_0^1 \sigma_{\max} dt$ for $\Lambda = \Lambda^\dagger$ (dashed line), $\Lambda = 3\Lambda^\dagger$ and $\Lambda = 10\Lambda^\dagger$ (solid lines) and $\Lambda = 100\Lambda^\dagger$ (dashed-dotted line) while $R_0 = 0.1$ 54
- 3.4 (a) The evolution of the upper bound of growth rate, σ_{\max}^* , for $V = 0$ (broken lines), $V = 0.1$ (solid lines), $R_0 = 0.2$ and a series of values of $\frac{\Lambda}{\Lambda^\dagger}$ that increases from the bottom of the figure upwards. (b) A regime diagram for the conditions $\sigma_{\max}^* < 0 \forall t$ (broken lines; region S) and $\sigma_{\max}^* > 0 \forall t$ (solid lines, region U) for a series of values of V increasing from left to right (as labelled). 55
- 3.5 (a) The evolution of the most unstable mode n_{\max} for $R_0 = 0.1$ and a series of $\frac{\Lambda}{\Lambda^\dagger}$ that increases from the bottom of the page upward. (b-g) The growth rate of discrete modes n for a constant injection rate (2nd row) and the optimal injection rate (3rd row) for $V = 0$, $R_0 = 0.1$ and $\Lambda = 3\Lambda^\dagger$ (left column), $\Lambda = 10\Lambda^\dagger$ (centre column) and $\Lambda = 100\Lambda^\dagger$ (right column). The mode number increases from the LHS to the RHS of the figures. (h-j) The amplitude of perturbations following the optimal injection rate. Initially, the lowest modes have the largest amplitude. Mode 2 (11) is highlighted with thick line in orange (purple). The growth-rate bound derived from treating n as a continuous variable is shown as the thick black line. 59
- 3.6 The final amplitude varying with $\frac{\Lambda}{\Lambda^\dagger}$ for $V = 0$, $R_0 = 0.1$ for constant injection (solid lines) and optimal injection (broken lines) computed with discrete modes (black) and a continuous series of modes (grey). . . 60
- 3.7 The critical value of Λ_0 , above which the system is always unstable for the gelling case in which $V_0 = 0.3$ and $V_f = 0.5$. A series of values of gelling rate, θ , is shown. 61

- 3.8 The optimal flow rate, $Q^*(t)$, for a series of different gelling rates θ for $R_0 = 0.35$, $V_0 = 0$, $\Lambda_f = 1250$ and $V_f = 0.9$ found using (3.27) (solid lines) and the invariant viscosity case (broken line). In (a), the timescale of viscosity change compared to the flow is small, whereas in (b) it is large. In (a) the numerical solution to (3.19) is shown (crosses). 62
- 3.9 (a) The final amplitude of each mode n for the viscosity invariant case ($\theta = 0$, grey lines), for a constant flow rate (solid lines) and the equivalent optimal flow rate (broken lines) where $V_0 = 0$, $V_f = 0.5$, $\Lambda_f = 1250$ and $R_0 = 0.35$. A gelling example is also shown ($\theta = 1$, black). (b) The variation of both maximum amplitudes with θ . (c) The ratio of the constant to optimal injection final amplitude plotted against θ for two values of Λ_f 64
- 3.10 Evolution of amplitudes for a shear-thinning fluid in which the apparent viscosity ratio varies according to $V_0 = 0.01$, $V_f = 0.9$ and $\theta = 10$ for constant injection ($U = 1$; solid lines) and a series of values of m that decreases from the Newtonian case ($m = 1$; black) at bottom of the figure upwards: $m = 0.99$ (blue), $m = 0.95$ (red) and $m = 0.78$ (yellow). Also included are the evolution of amplitudes in the case of optimal injection (*cf.* figure 3.11(a) broken lines). 67
- 3.11 Injection with $V_f = 0.9$. (a) Optimal injection flow rate profiles. (b) Variation of the final amplitude with gelling speed parameter θ for constant injection (solid lines) and optimal injection (broken lines). The values of m in the cases of shear thinning correspond to those in figure 3.10. 68
- 4.1 The evolution of the pattern area, A 82
- 4.2 VF pattern development time series for the experiment keys and time intervals, δt , as shown in the captions. Scales in [cm]. 84

4.3	The evolution of saturation for three different examples of inlet condition with the model (4.5) fitted (black lines). The time series are evenly-spaced in time and are shown starting at an initial time t_i at intervals Δt , with these values as shown in the captions as $(t_i, \Delta t)$. . .	85
4.4	Schematic of the saturation profile.	85
4.5	The final saturation profile across experiments. In all figures, the broken line is (4.4) with $\mathcal{D} = 1.70$	87
4.6	Variation of the fitting parameter R_b with \bar{C} . The experiment key number increases from left to right.	88
4.7	The evolution of the ratio R_{tip}/R_{fr} varying with R_{tip}/b for the injection profiles as labelled (<i>c.f.</i> figure 4.5 for legend keys).	89
4.8	The evolution of the radii R_{tip} (left column) and R_{fr} (right column). Top row: constant injection, middle row: constant pressure, bottom row: ramped injection (<i>c.f.</i> figure 4.5 for legend keys; the experiment key number increases from bottom left to top right).	92
4.9	(a) A DLA cluster of 10^5 particles. (b) The radial saturation profiles of DLA clusters of size ranging from 10^5 to 10^6 particles in ten equal increments. The simulation to produce each cluster size was repeated seven times, and that shown is the mean saturation of all repeats. . . .	94
4.10	Evolution of (a) the ratio R_{tip}/R_{fr} , (b) R_{tip} and (c) R_{fr} as a function of the number of particles released.	95
4.11	Comparison of the radii R_{in} (a) and R_{tip} (b) for the viscous fingering experiments (points) and DLA (broken lines).	97
4.12	The evolution of U_{tip} [cm/s] (left axis) and Ca (right axis). (a) Praud and Swinney (2005) experiments (bottom to top: P1 to P3). (b) Constant flow rate experiments C1-C3.	99
4.13	Saturation profiles for the final patterns of May and Maher (1989) (+), Thomé et al. (1989) (o), and Lajeunesse and Couder (2000) (their fig. 17(a) - (boxes)) and (fig 17.(b) - (diamonds)).	100

4.14 The box counting algorithm applied to different regions of two final VF patterns. From the top series to the bottom: Ov = Overall, Sc = Screened (frozen) and Ac = Active (growth).	101
--	-----

List of tables

4.1	Experimental setup. Experiments C1-C3 and R1-R3 were performed by the authors of this chapter, whereas P1-P3 were performed by Praud and Swinney (2005) and C4 and R4 were performed by Bischofberger et al. (2015).	80
4.2	Measured area and flow rate.	81
4.3	The error in the frozen region, $RMSE_{fr}$, and shape parameters of the model.	90
4.4	The image processing MATLAB functions used and a brief description thereof.	104

Chapter 1

Introduction

The theme of this thesis is the control of viscous fingering, the need for which is outlined in §1.1. In §1.2 we introduce the classic theoretical treatment of viscous fingering: the linear stability analysis. We discuss previous work that has used linear stability analysis as a theoretical tool to develop methods of controlling viscous fingering and in doing so we outline **chapters two** and **three** of this thesis, which propose novel control methods. Then, in §1.3, we describe new experiments to explore the nonlinear development of viscous fingering and outline **chapter four**, in which we develop a new empirical model to describe the patterns that form during this nonlinear growth. This provides insight into the efficacy of the control methods developed in chapters 2 and 3 for the fully nonlinear growth.

1.1 Motivation

When one fluid is displaced by another in a porous medium the interface between the fluids may be stable or unstable depending on their respective mobilities in the medium. In a homogeneous medium, if a less viscous fluid displaces a more viscous fluid then the interface is subject to the viscous fingering instability, whereby a series of fingers of the less viscous fluid penetrates into the fluid being displaced.

Viscous fingering can be problematic. In the oil and gas industry the process of waterflooding involves the injection of water into the oil reservoir in order to drive the oil towards the production well and to maintain the reservoir pressure. Upon water reaching the production well, an event known as ‘breakthrough’, further injected water may follow the path of least resistance along a channel of water, rather than continue to displace the oil towards the production well. Viscous fingering may cause this channel to form more readily, reducing the time until breakthrough and causing larger regions of uncaptured oil to be left in the reservoir (Lake, 1989). This is illustrated in figure 1.1, which shows the immiscible displacement of one fluid by another at the time that the displacing fluid breaks through to the production well. The experiment was carried out in a thin gap between two parallel plates, effectively behaving as a two-dimensional flow. The flow geometry is the ‘five spot’ pattern and there is no flow across boundaries. Figure 1.1(a) illustrates the displacement of water by a viscous oil from the injection well to the production well. Since the oil is more viscous, the displacement is not subject to viscous fingering and the majority of the water is displaced out of the cell at the time of breakthrough. However, some water does remain since the fastest flow is down the centreline. In contrast, figure 1.1(b) illustrates the opposite case: the interface is unstable and fingers of water penetrate through the oil zone. A large finger in the centreline of the flow extends to the production well, causing breakthrough before the majority of the oil can be swept.

Other difficulties can arise from viscous fingering in the oil and gas industry. If the rock surrounding the injection well, where the fluid pressure may be large, is poorly consolidated then sand can be dislodged from the rock at this site. This sand may then travel with the fluids to the production well and erode the well and associated machinery. This process is called ‘sand production’ and can be very destructive. To avoid sand production, a chemical treatment fluid can be deployed to consolidate the rock close to the injection well. One drawback of chemical treatment is that it might block pore throats in the immediate vicinity of the injection well (Paraskeva et al., 2000). Thus, following the chemical treatment a second fluid, that cleans up the

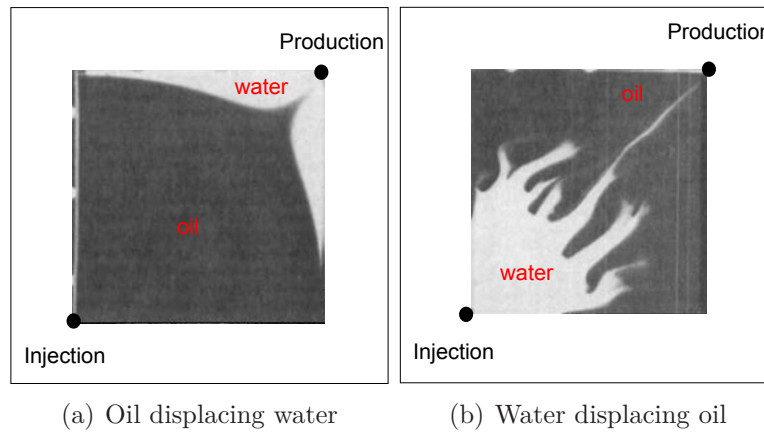


Fig. 1.1 The displacement of stable displacement of oil by water and the unstable displacement of water by oil in a Hele-Shaw cell five-spot pattern. From Mungan (1971).

well and displaces the chemical treatment away from the well, may be injected. The chemical treatment then forms an annulus that travels through the reservoir. In the presence of adverse viscosity ratios the annulus of fluid can break up due to viscous fingering (Cardoso and Woods, 1995). Talaghat et al. (2009) describe such fingering as a problem during sand consolidation that should be mitigated in the minimum amount of time since the well is out of production during chemical treatment.

Research interest is not limited to the oil and gas industry. Other examples of where viscous fingering is undesirable are catalyst regeneration in fixed bed reactors, filtration processes and sugar refining (Hill, 1952; Homsy, 1987). In other contexts, the instability may be exploited, for example to enhance fluid-fluid mixing (Jha et al., 2011). Turning to natural phenomena, the degree of mixing of fluids of different viscosity may be a factor that controls the composition of magma during its ascent in the conduit of a volcano (McBirney, 1984). In biology, Lubkin and Murray (1995) used a model from the field of viscous fingering to describe the early development of lung tissue. More recently, Callan-Jones et al. (2008) noted the similarity of the growth of a particular type of biological cell fragment and viscous fingering. Viscous fingering is also used as an archetype of interfacial instability that leads to pattern formation

(Casademunt, 2004). The subject is not short of applications and has proven to be a rich area of scientific research over the past half century.

1.2 Linear Stability Analysis: Predicting Interfacial Control

As a preface to introducing the scientific works upon which we have built, we will first introduce a simplifying analogue to porous media flow. The flow of fluid in a porous medium is governed by Darcy's law, which states that the velocity field is proportional to pressure gradients. This is also true of flow in the narrow gap between two parallel plates. This experimental device is called a Hele-Shaw cell (Hele-Shaw, 1898). Since the gap is narrow, motion perpendicular to the plates may be neglected and gap-averaged quantities are used. The equivalence is imperfect for two-phase flow since the Hele-Shaw model neglects pore-scale dispersive capillary forces that affect the propagation of the interface as well as other two-phase flow effects (Perkins and Johnston, 1969). In a porous medium, surface tension only acts on the scale of the pores. This force is not modelled in the Hele-Shaw geometry (Homsy, 1987). Therefore, there is a limitation on the validity of the relation of our analysis to a porous medium because the planform curvature we describe, which acts to select the fastest growing wavelength of instability, would not be present. The conclusions reached in later chapters are strictly only valid for Hele-Shaw flows, however, an effective capillary pressure, which depends on the proportion of each fluid phase in pore, does exist and acts to cut-off small wavelengths of instability in porous media (Woods, 2015). Nonetheless, the Hele-Shaw cell is a useful simplifying tool that provides insight into viscous fingering phenomena and is interesting in its own right (Homsy, 1987). We will now introduce our research in the context of the literature, which is mostly based on Hele-Shaw flow.

Whilst the criterion for stability was first derived by Hill (1952), the viscous fingering instability is often referred to by the study that first derived the dispersion

relation. Saffman and Taylor (1958) performed a linear stability analysis (LSA) of the interface between two immiscible fluids of differing viscosity in a rectilinear geometry. If the displaced fluid is more viscous then, according to Hele-Shaw flow, the pressure gradient in the longitudinal direction is steeper. Thus, a forward perturbation of the less viscous fluid is surrounded by lower pressure fluid and growth is encouraged. It was shown by Saffman and Taylor (1958) that a fastest growing wavelength exists because long wavelength perturbations are more stable and the large curvature of short wavelength perturbations stabilizes those perturbations through the action of interfacial tension, which was included in their study using a formulation proposed by Chouke et al. (1959).

Following this work, Bataille (1968) extended the linear stability theory to the more complex case of the flow of a less viscous fluid injected into a more viscous fluid from a point source. The complexity arises from the evolution of the base state. Furthermore, the wavenumber of the circular modes is quantised. At early stages in the flow the curvature may be sufficiently large that interfacial tension stabilizes all azimuthal modes. In the experiments presented by Paterson (1981) the fingers featured the azimuthal wavelength predicted by linear stability analysis at the onset of instability. However, Maxworthy (1989) found that this prediction of wavelength is only valid for small capillary numbers, and for larger capillary numbers the wavelength that is selected is larger than that predicted by Paterson (1981). Paterson (1981) adopted the simplest formulation for the interfacial pressure jump, which was introduced by Chouke et al. (1959) and Saffman and Taylor (1958). This condition only accounts for interfacial tension as a cause for the pressure jump at the interface. In fact, Dias and Miranda (2013b) have shown that an accurate prediction of the selected wavelength can be made for all capillary numbers if the pressure jump condition also includes: i) the effect of a thin wetting film that trails behind the interface (Park and Homsy, 1984) and ii) the viscous stresses at the interface (Kim et al., 2009). These developments demonstrate that linear stability theory can accurately predict the wavelength of instability at the onset of instability. In order to simplify the analysis, we neglect the contribution to

the pressure jump that originates with normal stresses and ignore the viscous film that trails behind the interface. Strictly, the pressure jump condition we use is only valid under conditions where the wavelength of instability is much greater than the gap width of the Hele-Shaw cell and the displacing fluid is perfectly wetting. We will now discuss the approaches to controlling the instability that have been developed, which have involved: modifying the geometry of the system; modifying properties of the fluids; and varying the injection flow rate.

It is possible to alter the stability by modifying properties of the Hele-Shaw cell such that additional terms are introduced to the growth rate equation. Al-Housseiny and Stone (2013) introduced a small tapering angle to the cell gap and demonstrated that it is possible to stabilise an otherwise unstable flow with a convergent angle. There was good agreement between their new linear stability analysis prediction of the stability threshold and experimental realisations of the flow. In another approach, replacing the top plate with an elastic film has been shown to delay the onset of instability (Pihler-Puzović et al., 2012) since the perturbations in pressure ahead of the advancing front are reduced by the bending of the film. Rather than introducing new terms to the growth rate equation, a variety of approaches involve altering the magnitude of viscous destabilisation relative to interfacial tension, and the gradual stretching of the interface in the case of radial spreading, in order to select the fastest growing mode for the duration of the flow.

Cardoso and Woods (1995) found the injection profile $Q(t) = \alpha_c t^{-1/3}$ leads to the total stabilisation of an axisymmetric displacement, where $Q(t)$ is the time-evolving injection flow rate and α_c is the constant of proportionality such that mode 2 is selected to be the fastest growing mode and is dynamically stabilised throughout injection by the continuous matching of destabilisation and stabilisation terms. With the same time dependency, Brenner et al. (1990) suggested that the injection profile $Q(t) = \alpha t^{-1/3}$ would give self-similar solutions for the nonlinear growth of a finger in a 90° sector cell. Li et al. (2009) numerically and experimentally confirmed that for any particular $\alpha > \alpha_c$, the linear stability theory prediction of the fastest growing mode is selected

by nonlinear interactions as that which becomes manifest after a brief adjustment period. These nonlinear interactions were theoretically analysed by Dias and Miranda (2010) who performed a mode-coupling analysis to derive the criterion that controls the selection of the fastest growing mode. This work was extended by Zheng et al. (2015) who showed that the fastest growing mode could be selected by introducing time dependency to the gap width rather than the injection flow rate. For a constant injection flow rate, they found that uniformly varying the plate separation such that the gap width, $b(t)$, followed the power law $b \propto t^{1/7}$ led to the fastest growing mode predicted by linear stability analysis being fixed over time in the experiments. The approach of interfacial control through mode selection has also been used in other contexts, which we will now discuss.

The potential of a three fluid system in reducing adverse viscosity gradients has also been explored (Mungan, 1971). The linear stability analysis for a three fluid system was first introduced by Nayfeh (1972) in a rectilinear geometry. This was later developed by Cardoso and Woods (1995) in an axisymmetric geometry. In the latter case, the annular intermediate fluid was thin in radial extent and also of very large viscosity. Experimentally, this resulted in the break up of the viscous annulus into droplets, the number of which was correctly predicted by linear stability analysis. Guided by the variation in injection rate required to stabilise a single interface, Cardoso and Woods (1995) found the equivalent variation in injection rate needed to stabilise the thin viscous annulus. In **chapter two** we generalise that analysis and develop an equation governing the variation of growth rate of the instability as a function of time for an annulus of any thickness or viscosity. We then go on to find the evolving critical injection flow rate such that the system is dynamically stable and then show how to select the viscosity of the annulus such that the overall injection time is minimised. This addresses the industrial need of rapidly and uniformly treating an oil reservoir with an annulus of chemical treatment fluid, as described in §1.1.

Following treatment of the reservoir to prevent sand production, oil recovery can begin. In most situations, constraints on time may not permit injection with a flow rate

that is sufficiently slow for stability and there will be growth of the instability. Often, polymers are added to the displacing fluid to reduce adverse viscosity gradients and improve stability (Sorbie, 1991). Mungan (1971) investigated the case of a three fluid system in which the intermediate fluid was a polymer solution. He demonstrated that programming the polymer concentration in a spatially varying manner leads to the very effective suppression of instability. With the viscosity of the solution approximately equal to the viscosity of oil at the leading interface and gradually reducing to that of the water at the trailing interface, he showed a significant improvement in the recovery of the oil phase compared to the recovery when the same mass of polymer is deployed at a uniform concentration. This problem was then theoretically analysed by Gorell and Homsy (1983), who arrived at the same conclusion through the variational calculus framework they developed. However, this strategy may be operationally challenging to deploy in the field. In **chapter three** we propose an alternative process: we consider the case of a single interface displacement in which the displacing fluid uniformly undergoes a gradual increase in viscosity, as might occur if a polymer is gradually released from a soluble encapsulant (Gun and Routh, 2013), if the polymer undergoes a change in viscosity that is thermally activated (Tran-viet et al., 2014) or if some other reaction, such as cross-linking or polymerisation, gradually takes place. To optimise this system, we build on the intriguing framework first proposed by Dias et al. (2012). Rather than seeking an injection rate which stabilises a specific mode for the duration of the injection, Dias et al. (2012) sought to minimise the final amplitude of perturbations following the injection of a finite volume of fluid in a finite time. In the case where the displacement started at a considerable radius from the injection point and was unstable for the duration of the flow, Dias et al. (2012) found that the optimal injection profile, $Q(t)$, is linear, $Q \propto t$, and leads to a significant suppression of instability in both experimental and computational realisations of the flow. This has been further confirmed in Hele-Shaw flow simulations by Huang and Chen (2015), who found that in contrast to the immiscible case if the fluids are miscible then the fingering is more severe with the linear injection scheme. Drawing on these results, we find that

in the case that the viscosity of the displacing fluid gradually increases, the optimal flow rate profile involves the injection of more fluid later in the flow as compared to the constant viscosity case in both rectilinear and axisymmetric displacements. Many polymer solutions feature a reduction in the effective viscosity at larger shear rates on account of the alignment of the polymer chains (Kamal et al., 2015). This property is known as shear-thinning. We extend our analysis of a Newtonian displacing fluid to a shear-thinning fluid and find that, in this case, the optimal flow rate involves increasing the injection flow rate to a lesser extent as compared to the Newtonian case.

These control methods are based on the linear stability analysis of the interface, which is valid when the amplitudes of instability are modest. As the instability develops fully, nonlinear calculations are needed to describe the evolution of the interface. In the most unstable and developed cases a heavily branched pattern forms for which bulk properties, such as the fractal dimension, are often invoked to describe the pattern.

1.3 Nonlinear Growth

To illustrate the development of viscous fingering beyond the linear regime, Saffman and Taylor (1958) used air to displace glycerine in a rectilinear Hele-Shaw cell, as reproduced in figure 1.2. Figure 1.2(a) illustrates the onset of instability and there are seven fingers with similar shapes whereas figure 1.2(b) depicts a later stage of the flow, when one finger has become dominant.

In nonlinear growth, such as that illustrated in figure 1.2(b), the injected fluid is diverted from neighbouring fingers to supply the dominant fingers. We shall refer to this interactive mechanism as screening (Praud and Swinney, 2005). Lajeunesse and Couder (2000) classify the subsequent behaviour of the dominant finger as either stable or unstable depending on its confinement, where the confinement is the ratio of the most unstable wavelength according to linear stability analysis (Chouke et al.,

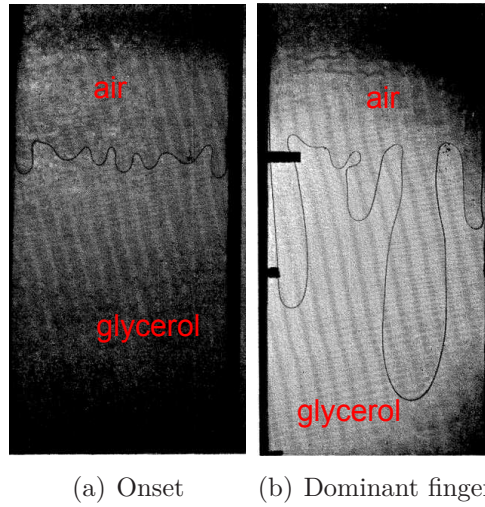


Fig. 1.2 The displacement of glycerol by air in a rectilinear Hele-Shaw cell at the onset of instability (a) and after the development of a dominant finger (b). From Saffman and Taylor (1958).

1959; Saffman and Taylor, 1958) to the width of the channel. If this wavelength and the channel width are of a similar scale then confinement is strong and a stable finger propagates through the channel. In contrast, if the wavelength is much smaller than the channel width then the confinement is weak and the finger undergoes the tip-splitting instability whereby the fingers continually branch.

To generalise the behaviour in rectilinear cells to those with non-parallel sides, Thomé et al. (1989) investigated the case of fingers propagating through sector-shaped cells and found self-similar fingers in the case of strong confinement. As in the case of rectilinear geometry, the role of interfacial tension in selecting the angular width of the self-similar fingers has been understood in sector geometry (Combescot and Ben Amar, 1991). Lajeunesse and Couder (2000) explored the growth of weakly confined fingers from the rectilinear geometry to the full circular geometry. It was found that above a 90° sector angle two long-lived structures are seen to coexist, whereas for sector angles smaller than this critical angle non-dominant branches are eventually screened from growth. In the full circular geometry, Thomé et al. (1989) proposed that the fingers behave as if they are divided into virtual sector cells with the virtual walls defining the effective confinement, and therefore stability, of the fingers. Lajeunesse and Couder

(2000) showed that if the confinement is weak there will be many generations of the tip-splitting instability. In this case, complex patterns form and bulk quantities, such as the fractal dimension, are used to describe the fingering. We now briefly introduce a number of key studies that investigated this weakly confined regime of viscous fingering, which becomes the focus of our final chapter.

Experiments performed by Praud and Swinney (2005) involved air injected at constant pressure, which led to the flow rate gradually increasing with time. Highly branched, complex fingering patterns were formed and the fractal dimension was found to be 1.70. In contrast to Praud and Swinney (2005), May and Maher (1989) performed constant flow rate experiments. In some of their experiments the fractal dimension was found to be 1.70, whereas in others was not. Since there is evidence to suggest that modifying the injection flow rate can suppress instability in the absence of tip splitting (Dias et al., 2012; Huang and Chen, 2015), it is of interest to understand whether the nonlinear pattern is different depending on the injection rate as a function of time. In **chapter four** we re-analyse the Praud and Swinney (2005) and May and Maher (1989) data, which present tip-splitting patterns. We assess the fractal dimension by analysing the radial distribution of air saturation (azimuthally averaged area fraction). There is no data available in the literature of the pattern of finger growth with a linearly increasing flow rate, so we performed a series of experiments for this situation. We discover a number of universal features in the variation of saturation with radius. In all cases, it is seen that inside of a particular radius the pattern is frozen. Growth of the pattern is concentrated at the tips as has previously been observed (Daccord et al., 1986; Praud and Swinney, 2005). However, the detailed delineation between the inner frozen pattern and the outer growing pattern is new. In the frozen region, the variation of saturation decreases with radius according to a power law, whereas in the outer part of the pattern the saturation decreases linearly to zero at the front of the pattern. Surprisingly, the overall radius of the pattern is found to be independent of the time dependence of the source flux for a fixed volume of injected fluid. The saturation distributions obtained in the experiments are also very similar to those

obtained from the 2D numerical diffusion limited aggregation models that we perform following Witten and Sander (1981) and Kuipers et al. (2014). We conclude with a description of the possible applications of this work.

Chapter 2

On the selection of viscosity to suppress the Saffman-Taylor instability in a radially spreading annulus

2.1 Summary

We examine the stability of a system with two radially spreading fronts in a Hele-Shaw cell in which the viscosity increases monotonically from the innermost to the outermost fluid. The critical parameters are identified as the viscosity ratio of the inner and outer fluids and the viscosity difference between the intermediate and outer fluids as a fraction of the viscosity difference between the inner and outer fluids. There is a minimum viscosity ratio of the inner and outer fluids above which, for each azimuthal mode, the system is stable to perturbations of that mode at any flow rate. This condition is directly analogous to the result for a single interface. Below this minimum ratio, the system may be stable at any flow rate early in the flow. However, once the inner radius reaches a critical fraction of the outer radius, this absolute stability ceases to apply owing to the coupling of the inner and outer interfaces. We determine the

maximum flow rate, as a function of time, in order that all modes remain stable due to the effects of interfacial tension. These criteria for stability are then used to select the viscosity of the intermediate fluid so that a fixed volume of the intermediate and then inner fluid can be added to the system in the minimum time with the system remaining stable throughout. The optimal viscosity for this intermediate fluid depends on the relative volume of the inner and intermediate fluid and also on the overall viscosity ratio of the innermost fluid and the original fluid in the cell, with the balance being to suppress the early time instability of the outer interface and the late time instability of the inner interface. We discuss application of this approach to a problem of injection of treatment fluid in an oil well.

2.2 Introduction

In processes which involve production of fluids from a subsurface porous layer through a well, interventions occur whereby from time to time two fluids are pumped in sequence into the porous rock from the well. One example of this occurs when reservoir engineers inject a chemical treatment to consolidate the oil-bearing sands (Paraskeva et al., 2000) or introduce an agent that inhibits the precipitation of salts in the event of any mixing between geologic and injected water (Woods, 2015). After the chemical treatment is injected into the rock from the well, post-treatment fluid is typically used to clean up the well and as a result the finite volume of treatment fluid is displaced by the post-treatment fluid, and forms an annulus some distance beyond the well. Taghlat et al. (2009) describe how it is difficult to obtain a uniform front of the injected chemical owing to the time constraint of injecting the treatment as quickly as possible, since the well is unproductive during such interventions. Any break up or fingering of the treatment fluid might lead to regions in which the treatment fluid is unable to form a competent bond designed to prevent sand production.

The challenge for such injection arises where adverse viscosity ratios are present. As well as two-phase flow effects, the interfaces are subject to the possible development

of viscous fingering. In this study, in order to build fundamental understanding of such coupled interface flows, we analyse the stability of an idealised flow involving two unstable interfaces spreading radially from a central source in a Hele-Shaw geometry. We use the analysis to select an optimum viscosity for the treatment fluid so as to prevent any instability during the injection process while maximising the injection rate.

Paterson (1981) pioneered the study of the single-interface radial viscous instability in a Hele-Shaw geometry, determining the linear growth rates of the different azimuthal modes. This analysis has been developed in a number of directions. For example, Miranda and Widom (1998) investigated weakly nonlinear tip-splitting phenomena, whilst Parisio et al. (2001) explored viscous fingering on the surface of a sphere. There has been interest in the control of such phenomena. Cardoso and Woods (1995) explained how fingering could be prevented by keeping the interface linearly stable at low flow rates. Li et al. (2009) developed a nonlinear analysis and a technique to control the final shape of the interface. In the context of Hele-Shaw flow, the possibility of control through varying the gap width has been explored (Al-Housseiny and Stone, 2013; Dias and Miranda, 2013a).

The two-interface problem was first introduced by Nayfeh (1972) and later developed by Cardoso and Woods (1995) who performed a theoretical and experimental dual-interface analysis in the special case in which the inner fluid is highly viscous. With a stable trailing interface and an unstable leading interface, they modelled the formation of drops from the annulus of intermediate fluid. However, in the present problem of well treatment, both interfaces are likely to be unstable. Recently, Gin and Daripa (2015) examined the growth rates of instabilities in a dual-interface system as a function of the viscosity of the three fluids in the system. In that analysis less attention was placed on the conditions for overall stability; however, this is relevant for the injection of treatment fluid followed by a volume of post-treatment clean-up fluid, and forms the focus of the present work. Our ultimate aim is to select the viscosity of the intermediate (treatment) fluid so as to minimise the overall injection time for both

the treatment fluid and the subsequent post-treatment fluid, whilst ensuring overall stability of the system. We assume that the original reservoir (outer) fluid is more viscous than the post-treatment (inner) fluid, and that the treatment fluid is of intermediate viscosity. For simplicity, we assume that the treatment fluid is immiscible with both the reservoir fluid and the post-treatment fluid, so that there is interfacial tension at both interfaces. In this regard, we note that if two fluids are only weakly soluble and hence only partially miscible, this can also lead to an effective interfacial stress (Korteweg, 1901; Pojman et al., 2006).

First, in §2.3 we analyse the linear stability of a single interface as a reference calculation and identify that there is a maximum flow rate below which all modes are stable. We relate this maximum flow rate to the viscosity of the displacing fluid. In §2.4 we explore the dual-interface system and determine conditions for both absolute stability of the lowest modes of the system, and also dynamic stability of all modes through control of the flow rate. In §2.5 we use these results to find the optimal choice of the viscosity of the treatment fluid so as to minimise the injection time.

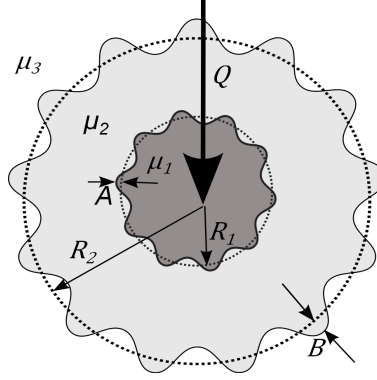


Fig. 2.1 Dual-interface variable definitions. The reservoir fluid (fluid 3) and post-treatment fluid (fluid 1) are separated by an annulus of treatment fluid (fluid 2). The leading and trailing interfacial base states are at radii R_2 and R_1 respectively, with perturbation amplitudes $B_n(t)$ and $A_n(t)$.

2.3 Single-Interface Stability: Treatment Injection Phase

2.3.1 Formulation

The flow configuration is shown in figure 2.1. In this section, we consider the stability of the leading interface alone. Paterson (1981) showed that the linear growth of perturbations of the form

$$b_n = B_n(t)e^{in\theta} \quad (2.1)$$

during radial displacement of a single interface is given by

$$\frac{1}{B_n} \frac{\partial B_n}{\partial t} = \frac{Qc_{23}n}{2\pi R_2^2} - \frac{Q}{2\pi R_2^2} - \frac{\kappa T n(n^2 - 1)}{R_2^3(\mu_2 + \mu_3)}. \quad (2.2)$$

In (2.2), B_n is the amplitude of azimuthal mode n , Q is the volumetric flow rate per unit depth, R_2 is the radial position of the interface, μ_i is the viscosity of species i , κ is the permeability of the porous medium (equivalent to $h^2/12$ where h is the Hele-Shaw cell gap spacing), T is the interfacial tension, the viscosity contrast $c_{ij} = (\mu_j - \mu_i)/(\mu_j + \mu_i)$, the treatment fluid is labelled 2 and the displaced reservoir fluid

is labelled 3. The first term on the right-hand side represents viscous destabilisation and the second and third terms represent the stabilising effects of stretching of the interface and interfacial tension respectively.

2.3.2 Absolute Stability of mode n

For each mode n , equating the viscous destabilisation term with the stretching term gives the maximum viscosity contrast for which the interface is stable for any flow rate, at all radii

$$c_{23} \leq 1/n. \quad (2.3)$$

We refer to this as absolute stability. We envisage that the treatment fluid is of intermediate viscosity between the reservoir fluid and the post-treatment fluid and so introduce a parameter P , the ratio of the viscosity difference between the treatment fluid and the reservoir fluid, to the viscosity difference between the post-treatment fluid (labelled 1) and the reservoir fluid. We also introduce a viscosity ratio between the post-treatment fluid and reservoir fluid V . They are respectively given by

$$P = \frac{\mu_3 - \mu_2}{\mu_3 - \mu_1}, V = \frac{\mu_1}{\mu_3}. \quad (2.4)$$

Hence, we can rewrite (2.3) in terms of P and V :

$$P \leq \frac{2}{(1 - V)(n + 1)}. \quad (2.5)$$

The values of P for absolute stability of mode n are shown in figure 2.2 for $n = 2, \dots, 6$. As V increases or P decreases higher modes become absolutely stable. Both regions are labelled for mode 2, otherwise each region is labelled with the highest mode that is absolutely stable.

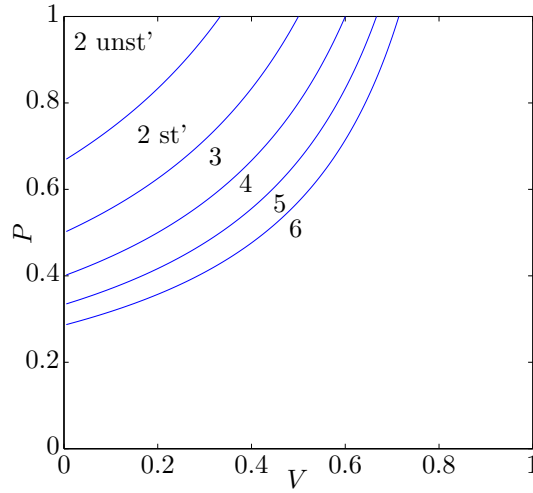


Fig. 2.2 Variation of the maximum value of P at which the labelled mode, $n = 2, \dots, 6$, becomes absolutely stable as a function of V . For a given mode n , then for values of P smaller than this maximum, all modes n' such that $n' < n$ are absolutely stable.

2.3.3 Dynamic Stability

If the viscosity contrast is higher than that given by (2.3), the viscous destabilisation term must be equated with the interfacial tension and stretching terms in order to control mode n . This yields a maximum flow rate $Q_n(R_2)$ for which mode n is stable at a finite radius, R_2 ,

$$Q_n(R_2) = \frac{1}{R_2} \frac{2\pi\kappa T n(n^2 - 1)}{(n(\mu_3 - \mu_2) - (\mu_3 + \mu_2))}. \quad (2.6)$$

It is convenient to scale $Q_n(R_2)$ by Q_{ref} , the flow rate at which mode 2 would go unstable at the well radius (R_w) if the reservoir fluid were displaced by an inviscid

species. Hence

$$Q_{\text{ref}} = \frac{12\pi\kappa T}{R_w\mu_3}, \quad (2.7)$$

$$R_2^* = \frac{R_2}{R_w}, \quad (2.8)$$

$$t^* = t \frac{Q_{\text{ref}}}{\pi R_w^2}, \quad (2.9)$$

$$Q_n^*(R_2) = \frac{Q_n(R_2)}{Q_{\text{ref}}}, \quad (2.10)$$

$$\Gamma(n) = Q_n^*(R_2^*)R_2^* = \frac{n(n^2-1)}{6((n+1)P(1-V)-2)}. \quad (2.11)$$

Henceforth, the stars are dropped for convenience. The minimum value of $\Gamma(n)$, $\Gamma(n_{\min})$ say, identifies the highest dimensionless flow rate such that the interface is stable to all such azimuthal modes (2.1). Higher modes are stabilised by interfacial tension, and lower modes by stretching. As an approximation for large n_{\min} , we can find the solution $n = n_{\min}$ by finding a solution of $\frac{d\Gamma}{dn} = 0$. This is given by the real, positive root of the equation

$$n^3(2P(1-V)) - n^2(6 - 3P(1-V)) - (P(V-1) + 2) = 0. \quad (2.12)$$

This provides a good approximation for large n , but is inexact since n is discrete. Note that there is only one real positive root of (2.12) if $P(1-V) < 2$, which is always true if the treatment fluid is of intermediate viscosity. In figure 2.3 we plot $\Gamma(n)$ for modes $n = 2 - 8$ (dotted lines) and $\Gamma(n_{\min})$ (solid line) as a function of P . The figure illustrates how for smaller viscosity jumps, P , the interface remains stable at larger flow rates Γ (2.11).

2.3.4 Single-Interface Control

The time t taken for the interface to advance to radius $R_2(t)$ starting with radius $R_2(0) = 1$ when injected at the highest dimensionless stable flow rate $\frac{\Gamma(n_{\min})}{R_2(t)}$ is

$$t = \int_1^{R_2} \frac{2R_2'^2}{\Gamma(n_{\min})} dR_2' = \frac{2}{3} \frac{(R_2^3 - 1)}{\Gamma(n_{\min})} \quad (2.13)$$

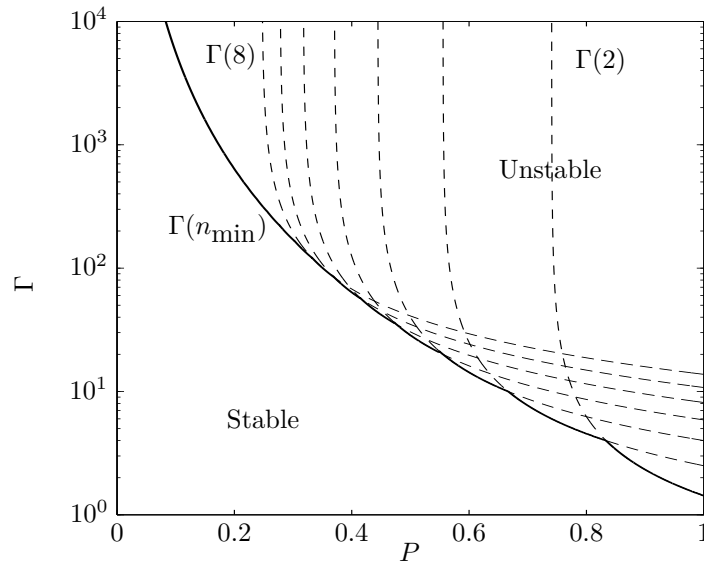


Fig. 2.3 Stability diagram for a radial displacement flow with $V = 0.1$, showing the highest $\Gamma(n) = Q_n^*(R_2^*)R_2^*$ for which the flow is stable to perturbations of mode n (dashed lines) plotted as a function of the ratio of the viscosity difference between the reservoir fluid and the treatment fluid, to the viscosity difference between the post-treatment fluid and the reservoir fluid. Solid line represents the locus of stability for all modes $\Gamma(n_{\min})$ as a function of P . If a more viscous displacing fluid is used, higher flow rates are permitted.

and this implies that the dynamically stable flow rate, $Q(R_2)$, is

$$Q(R_2) = Q_{n=n_{\min}}(R_2) = \frac{\Gamma(n_{\min})}{\left(1 + \frac{3}{2}\Gamma(n_{\min})t\right)^{\frac{1}{3}}}. \quad (2.14)$$

In the limit $t \gg 1$

$$Q(R_2) = \Gamma(n_{\min})^{\frac{2}{3}} \left(\frac{3}{2}t\right)^{-\frac{1}{3}}. \quad (2.15)$$

This generalises the result of Cardoso and Woods (1995) (their equation (5.2)) who analysed the limiting case of a large viscosity contrast in which only mode 2 needs to be considered.

This calculation identifies the maximum flow rate to ensure stability during the period in which there is one interface. During this phase it is desired to make $\Gamma(n_{\min})$ as large as possible which can be achieved by making the injected fluid more viscous (such that $c_{23} \rightarrow 0$). However, by doing so the subsequent clean-up phase (in which post-treatment fluid displaces the chemical treatment) tends to develop an unstable interface. The destabilisation of the trailing interface in an annular system could lead to the break up of the annulus of treatment fluid. Hence, we seek an optimum viscosity to minimise the time the well is out of production for given volumes of treatment chemical and post-treatment fluid. In order to inform this selection of viscosity we model the stability of a two-interface system in §2.4.

2.4 Dual-Interface Stability: Post-Treatment Fluid Injection Phase

2.4.1 Formulation

In this section we calculate the maximum flow rate for stability for a three fluid system, in which there are two interfaces at positions $R_1(t) + a(\theta, t)$ and $R_2(t) + b(\theta, t)$, where a and b are small perturbations to the shape of the interface. In general we can express

the perturbations of the interfaces in the form of a power series:

$$\begin{aligned} a(\theta, t) &= \sum_{n=1}^{\infty} A_n(t) e^{in\theta} \\ b(\theta, t) &= \sum_{n=1}^{\infty} B_n(t) e^{in\theta}. \end{aligned} \quad (2.16)$$

A schematic of the variables used in the calculation is shown in figure 2.1. The velocity potential ϕ is related to velocity \mathbf{v} and the pressure p by Darcy's law for flow in porous media

$$\mathbf{v} = -\frac{\kappa}{\mu} \nabla p = -\nabla \phi \quad (2.17)$$

and the flow is incompressible hence the velocity potentials obey Laplace's equation, $\nabla^2 \phi = 0$. The solution is assumed to comprise a steady solution $\phi_j^0 = -\frac{Q}{2\pi} \ln r + c_j$ and a first-order perturbation $\phi_j^1 = \sum_{n=1}^{\infty} \phi_{j,n}^1(r, t) e^{in\theta}$ where for mode n , the linearised perturbation has radial structure $\phi_{j,n}^1$ given by Laplace's equation (for $j = 1, 2, 3$)

$$\begin{aligned} \phi_{1,n}^1 &= \alpha_n(t) \left(\frac{r}{R_1} \right)^n, \\ \phi_{2,n}^1 &= \beta_n(t) \left(\frac{r}{R_1} \right)^{-n} + \gamma_n(t) \left(\frac{r}{R_2} \right)^n, \\ \phi_{3,n}^1 &= \epsilon_n(t) \left(\frac{r}{R_2} \right)^{-n}. \end{aligned} \quad (2.18)$$

Owing to the orthogonality of the modes, it follows that for each mode n at the trailing interface, R_1 , the continuity of velocity and the jump in pressure owing to interfacial tension are given by (Cardoso and Woods, 1995)

$$\frac{\partial v_1^0}{\partial r} A_n + v_{1,n}^1 = \frac{\partial v_2^0}{\partial r} A_n + v_{2,n}^1 = \frac{dA_n}{dt}; \quad (2.19)$$

$$\frac{\partial}{\partial r} \left(\frac{\phi_1^0 \mu_1}{\kappa} \right) A_n + \frac{\phi_{1,n}^1 \mu_1}{\kappa} = \frac{\partial}{\partial r} \left(\frac{\phi_2^0 \mu_2}{\kappa} \right) A_n + \frac{\phi_{2,n}^1 \mu_2}{\kappa} - \frac{T(1-n^2)}{R_1^2} A_n \quad (2.20)$$

where $v_{j,n}^1 = -\frac{\partial}{\partial r}\phi_{j,n}^1$. Similar conditions may be written for the leading interface at R_2 . Substituting the velocity potentials (2.18) into the boundary conditions (2.19, 2.20) and eliminating $\alpha_n(t)$, $\beta_n(t)$, $\gamma_n(t)$ and $\epsilon_n(t)$ yields the following set of coupled ordinary differential equations (ODEs) for each mode n :

$$\begin{aligned}\frac{dA_n}{dt} &= \underbrace{f_1 \left(\frac{Q(n-f_1^{-1})}{2\pi R_1^2} - \frac{T\kappa n(n^2-1)}{R_1^3(\mu_2-\mu_1)} \right)}_{(i)} A_n + \underbrace{f_2 \left(\frac{Qn}{2\pi R_2^2} - \frac{T\kappa n(n^2-1)}{R_2^3(\mu_3-\mu_2)} \right)}_{(ii)} B_n \\ \frac{dB_n}{dt} &= \underbrace{f_3 \left(\frac{Qn}{2\pi R_1^2} - \frac{T\kappa n(n^2-1)}{R_1^3(\mu_2-\mu_1)} \right)}_{(iii)} A_n + \underbrace{f_4 \left(\frac{Q(n-f_4^{-1})}{2\pi R_2^2} - \frac{T\kappa n(n^2-1)}{R_2^3(\mu_3-\mu_2)} \right)}_{(iv)} B_n\end{aligned}$$

where

$$\begin{aligned}f_1 &= \frac{c_{12}(1-c_{23}\hat{R}^{2n})}{1+c_{12}c_{23}\hat{R}^{2n}}, \quad f_2 = \frac{c_{23}(1+c_{12})\hat{R}^{n+1}}{1+c_{12}c_{23}\hat{R}^{2n}}, \\ f_3 &= \frac{c_{12}(1-c_{23})\hat{R}^{n-1}}{1+c_{12}c_{23}\hat{R}^{2n}}, \quad f_4 = \frac{c_{23}(1+c_{12}\hat{R}^{2n})}{1+c_{12}c_{23}\hat{R}^{2n}}, \\ \hat{R} &= \frac{R_1}{R_2}.\end{aligned}\tag{2.21}$$

The terms labelled (i) and (iv) on the right-hand sides of (2.21) describe local behaviour in which we can recognise terms for viscous destabilisation, stretching of the interface and interfacial tension (*cf.* (2.2)). The terms labelled (ii) and (iii) couple the two interfaces and in the limit of a thick annulus ($\hat{R} \rightarrow 0$) they become weak, leaving two separate single interfaces. The coupled ODEs can be written in matrix form

$$\frac{d}{dt} \begin{pmatrix} A_n \\ B_n \end{pmatrix} = \mathbf{M} \begin{pmatrix} A_n \\ B_n \end{pmatrix}.\tag{2.22}$$

The growth rates of the system (λ^+, λ^-) are the eigenvalues of \mathbf{M} . In the limit of a thin annulus ($\hat{R} \rightarrow 1$; $R_1 = R_2$) the growth rates have the asymptotic form

$$\begin{aligned}\lambda^+ &= \frac{Qc_{13}n}{2\pi R_2^2} - \frac{Q}{2\pi R_2^2} - \frac{2\kappa Tn(n^2 - 1)}{R_2^3} \frac{1}{\mu_1 + \mu_3}, \\ \lambda^- &= -\frac{Q}{2\pi R_2^2}.\end{aligned}\tag{2.23}$$

In equation (2.23) the largest growth rate is that which would occur with species 1 displacing species 3 (no annulus; *cf.* (2.2)), but with twice the individual interfacial tension. In the limit of a stable inner interface ($\mu_1 \gg \mu_2, \mu_3$) the result matches that given by Cardoso and Woods (1995). These asymptotic limits were also derived by Gin and Daripa (2015).

To understand the controls on the onset of instability, and hence determine the critical flow rate to ensure stability, it is of interest to study the nature of the instabilities as the three controlling parameters \hat{R} , V and P vary.

2.4.2 Absolute Stability of Mode n

The single-interface stability problem reveals the fascinating result that there is a viscosity contrast below which a mode is stable at all flow rates and radii (absolute stability), based on the balance between the stretching of the interface owing to the radial spreading and the viscous destabilisation. We can draw from that result to provide insight into the two-interface problem.

For small values of \hat{R} , we expect the two interfaces to be largely decoupled. We expect that as P increases the outer interface becomes progressively more unstable. To assess this transition in more detail, it is useful to consider how the condition for absolute stability depends on the viscosity change between the treatment and reservoir fluids, P , and also the ratio between the post-treatment and reservoir fluid viscosity V . We can then generalize these results for $\hat{R} = \mathcal{O}(1)$ where coupling between the interfaces becomes significant.

Absolute stability results from balancing viscous destabilisation with stretching, and in the dual-interface system this is done by setting $\text{Det}(\mathbf{M}) = 0$ with $T = 0$. This yields

$$c_{12}c_{23}(1 - \hat{R}^{2n})n^2 - (c_{12} + c_{23})n + 1 + c_{12}c_{23}\hat{R}^{2n} = 0. \quad (2.24)$$

In the limit $\hat{R} \rightarrow 0$, (2.24) gives the condition for absolute stability of mode n from §2.3.2 for two separate single interfaces,

$$\begin{aligned} c_{12} &\leq \frac{1}{n}, \\ c_{23} &\leq \frac{1}{n}. \end{aligned} \quad (2.25)$$

These conditions are combined by writing them in terms of P , giving the condition for absolute stability for mode n

$$\frac{1 - \frac{n+1}{n-1}V}{1 - V} \leq P \leq \frac{2}{(1 - V)(n + 1)}. \quad (2.26)$$

Below the lower bound the trailing interface is locally not absolutely stable, and likewise above the upper bound the leading interface is not. Equating these conditions gives a critical V below which neither mode can be absolutely stable

$$V_{\text{lower}}(n) = \left(\frac{n - 1}{n + 1} \right)^2. \quad (2.27)$$

In figure 2.4(a) we show the upper P bound of the absolutely stable region as a solid line (familiar from §2.3.2) and the lower bound P as a dashed line for mode 2 as a function of V . The system is only absolutely stable in region (ii). Elsewhere, viscous destabilisation on one or both interfaces is possible and can only be stabilised by controlling flow rate. In figure 2.4(b) we extend this to higher modes by indicating which modes ($n' \leq n$) are absolutely stable in each domain. This figure is important since it illustrates how, at the onset of instability, the lowest modes in the system may not be unstable at all, depending on the parameters P and V . To determine which

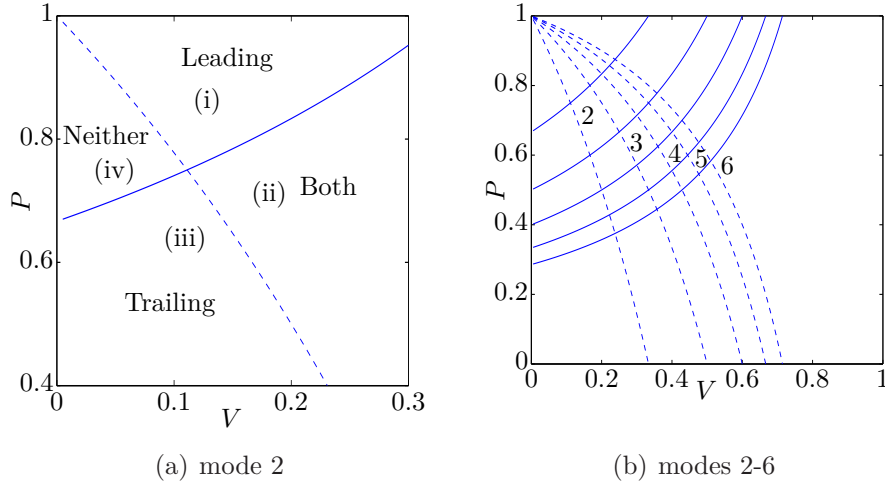


Fig. 2.4 The non-dimensional difference in viscosity across the leading interface, P , at which the trailing (dashed) and leading (solid) interfaces become absolutely stable to the given mode as a function of the bounding viscosity ratio, V for the limit $\hat{R} \rightarrow 0$. In (a) we show which interface is absolutely stable for mode 2. In regions (i) and (iii) the leading or trailing interface alone is respectively absolutely stable, whereas in region (ii) both interfaces are absolutely stable and in region (iv) both interfaces impose a flow rate limitation for stability. In (b) we show how this extends to higher modes.

mode will be unstable first, the effect of interfacial tension must be considered (see §2.4.3).

As fluid continues to be supplied to the system, the inner radius grows and \hat{R} increases. This leads to a progressively increasing level of coupling between the leading and trailing interfaces. In the case $V > V_{\text{lower}}(n = 2)$, we identified values of P for which mode 2 becomes absolutely stable with $\hat{R} \ll 1$; as \hat{R} increases, we expect that the coupling will cause these bounding values of P to converge, and eventually that there is a value of \hat{R} for which there is no longer a region of absolute stability for mode 2. The bounding values of P can be found by solving (2.24) at chosen values of V , \hat{R} and n . We illustrate this trend in figure 2.5 in which we show how the bounding values of P vary with \hat{R} for mode 2 where $V = 0.3$. The boundary for mode 3 is also plotted and is contained within that of mode 2. In this case, there are no regions of absolute stability for mode 4 since $0.3 < V_{\text{lower}}(n = 4)$.

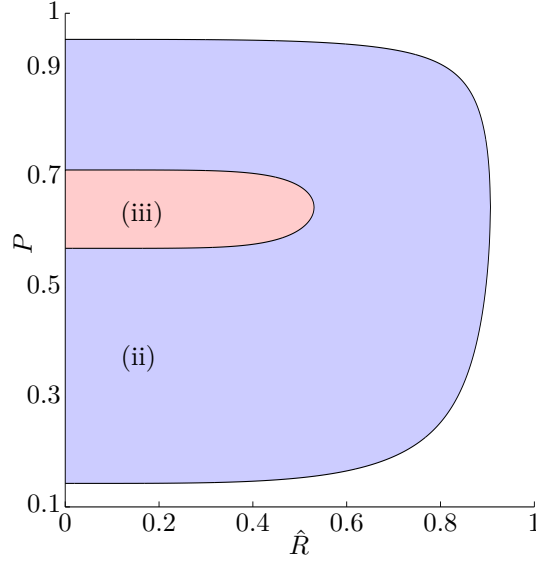


Fig. 2.5 The critical values of the non-dimensional leading viscosity jump, P , for absolute stability as a function of \hat{R} for $V = 0.3$. In regions (ii) and (iii) modes 2 and 3 are absolutely stable respectively. As time and hence \hat{R} increase, the annulus thins and these lines converge. As such, absolute stability is transient for modes 2 and 3 for this value of V .

In the limit of a thin annulus, $\hat{R} \rightarrow 1$, (2.24) has the asymptotic form

$$c_{13} \leq \frac{1}{n}. \quad (2.28)$$

This condition can be obtained by considering a single interface with post-treatment fluid displacing reservoir fluid directly (see §2.3.2). It can also be written as a function of V

$$V_{\text{upper}}(n) = \frac{n-1}{n+1}. \quad (2.29)$$

Equation (2.29) shows that in the case $V > 1/3$, the instability that would result from post-treatment fluid directly displacing the reservoir fluid is only unstable to higher modes, $n \geq 3$, and so the two-interface problem is also only unstable to these higher modes. In this case, depending on the value of P we expect that the most unstable mode could correspond to much higher values of n . Figure 2.6 shows how the absolutely stable region of figure 2.4 evolves as \hat{R} increases for mode 2 (solid lines)

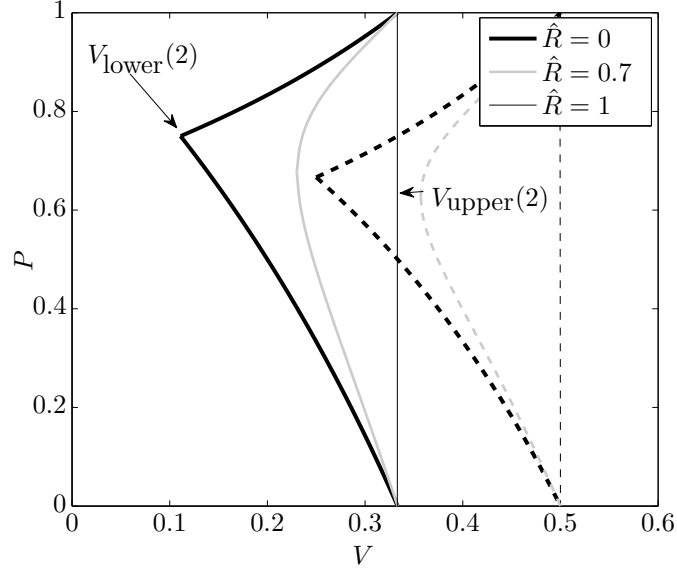


Fig. 2.6 The critical values of the non-dimensional difference in viscosity across the leading interface, P , at which the dual-interface system is absolutely stable as a function of V for modes 2 (solid lines) and 3 (broken lines) for three values of \hat{R} . The $\hat{R} = 0$ curves can be recognised from figure 2.4 with cusps at $V_{\text{lower}}(n)$. As \hat{R} increases, the annulus thins and the stability tends to that of a single interface in a system in which the post-treatment fluid displaces the reservoir fluid, with a vertical boundary at $V_{\text{upper}}(n)$.

and mode 3 (broken lines). As \hat{R} increases, the bounds tend towards a vertical line at $V_{\text{upper}}(n)$. The system is only absolutely stable if an interface between the post-treatment and reservoir fluid is absolutely stable. The cusp at $V_{\text{lower}}(n)$ for mode 3 is larger than the cusp for mode 2, as expected from figure 2.5.

We have found that if $V_{\text{lower}}(n) < V < V_{\text{upper}}(n)$ there are solutions of (2.24) that are transient absolutely stable bounds of P , *i.e.* initially mode n can be absolutely stable but later in the flow interfacial tension must be considered for dynamic stability. Below this range there is no absolute stability and above it mode n remains absolutely stable at all radii. If mode n is absolutely stable, we must consider the dynamic stability of a higher mode to find the maximum flow rate for the system's stability.

2.4.3 Dynamic Stability

In general, the condition for stability is found by balancing the viscous destabilisation with the stretching and interfacial tension terms to ensure $\lambda^+ = 0$, since if either growth rate were positive the perturbations would grow. The eigenvalues are given by

$$\lambda^\pm = \frac{\text{Tr}(\mathbf{M})}{2} \pm \sqrt{\left(\frac{\text{Tr}(\mathbf{M})^2}{4} - \text{Det}(\mathbf{M})\right)}. \quad (2.30)$$

It can be seen from (2.30) that if $\text{Tr}(\mathbf{M}) \leq 0$ and $\text{Det}(\mathbf{M}) = 0$, then $\lambda^+ = 0$ and $\lambda^- < 0$. If we solve the relation $\text{Det}(\mathbf{M}) = 0$ we find two solutions for $Q_n(R)$, but only one of these is in a region where $\text{Tr}(\mathbf{M}) \leq 0$ and therefore represents stability. To illustrate the evolution of the stability of the different modes as the fluids invade the pore space and the trailing front catches up with the leading front, in figure 2.7 we present the maximum value of $\Gamma = QR_2$ (thick line) below which the system is stable for the cases $\hat{R} = 0.1$ and $\hat{R} = 0.5$ where $V = 0.1$.

The left hand panel corresponds to $\hat{R} = 0.1$, which occurs at an early time in the injection process when the two interfaces are far apart. In this limit then to leading order the stability of each interface may be approximated by the local stability of that interface (2.21). In this case, the thick line showing the maximum flow rate for stability is approximately given by the mode 2 stability bound of the trailing interface for small P , but as P increases, this intersects the mode 6 stability bound of the leading interface for this value of \hat{R} . As P continues to increase, the critical flow rate for stability is given by successively lower modes, until coinciding, approximately, with the mode 2 stability of the leading interface.

In this limit of small \hat{R} , since the interfaces are far apart, the stability curves $\text{Det}(\mathbf{M}) = 0$ for the higher modes are well approximated by the stability curves for that mode on each of the two interfaces individually, and the effects of the coupling between the interfaces are small. Indeed, in figure 2.7(a) for all the higher modes, $n > 2$, with $\hat{R} = 0.1$ there is a common point at which $\text{Det}(\mathbf{M}) = 0$ and $\text{Tr}(\mathbf{M}) = 0$ which connects the solutions $\text{Det}(\mathbf{M}) = 0$ with $\text{Tr}(\mathbf{M}) < 0$ and the solutions $\text{Det}(\mathbf{M}) = 0$

with $\text{Tr}(\mathbf{M}) > 0$. For a given mode, $n > 2$, as we move across the point $\text{Det}(\mathbf{M}) = 0$ and $\text{Tr}(\mathbf{M}) = 0$, on the line $\text{Det}(\mathbf{M}) = 0$ we can interpret this point as corresponding to that at which the stability of the mode changes from being dominated by one interface to the other. The main exception to this for $\hat{R} = 0.1$ is for the lowest mode, mode 2 (solid thin line). Here, it is seen that for mode 2 the solution of the relation $\text{Det}(\mathbf{M}) = 0$ does not intersect the solution $\text{Tr}(\mathbf{M}) = 0$; instead for mode 2 two non-intersecting branches of the solution $\text{Det}(\mathbf{M}) = 0$ may be seen. $\text{Tr}(\mathbf{M}) < 0$ on the lower branch and $\text{Tr}(\mathbf{M}) > 0$ on the upper branch. The coupling between the interfaces leads to a loss of the special solution, $\text{Det}(\mathbf{M}) = 0$ and $\text{Tr}(\mathbf{M}) = 0$, for the lowest mode, mode 2. Instead there is a smooth adjustment along the line $\text{Det}(\mathbf{M}) = 0$ from the solution dominated by the leading interface when $P \approx 1$ to the trailing interface when $P \approx 0$.

However, as more fluid is injected and the trailing interface catches up with the leading interface, $\hat{R} = 0.5$ (right hand panel) then the distance between the interfaces becomes smaller and so some of the higher modes, notably modes 3-5, in the case $\hat{R} = 0.5$, also become highly coupled. As a result, for each of these modes there is no longer a solution $\text{Det}(\mathbf{M}) = 0$ with $\text{Tr}(\mathbf{M}) = 0$. Again, two independent solution branches for $\text{Det}(\mathbf{M}) = 0$ emerge for each of these modes. On the lower branch in (P, Γ) space, $\text{Tr}(\mathbf{M}) < 0$, and on a separate higher solution branch $\text{Det}(\mathbf{M}) = 0$ we have $\text{Tr}(\mathbf{M}) > 0$. Now the lower solution branch determines the maximum flow rate, Γ , for which that mode is stable to all perturbations.

In figure 2.7(b), the dark line again shows the overall stability boundary for all modes in terms of the maximum values of Γ for which the modes are stable, as a function of P . For small P , the stability threshold is determined by mode 2. However, for this larger value of \hat{R} , $\hat{R} = 0.5$, figure 2.7(b) shows that, as P increases, this first intersects the stability boundary for the higher modes with the mode 4 stability curve. With further increases in the value of P , this overall stability threshold is given by mode 3 and then back to the mode 2 at very large P .

It is also seen from the figure that higher modes only become unstable for large values of Γ and so are not rate-limiting in determining the maximum flow rate for stability. Indeed, in figure 2.8 we illustrate the most unstable mode for three representative values of \hat{R} as a function of P . In accord with the form of figure 2.7, it is seen that as the value of P increases from close to 0, the most unstable mode jumps from mode 2 to mode 6 when P has value of order 0.45, but then as P continues to increase this most unstable mode gradually falls again to mode 2.

This figure, in conjunction with figure 2.7, demonstrates how lower modes impose stricter limitations on the maximum stable flow rate as \hat{R} increases.

Our analysis has identified that, for small \hat{R} , there are values of P and V for which the system is unstable only to higher modes. If $V > V_{\text{lower}}$ (2.27), all modes $n' < n$ can be absolutely stable for a range of P . As \hat{R} increases, these lower modes also become progressively unstable. If $V > V_{\text{upper}}(n)$ (2.29), all modes $n' < n$ are stable for all P and \hat{R} . As fluid continues to be injected, the effect of interfacial tension, which is the mechanism ensuring stability, becomes progressively weaker. As a result, in order to ensure the stability of the system, the injection rate should progressively decrease. Depending on the values of P and V , the mode imposing the strictest limit on flow rate to maintain stability may become lower with increasing \hat{R} . Owing to the transition in this strictest-limit mode with the injection of a finite volume of fluid, the minimum time required for injection whilst maintaining stability depends on the choice of P .

2.5 Control Strategy

The aim of this section is to identify the optimal value of viscosity of chemical treatment to minimise injection time. This will depend on the viscosity ratio of the post-treatment fluid and reservoir fluid, V , but also on the volumes of chemical treatment fluid and post-treatment fluid to be deployed.

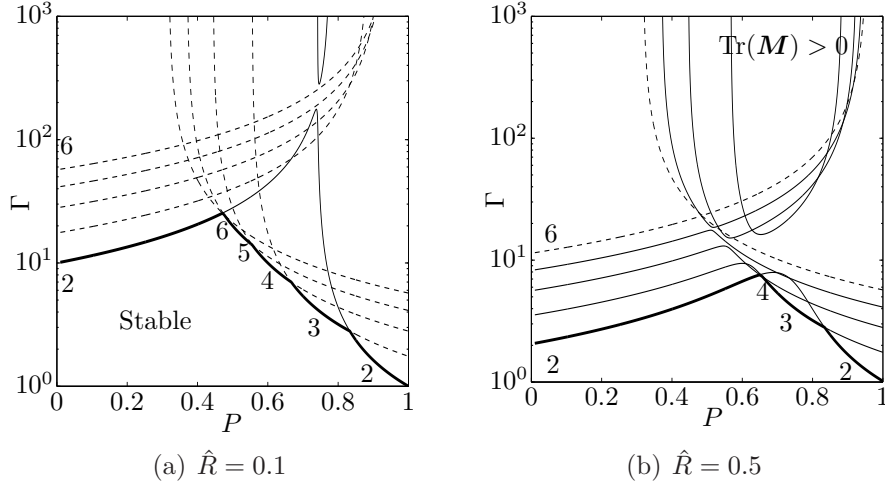


Fig. 2.7 Variation of the maximum flow rate, $\Gamma = QR_2$, for stability of the system to all modes (thick solid line) as a function of the non-dimensional leading viscosity jump, P , for $V = 0.1$ and for two values of \hat{R} , $\hat{R} = 0.1, 0.5$. Also shown in the figures are a series of thin lines on which $\text{Det}(\mathbf{M}) = 0$ for each of modes 2,...,6. In (a), for $n > 2$, there are two dashed lines for each mode: one of these lines has relatively small values of Γ for small P and Γ then increases monotonically with P , whilst the other has relatively small values of Γ for large P and Γ then decreases monotonically with P . The point of intersection of these two solution branches corresponds to the point $\text{Det}(\mathbf{M}) = 0$ and $\text{Tr}(\mathbf{M}) = 0$. However, for $n = 2$, there are two non-intersecting lines for which $\text{Det}(\mathbf{M}) = 0$ and these are shown as solid thin lines. The lower branch corresponds to the maximum value of Γ for which all perturbations of mode 2 are stable, while the upper branch corresponds to the minimum value of Γ for which all perturbations of mode 2 are unstable. In (b), we show solutions for $\text{Det}(\mathbf{M}) = 0$ for modes $n = 2, \dots, 5$ as thin solid lines, and for each such mode, there is a lower branch on which $\text{Tr}(\mathbf{M}) < 0$ and an upper branch on which $\text{Tr}(\mathbf{M}) > 0$, and these branches do not intersect. Note, however, that owing to the finite vertical scale, the upper branch of mode 2 does not appear in the graph. Also shown are two dashed thin lines, corresponding to $\text{Det}(\mathbf{M}) = 0$ for mode 6. The value of Γ on these two dashed lines increase and decrease monotonically with P , respectively, and their point of intersection again corresponds to the point $\text{Det}(\mathbf{M}) = 0$ and $\text{Tr}(\mathbf{M}) = 0$.

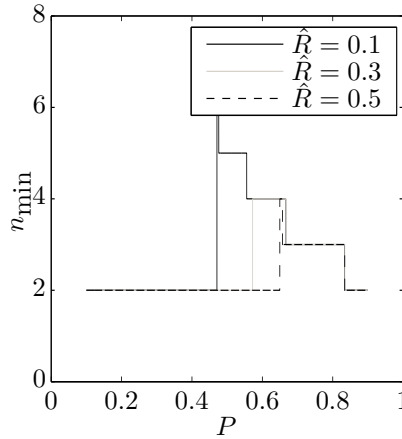


Fig. 2.8 The mode that requires the lowest flow rate to remain stable (n_{\min}) as a function of P for $V = 0.1$ and $\hat{R} = 0.1, 0.3, 0.5$. As \hat{R} increases coupling causes lower modes to impose the strictest limit on flow rate. There are some small spikes in n_{\min} when the respective range of values of P is narrow.

During treatment, a finite volume of fluid is injected with behaviour characterised in §2.3, followed by a finite volume of post-treatment fluid (see §2.4). Using the analysis of §2.3 and §2.4 we can identify the maximum possible flow rate for each value of P , as a function of time during the injection. By integrating this flow rate with time, we can then assess the value of P which minimises the total injection time.

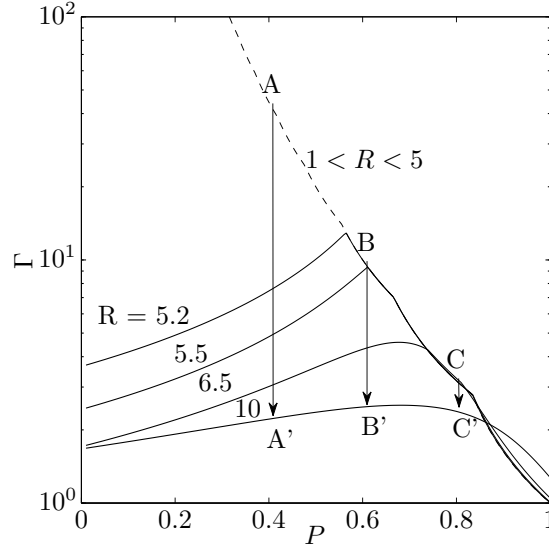
As an example of such a calculation, in figure 2.9(a) the maximum $\Gamma = QR_2$ for stability is shown as a function of P for different values of the outer radius of the treatment fluid R_2 . In these calculations, the post-treatment fluid is added to the system when $R_2 = 5$, and the whole process is completed when $R_2 = 10$. During the treatment phase, $1 < R_2 < 5$, the maximum flow rate to ensure stability of the system may be found using the single-interface analysis of §2.3 (dotted line). However, once the post-treatment fluid starts to be injected, for $R_2 \geq 5$, the stability of the trailing interface should also be taken into account in determining the maximum flow rate for stability of the system. We show how this maximum flow rate changes as a function of R_2 in figure 2.9(a), illustrating the bounds for the values $R_2 = 5.2, 5.5, 6.5$ and 10 (solid lines) as obtained from the analysis of §2.4. For a specific choice of P we see that Γ needs to be systematically reduced once $R_2 > 5$ and both interfaces are migrating

through the system, and this has been illustrated schematically with the lines A-A' , B-B' and C-C'.

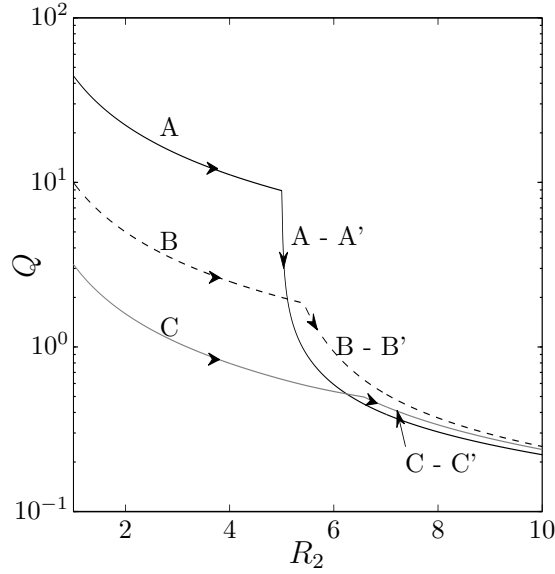
For clarity, in figure 2.9(b) we illustrate how $Q = \Gamma/R_2$ varies as R_2 increases, following each of the lines A-A' , B-B' and C-C' from figure 2.9(a). It is seen that for larger values of P (*e.g.* curve C-C'), the maximum stable flow rate during the treatment phase, $R_2 < 5$, is smaller but as R_2 increases further during the clean-up phase, and the trailing interface becomes rate-limiting, the maximum flow rate may be smaller for smaller values of P . The trade-off between these early and late time effects can lead to a choice of P that minimises the overall time taken to inject the treatment fluid.

In order to illustrate this trade-off, in figure 2.10 we show the total injection time required for the leading interface to reach the value $R_2 = 10$ as a function of the viscosity of the treatment fluid, as parametrised by P . Curves have been shown for different values of the ratio of volume of treatment fluid to the total volume of fluid injected, as parametrised by $S = 1 - \hat{R}^2$. The overall time taken to sweep is found by integrating $Q(R_2)$. For each case, there is an overall optimum viscosity for the treatment fluid. Note that in the figure, time is scaled with the time it would take to inject the same total volume of fluid with a single interface between the reservoir fluid and the post-treatment fluid (*cf.* (2.13)). As S becomes larger, the optimal value of P decreases; this is because the effect of the instability at the trailing interface becomes smaller since less post-treatment fluid is added, and the interfacial tension on this trailing interface is more effective for smaller radii. Therefore, there is benefit in preferentially increasing the viscosity of the treatment fluid to maximise the average injection rate.

As an illustration of the potential benefits of this analysis in terms of injection time, we note that for example, in the case $S = 0.25$, by increasing the viscosity of the treatment fluid to the optimal viscosity, the minimum injection time to maintain overall stability is about 30% of the injection time when the treatment fluid has the same viscosity as the post-treatment fluid.



(a)



(b)

Fig. 2.9 (a) The maximum stable $\Gamma = QR_2$ as a function of P for a series of increasing R_2 where $V = 0.1$. The post-treatment fluid is injected at $R_2 = 5$. As such, for $1 \leq R_2 \leq 5$ the stability of the system is bounded by the single-interface analysis (broken line). Subsequently, the stability of the trailing interface must be considered and the stability is bounded by the dual-interface analysis (solid lines). (b) The maximum Q for stability varying with R_2 for the cases A, B and C in (a).

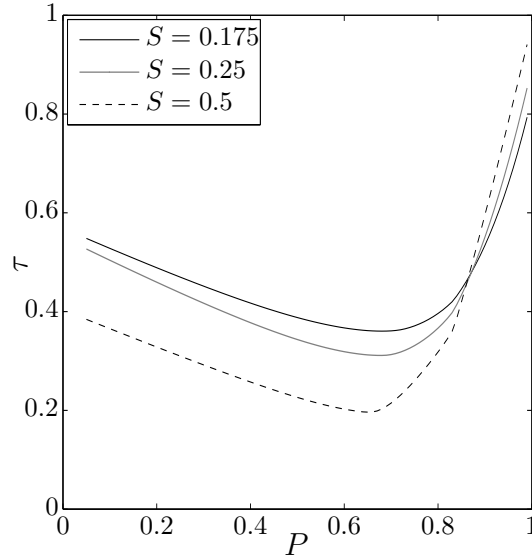


Fig. 2.10 Time to sweep to $R_2 = 10$ scaled with the time taken for a single interface in which post-treatment fluid displaces the original reservoir fluid for a series of increasing S as a function of the ratio of the leading viscosity jump to the global viscosity jump. The optimum viscosity choice balances the adverse viscosity ratios at the leading and trailing interfaces.

2.6 Conclusions

We have considered the stability of an annulus of fluid spreading from a point source in a Hele-Shaw geometry, in which there is an increase in viscosity across both the leading and trailing interfaces, so that both interfaces are potentially unstable. In a reference calculation of a single interface spreading axisymmetrically from a point source, we show that the stretching of the interface associated with the radial flow permits absolute stability for lower azimuthal modes for sufficiently small viscosity contrasts. We then find a maximum injection rate so that the viscous destabilisation of the interface is suppressed by the combination of the stretching and the interfacial tension for all higher modes.

We build on this analysis for a dual-interface system, in which there may be interactions between instabilities at the leading and trailing interfaces. We find that there is a range of viscosity of the intermediate fluid such that both interfaces are

absolutely stable and show how this range depends on the ratio of viscosities of the bounding fluids. We also find the maximum injection rate such that the combination of stretching and interfacial tension is able to suppress the instability of all modes in the system. By following the evolution of this critical flow rate with time during the injection of an annulus of finite volume and a finite volume of the subsequent fluid inside the annulus, we can calculate the minimum total time for injection. We examine how this minimum time varies with the viscosity of the fluid in the annulus, and thereby identify an optimal choice of viscosity that minimises the injection time while maintaining overall stability of the system. We also show how as the volume of the annulus as a fraction of the total volume of fluid injected increases, the optimal viscosity of the annular fluid increases. Also, the reduction in the time required for the injection of the annular fluid and the following inner fluid relative to the time to inject an equal volume of the inner fluid becomes progressively larger in order to maintain stability.

Although our analysis is strictly valid for Hele-Shaw geometries, the analysis suggests that in field operations in which treatment chemicals are added to a production well for scale management or to suppress sand production, there may be benefit in making the treatment fluid more viscous in order to minimise the time required for the treatment but also to ensure a uniform distribution of the treatment fluid around the well. As a very simplified example, if 10m^3 of treatment fluid was added to a well followed by 10m^3 of post-treatment fluid, with an injection rate of $0.0001\text{ m}^3/\text{s}$, the treatment time would be 30-40 hours; by making the treatment fluid more viscous, this process may be accelerated to a time closer to 10-20 hours, substantially reducing the non-productive time of the well.

Following the chemical treatment of the well, oil production may begin. During secondary recovery, polymers may be added to the injected water in order to reduce adverse viscosity gradients. The potential of deploying a polymer solution that features time-dependent rheology will now be explored.

Chapter 3

Control of viscous instability by variation of injection rate in a fluid with time-dependent rheology

3.1 Summary

Using variational calculus, we investigate the time-dependent injection rate which minimises the growth of the Saffman-Taylor instability when a finite volume of fluid is injected in a finite time, t_f , into a Hele-Shaw cell. We first consider a planar interface, and show that with a constant viscosity ratio the constant injection rate is optimal. When the viscosity of the displacing fluid, $\mu_1(t)$, gradually increases over time, as may occur with a slowly gelling polymer solution, the optimal injection rate, $U^*(t)$, involves a gradual increase in the flow rate with time. This leads to a smaller initial value of flow rate than the constant injection rate, finishing with a larger value. Such optimisation can lead to a substantial suppression of the instability as compared to the constant injection case if the characteristic gelling time is comparable to t_f . In contrast, for either relatively slow or fast gelling there is much less benefit in selecting the optimal injection rate, $U^*(t)$, as compared to the constant injection rate. In the case of a constant injection rate from a point source, Q , with a constant viscosity ratio

the fastest growing perturbation on the radially spreading front involves axisymmetric modes whose wavenumber increases with time. Approximating the discrete azimuthal modes by a continuous distribution, we find the injection rate that minimises growth, $Q^*(t)$. We find that there is a critical time for injection, t_f^\dagger , such that if $t_f > t_f^\dagger$ then $Q^*(t)$ can be chosen so that the interface is always stable. This critical time emerges from the case with an injection rate given by $Q^* \sim t^{-1/3}$. As the total injection time is reduced to values $t_f < t_f^\dagger$, the system becomes progressively more unstable and the optimal injection rate for an idealised continuous distribution of azimuthal modes asymptotes to a flow rate which increases linearly with time. As for the one-dimensional case, if the viscosity of the injection fluid gradually increases over time, then the optimal injection rate has a smaller initial value but gradually increases to larger values than for the analogous constant viscosity problem. If the displacing fluid features shear-thinning rheology, then the optimal injection rate involves a smaller flow rate at early times, although not as large a reduction as in the Newtonian case, and a larger flow rate at late times, although not as large an increase as in the Newtonian case.

3.2 Introduction

Viscous fingering occurs when a low viscosity fluid is used to displace a more viscous fluid through a porous medium. The phenomenon is of considerable importance for the oil industry since it can lead to injected water bypassing the oil in a reservoir, with the result that there are large pockets of unswept oil (Lake (1989); Woods (2015)). The injection of a less viscous fluid into a more viscous fluid in a Hele-Shaw cell is also subject to viscous fingering. The Hele-Shaw cell is used as a two-dimensional analogue model of a porous medium where pore-scale physics is neglected. Also, the planform curvature which acts with surface tension to cut off the wavenumber of instability in a Hele-Shaw cell is not present in a porous medium. With these problems acknowledged, we focus on Hele-Shaw flow in order to develop new concepts.

A variety of approaches to control the stability of the interface have been explored. They can be classed as involving modification of (1) the Hele-Shaw cell geometry, (2) the injection flow rate, (3) fluid properties or combinations thereof. For the first class, Al-Housseiny and Stone (2013) performed a linear stability analysis for flow in a tapering cell, and experimentally verified how the tapering angle modified the stability of the interface whereas Pihler-Puzović et al. (2012) investigated the stabilising effect of replacing the top plate with an elastic membrane. Zheng et al. (2015) defined a control parameter that, if held constant in time, permits selection of which azimuthal mode is manifest throughout the injection. In that study, the control parameter was held constant by varying the gap thickness, b , according to $b(t) \sim t^{1/7}$. In a different study, the control parameter was held constant by varying the injection flow rate, Q , according to $Q(t) \sim t^{-1/3}$ (Li et al., 2009). Both studies demonstrated good agreement between experiment and theoretical prediction of the dominant mode of instability which develops. For the latter case, Dias and Miranda (2010) went on to perform a weakly nonlinear mode-coupling analysis to explain how the $Q \sim t^{-1/3}$ injection flow rate leads to sharpening, stable fingers.

Modification of the fluids (class three) has also been shown to give interfacial control. The viscosity of the injected fluid can be increased, for example by adding a polymer (Sorbie, 1991). Since the field-scale deployment of polymer can be expensive, in some cases a finite volume of polymer solution is injected between the oil and the water. This leads to a series of interesting problems concerning the stability of a flood front with two interfaces. Gorell and Homsy (1983) explored the stability of a uni-directional constant flow in which the concentration of injected polymer varies with position in the flow. They developed a variational approach to determine the optimal concentration of the injected polymer as a function of time in order to to minimise the viscous instability when a finite mass of polymer and water are injected. Following a different approach, a stability analysis has been presented for a coupled problem based on flow in a Hele-Shaw cell (Cardoso and Woods, 1995). Gin and Daripa (2015) developed this by calculating the stability of a series of discrete layers of different viscosity

injected in sequence. However, there are challenges associated with the direct injection of polymer solutions into a porous medium, including the risk that the polymer may block up pore throats near the injector and hence prevent the continued injection of fluid into the reservoir in order to displace the oil (Sorbie (1991); Woods (2015)). In order to mitigate such risks, it is possible to use a polymer with a delayed activation so that the mixture viscosity gradually increases with time. There are a variety of methods that could achieve this. For example, if the polymer were supplied in a soluble encapsulant with a finite release time, then the concentration of polymer in solution would gradually change as the encapsulant dissolves. Gun and Routh (2013) explored the possibility of using poly(lactic-co-glycolic) acid to encapsulate a gelling agent that is gradually released. In the context of drug delivery in the body, Makadia and Siegel (2011) detail how the release profile of this encapsulant can be tuned by varying the composition. Alternatively, the polymer may be thermally activated, gelling once it passes through an activation temperature. Tran-viet et al. (2014) explored the thermal response of poly(NIPAM) to this end. The viscosity may also vary on account of reaction. Polyacrylamide (PAA) solutions are commonly used in oil field displacements (Kamal et al., 2015). In addition to gradual release from encapsulant, time dependency can be introduced to PAA solution viscosity through tailoring reaction kinetics. Han et al. (1995) demonstrated that the addition of chromium ions to PAA led to the formation of a cross-linked gel structure, and that the addition of acetic acid to this solution delayed the rate of gel formation. Furthermore, we hypothesise that by limiting the initial concentration of chromium ions, the rheological properties of the final polymer solution, including the cross-links, can also be controlled. In the case of PAA polymerisation, Lee et al. (2012) measured the gradual change in solution viscosity over the course of the reaction and demonstrated that the rate of reaction is dependent on the concentration of various reagents. With polymer solutions (including those of PAA), shear can cause the polymer chains to align which can lead to a decrease in the effective viscosity. Thus, polymer solutions with time-dependent viscosity may exhibit shear-thinning behaviour.

Drawing on the results of previous work related to time-dependent changes in viscosity, we now explore how such variations of viscosity may impact the stability of a moving interface, and given the evolving rheology, we also account for possible variations in injection rate. Such effects may be key for the class of problem in which a finite volume of fluid is to be injected in a finite time, and in this case there is the intriguing possibility that by varying the flow rate with time the final amplitude of instability can be further reduced. In exploring this class of problem, we are guided by the pioneering works of Dias et al. (2010) and Dias et al. (2012) who examined the impact of changes in flow rate on the growth of viscous fingers. In particular, Dias et al. (2012) considered the problem of injection of a finite volume of fluid in a finite time, and using variational calculus, developed an expression for the injection flow rate as a function of time which minimises the final amplitude of instability.

We have arranged the chapter as follows. In §3.3 we consider the impact of time-dependent rheology in a uni-directional displacement, in which there is a continuous range of unstable wavenumbers. we assess the relationship between the time-dependent viscosity of the injected fluid and the optimal injection rate. In §3.4 we extend the results to consider injection from a central source in which the instability leads to a discrete series of modes with increasing azimuthal wavenumber, n , of the form $A_n(t) \exp(in\theta)$ (*cf.* Paterson (1981)). In this case, the analysis is more complex owing to the continual stretching of the interface which progressively suppresses the instability of lowest modes as the interface grows, while surface tension suppresses the instability of the highest modes (*cf.* Cardoso and Woods (1995)). In order to make progress, following Dias et al. (2012) we approximate the discrete spectrum of modes with a continuous spectrum, noting that this will lead to an upper bound on the actual growth rate. We find that for a given initial radius R_0 , there is a particular total injection time, t_f^\dagger , for which the system is just stable, provided the injection rate decreases with time according to $Q = a(b + ct)^{-1/3}$, where the constants a , b , and c are found in our analysis. If t_f decreases to values $t_f < t_f^\dagger$, for this given R_0 , then the optimal injection rate gradually evolves towards the simple linearly increasing rate

$Q = d + et$, where d and e again are found from the analysis. This limit coincides with the results of Dias et al. (2012), who investigated the optimal injection rate in the limit $t_f \ll t_f^\dagger$. We then illustrate how a gradual increase in the viscosity of the injected fluid, for example resulting from slow activation of gel, modifies this optimal solution so that, as for the uni-directional flow, the optimal injection rate increases with time from a smaller to a larger value than for the case in which the injected fluid has a constant viscosity equal to the initial viscosity. Given that many polymer solutions exhibit shear thinning rheology, in §3.5 we generalise the analysis to account for such rheology in the calculation of the optimal flow rate with time. To this end, we draw on the analysis of Wilson (1990) and Mora and Manna (2009) who developed dispersion relations for the growth of viscous fingers in non-Newtonian fluids migrating through a Hele-Shaw cell. We compare our results to Fontana et al. (2014), who generalised the analysis of Dias et al. (2012) to air displacing a shear-thinning fluid. It was found that, with radial flow, the optimal injection rate involved a more rapid injection at early time and slower injection later as compared to the Newtonian case.

3.3 Newtonian Flow in a Rectilinear Geometry

3.3.1 Formulation

The depth-averaged flow of fluid in a Hele-Shaw cell is governed by the following equations (Saffman and Taylor, 1958):

$$\nabla \cdot \mathbf{u} = 0 \text{ and } \mathbf{u} = -\frac{b^2}{12\mu} \nabla p, \quad (3.1)$$

where \mathbf{u} denotes velocity, b is the plate separation, μ the viscosity of the fluid and p is the pressure.

By applying the interfacial boundary conditions of continuity of velocity and the jump in pressure on account of interfacial tension, and exploring the stability of the

interface to small sinusoidal perturbations along the interface, Saffman and Taylor (1958) obtained the dispersion relation

$$\frac{\dot{A}}{A} = \sigma_k = \frac{\mu_2 - \mu_1}{\mu_2 + \mu_1} U k - \frac{b^2 T}{12(\mu_1 + \mu_2)} k^3, \quad (3.2)$$

where T is the interfacial tension, $A(k, t)$ is the amplitude of a perturbation of wavenumber k , $U(t)$ is the velocity of the interface and subscript 1 denotes the displacing fluid whereas subscript 2 is the displaced fluid. With injection of a finite volume of fluid in a finite time t_f , such that the interface migrates a distance x_f , this relation may be expressed in dimensionless form

$$\hat{\sigma}_k = \frac{(1 - V)\hat{U}\hat{k} - \tau\hat{k}^3}{1 + V}, \quad (3.3)$$

where the hat notation denotes a dimensionless variable, $\hat{k} = kx_f$, $\hat{t} = t/t_f$, the stability parameter $\tau = \frac{b^2 T t_f}{12\mu_2 x_f^3}$, $\hat{U}(\hat{t}) = U t_f / x_f$, $\hat{\sigma} = \sigma t_f$ and $V(\hat{t}) = \frac{\mu_1(\hat{t})}{\mu_2}$. We now drop the hat notation for convenience and henceforth work with dimensionless variables. The wavenumber, k_{\max} , with maximum growth rate, σ_{\max} is given by

$$k_{\max} = \sqrt{\frac{(1 - V)U}{3\tau}}, \quad (3.4)$$

where

$$\sigma_{\max} = \frac{2}{3\sqrt{3\tau}} \frac{(1 - V)^{\frac{3}{2}}}{(1 + V)} U^{\frac{3}{2}}. \quad (3.5)$$

At each time, the growth rate of any mode, $\sigma(k, t) < \sigma_{\max}(t)$ and so an upper bound on the natural logarithm of the final amplitude of any mode is given by

$$I = \log(A_f) = \int_0^1 \sigma_{\max} dt \quad (3.6)$$

where A is scaled with the starting amplitude of any mode. In order to find the injection rate, $U(t)$, which minimises I subject to the requirement $\int_0^1 U dt = 1$, we can follow the Euler-Lagrange framework of variational calculus and seek a solution for

$U(t)$ of the equation

$$\frac{d}{dt} \left(\frac{\partial \sigma_{\max}}{\partial U} \right) = 0. \quad (3.7)$$

This leads to the ordinary differential equation for $U(t)$

$$(5 + V(t)) \dot{V}(t) U(t) - (1 - V(t)^2) \dot{U}(t) = 0, \quad (3.8)$$

with solution

$$U(t) = U^*(t) = \Omega \frac{(1 + V(t))^2}{(1 - V(t))^3},$$

$$\text{where } \Omega = \left(\int_0^1 \frac{(1 + V(t))^2}{(1 - V(t))^3} dt \right)^{-1} \quad (3.9)$$

and the star (*) indicates the variable is of the optimal value. If the viscosity ratio is constant, $\dot{V} = 0$, then (3.8) predicts that the constant flow, $U^* = 1$ is optimal. It follows that

$$k(t) = k(t)_{\max}^* = \sqrt{\frac{\Omega}{3\tau}} \frac{(1 + V(t))}{(1 - V(t))} \quad (3.10)$$

and

$$\sigma_{\max}(t) = \sigma(t)_{\max}^* = \frac{2}{3} \sqrt{\frac{\Omega^3}{3\tau}} \frac{(1 + V(t))^2}{(1 - V(t))^3}. \quad (3.11)$$

A key parameter in the present model is τ . Analysis of the upper bound on the amplitude of perturbations, (3.6), shows that this may be re-expressed in the form

$$A_f = \exp \left(\int_0^1 f(U(t), V(t)) dt / \tau^{1/2} \right), \quad (3.12)$$

where $f(U, V)$ takes on different functional forms depending on whether the injection rate is constant or follows the optimal injection rate. It follows that $A^{\sqrt{\tau}}$, $\sqrt{\tau} \sigma_{\max}$ and $\sqrt{\tau} k_{\max}$ are independent of τ .

3.3.2 Effect of a Gradual Increase in Viscosity

As mentioned in §3.2, the time-dependent viscosity could be tailored through choosing the thickness or composition of polymer micro-encapsulant, altering reagent concen-

trations to control polymerisation or cross-linking reaction kinetics or altering the temperature to trigger a thermally activated viscosity change. In the case of release from micro-encapsulant, we assume the viscosity of the displacing fluid is directly proportional to the concentration of released polymer and model this concentration as following the release profiles shown in Makadia and Siegel (2011). Thus, the viscosity ratio has the form

$$V(t) = V_o + (V_f - V_o) (1 - e^{-\theta t}), \quad (3.13)$$

where V_o is the initial viscosity ratio, V_f is the long-time asymptotic viscosity ratio and θ is the ratio of the injection time, t_f , to the characteristic time for the viscosity change or 'gelling'. In figures 3.1(a) and 3.1(b) we illustrate the optimal solutions for the cases in which $\theta = 1$, corresponding to slow gelling, and $\theta = 10$, corresponding to faster gelling. In both cases, the change in viscosity of the injected fluid is also defined by the ratio $V_f/V_o = 90$. In the case $\theta = 10$, the viscosity of the injected fluid reaches this target value early in the flow, whereas for the slow-gelling case, $\theta = 1$, the viscosity is increasing for the duration of the injection. For the faster-gelling case, $\theta = 10$, the optimal flow rate strategy involves injection of the majority of the fluid once the viscosity has reached its maximum value since adverse viscosity differences are reduced at these later times. In contrast, with slow gelling, the change in viscosity is smaller and so the optimal flow rate increases gradually with time. In figures 3.1(c) and 3.1(d) we show how the most unstable wavenumber $\sqrt{\tau}k_{\max}$ evolves in time, for the optimal flow rate (dashed lines), and, for reference, for the case of a constant injection rate (solid lines). With a constant flow rate, the most unstable wavenumber decreases with time, owing to the increasing stability of the system. In contrast, the optimal injection profile actually leads to a gradual increase in the most unstable wavenumber with time as a result of the increasing flow rate, even though the viscosity ratio falls with time. As a result of the different evolution of the maximum growth rate with time, we find that for the optimal flow, the maximum growth rate actually increases

with time owing to the progressively faster injection, whereas for a constant injection, the growth rate falls with time (figures 3.1(e), 3.1(f)).

We now explore the final amplitude of the perturbation, once the finite volume of fluid has been injected. In order to compare the benefit of the optimal injection rate with the case of constant injection, for different values of θ , it is convenient to investigate the variation of $A_f^{\sqrt{\tau}}$ with θ for each case. For clarity, figure 3.2(a) illustrates the difference between these two amplitudes as a function of wavenumber in the case $V_f = 0.9$ and $V_o = 0.01$. Figure 3.2(b) illustrates the ratio of the two final largest amplitudes as a function of θ . Both figures illustrate that the maximum benefit arises when θ is close to unity so that the viscosity is changing over the whole period of injection. For small or large θ the difference is much smaller, since in either of these limits, the majority of the injection occurs with either the original or the final viscosity. In figure 3.2(c), curves are given for $V_o = 0.01$ and $V_f = 0.5, 0.7$ and 0.9 corresponding to polymer solutions whose final viscosity is progressively larger. Each curve has a similar shape, but the magnitude of the reduction in amplitude associated with using the optimal injection strategy is greater when the change in viscosity of the polymer gel is greater. This is further illustrated by figure 3.2(d), which shows how the magnitude of reduction in amplitude diminishes as V_o approaches V_f for $\theta = 2$. Finally, in order to illustrate the effect of decreasing the overall injection time τ , in figure 3.2(e) we show contours of the ratio of the final amplitude associated with constant and optimal injection in $\theta - \tau$ space, for the case $V_o = 0.01$ and $V_f = 0.9$. As the value of τ is reduced from unity, corresponding to a shorter injection time, it is seen that the suppression of final amplitude is enhanced. For example, for $\tau = 10^{-3}$, $\log\left(\frac{A_f}{A_f^*}\right) \approx 2.5$, which corresponds to amplitude reduction by a factor of 12. We note that there is an upper limit on the validity of this analysis; for smaller values of τ and therefore larger amplitudes, nonlinear effects dominate behaviour and the amplitudes will be different to those predicted by linear stability analysis.

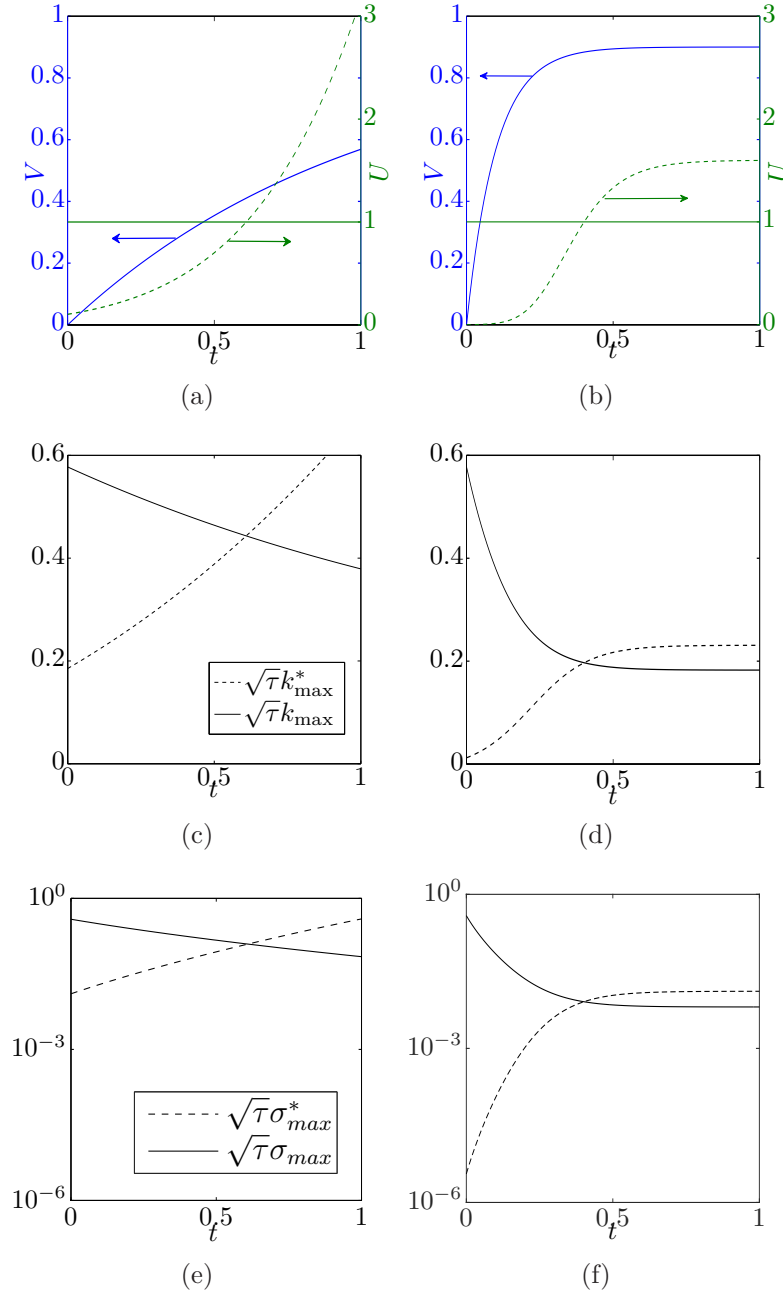


Fig. 3.1 Left column: $\theta = 1$ (slow gelling). Right column: $\theta = 10$ (rapid gelling). Top row: viscosity ratio profiles with parameters θ , $V_0 = 0.01$ and $V_f = 0.9$ (primary axis) and the optimal velocity profiles (secondary axis). Middle row: the evolution of $\sqrt{\tau}k_{\max}$ for the optimal (dashed lines) and constant (solid lines) flow rate profiles. Bottom row: the evolution of $\sqrt{\tau}\sigma$.

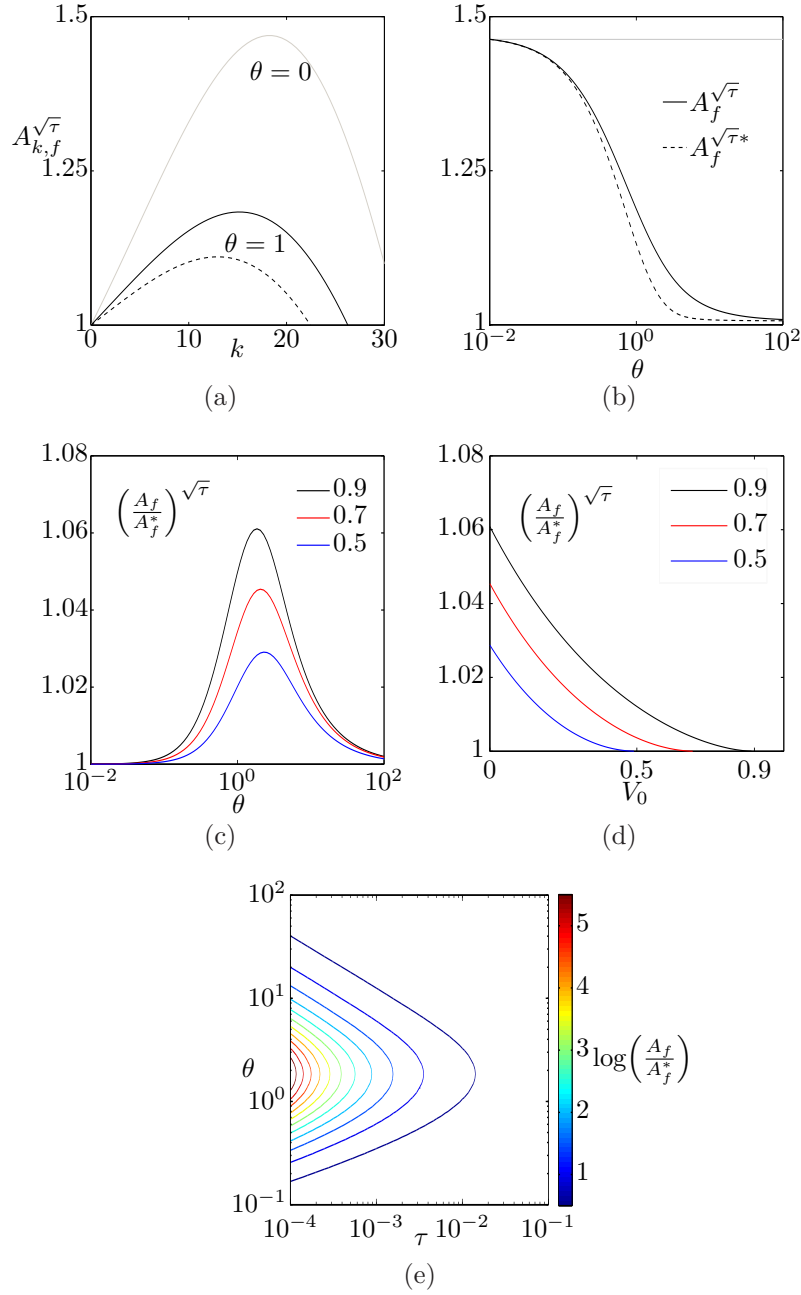


Fig. 3.2 (a) The final amplitude of perturbations of wavenumber k for the viscosity invariant case ($\theta = 0$, grey) and a gelling case ($\theta = 1$) for a constant flow rate (solid line) and the optimal flow rate (broken line). (b) The final maximum amplitudes varying as a function of θ for $V_f = 0.9$. (c) The ratio of these two final amplitudes as a function of θ for a series of V_f . (d) The effect of increasing V_0 for a series of V_f and $\theta = 2$. (e) A contour plot of the final amplitude ratio varying with τ and θ for $V_0 = 0.01$ and $V_f = 0.9$.

3.4 Injection from a point source

We now turn to the more complex problem of injection from a point source rather than a line source. Paterson (1981) derived a dispersion relation for the growth of perturbations on a circular interface of radius R in terms of a series of discrete azimuthal modes n , which depends on the viscosity ratio across the interface, V , the surface tension T and the permeability K , taken to be $b^2/12$ for a Hele-Shaw cell. For injection of a fixed volume of fluid, $\pi b(R_f^2 - R_0^2)$ over a time t_f , we can scale the growth rate with $1/t_f$ and the radius with R_f , leading to the dimensionless growth rate

$$\sigma_n(R, \dot{R}) = \frac{\dot{R}}{R} \left(\frac{1-V}{1+V} n - 1 \right) - \frac{\tau}{R^3(1+V)} n(n^2 - 1) \quad (3.14)$$

where the stability parameter $\tau = \frac{b^2 T t_f}{12 \mu_2 R_f^3}$. Although n corresponds to a series of discrete modes, we can find an upper bound on the maximum growth rate at each time by treating n as a continuous variable (Dias et al. (2012)) leading to

$$n_{\max}(R, \dot{R}) = \sqrt{\frac{1}{3} (1 + 2\Lambda \dot{R} R^2)}, \quad (3.15)$$

$$\sigma_{\max} = \left(\frac{1-V}{1+V} \right) \frac{1}{3\sqrt{3}\Lambda R^3} (1 + 2\Lambda \dot{R} R^2)^{3/2} - \frac{\dot{R}}{R}, \quad (3.16)$$

where $\Lambda = \frac{(1-V)}{2\tau}$. Since the amplitude of each mode grows as the exponential of the integral of the growth rate of that mode, the ultimate amplitude of the instability will be smaller than the expression

$$A = \exp \left(\int_0^1 \sigma_{\max}(\dot{R}, R, t) dt \right), \quad (3.17)$$

If we find a minimum value for A by varying dR/dt through all possible functions which satisfy the boundary conditions, then this will provide an upper bound on the amplitude of the instability. To this end we apply the Euler-Lagrange equation

$$\frac{d}{dt} \left(\frac{\partial \sigma_{\max}}{\partial \dot{R}} \right) = \frac{\partial \sigma_{\max}}{\partial R}, \quad (3.18)$$

leading to the following differential equation governing the optimal injection rate:

$$1 + \Lambda R^2 \dot{R} + \Lambda^2 R^5 \ddot{R} - \frac{\dot{V}}{2\tau(1+V)} (2R^3 + \Lambda(5+V)\dot{R}R^5) = 0. \quad (3.19)$$

3.4.1 The Constant Viscosity Regime

In the case that the injection fluid has constant viscosity, the evolution of R is given by the equation

$$1 + \Lambda R^2 \dot{R} + \Lambda^2 R^5 \ddot{R} = 0, \quad (3.20)$$

subject to the constraint that $R = R_0 < 1$ at $t = 0$ and $R = 1$ at $t = 1$, as noted by Dias et al. (2012). Subject to the appropriate boundary conditions, this equation has an exact solution which is available only in the special case that $\Lambda = \Lambda^\dagger$. The solution is

$$R = \left(\frac{t + t_o}{1 + t_o} \right)^{1/3}, \quad (3.21)$$

where $t_o = R_0^3/(1 - R_0^3)$. The special value Λ^\dagger can be found from substituting (3.21) into (3.20), giving

$$1 + (1/3)\Lambda^\dagger(1 - R_0^3) = (2/9)\Lambda^{\dagger 2}(1 - R_0^3)^2, \quad (3.22)$$

which requires

$$\Lambda^\dagger(R_0) = 3 \frac{1}{(1 - R_0^3)}. \quad (3.23)$$

This solution can be substituted into (3.15) to show that it fixes the most unstable mode to the mode $n_{\max} = 1$ for the injection duration. The solution can also be substituted into (3.16) to show that it corresponds to a maximum growth rate

$$\sigma_{\max}^{\dagger} = -\frac{2}{3(t+t_0)} \frac{V}{(1+V)}. \quad (3.24)$$

This solution was recently found independently using a different approach (Batista et al., 2016). If $V = 0$ this solution is neutrally stable for the duration of flow ($\sigma_{\max}^{\dagger} = 0$) and the result quantitatively matches the flow rate that would be found by setting $\sigma = 0$ in the dispersion relation (3.14), as described in the previous chapter (see §2.3.1). If $0 < V < 1$ then $\sigma_{\max}^{\dagger} < 0 \forall t$ and the solution (3.23) leads to a decay of each mode.

We have solved (3.20) numerically for $\Lambda = 3\Lambda^{\dagger}$ and $\Lambda = 10\Lambda^{\dagger}$, with fixed R_0 , and these solutions are shown in figure 3.3 (solid lines). It is seen that as Λ increases to values much larger than $\Lambda^{\dagger}(R_0)$, the variation of the optimal injection rate, $Q^* = 2R\dot{R}$, with time changes in character from the slowly decaying flow rate for values close to Λ^{\dagger} (included as a dashed line) to a linearly increasing flow rate in the case $\Lambda \gg \Lambda^{\dagger}$ (dashed-dotted line). This occurs since if the length of the injection duration permits, $\Lambda \gtrsim \Lambda^{\dagger}$ then the destabilising effects can be balanced against interfacial tension which is achieved by a decreasing flow rate. On the other hand, if the injection duration is much shorter, $\Lambda \gg \Lambda^{\dagger}$, then it is optimal to minimise the amount of time for which any particular mode is the most unstable by transitioning through the modes quickly, which is seen to be achieved by a linearly-increasing injection flow rate. The solution for $\Lambda \gg \Lambda^{\dagger}$ corresponds to the solution proposed by Dias *et al.* (2012),

$$R = R_0 + (1 - R_0)t \quad (3.25)$$

and the numerical solutions (solid lines) smoothly connect this limit with the solution (3.21) for $\Lambda = \Lambda^{\dagger}(R_0)$ which coincides with the analytical solutions in the formulation of Batista et al. (2016). We only consider values $\Lambda \geq \Lambda^{\dagger}$ since for values less than this the injection duration is longer than that required to fully stabilise the flow with interfacial tension. This leads to the solution of (3.20) involving a period of injection followed by a period of suction. Therefore, $\Lambda = \Lambda^{\dagger}$ marks the limit of values for which this optimisation approach is valid.

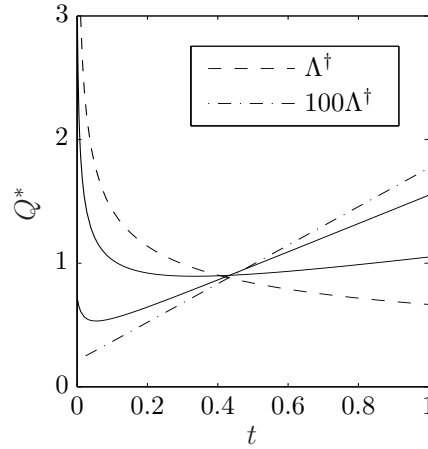


Fig. 3.3 The flow rate, $Q^*(t)$, that minimises $\int_0^1 \sigma_{\max} dt$ for $\Lambda = \Lambda^\dagger$ (dashed line), $\Lambda = 3\Lambda^\dagger$ and $\Lambda = 10\Lambda^\dagger$ (solid lines) and $\Lambda = 100\Lambda^\dagger$ (dashed-dotted line) while $R_0 = 0.1$.

We now explore the evolution of the instabilities over time, to assess the value of the predicted optimal injection rate, which is based on minimising the upper bound of the growth rate as a function of time, and we compare the results with the case of a simple constant injection rate.

It is useful to recall that the upper bound on the growth rate – σ_{\max} – has been estimated by assuming a continuous distribution of modes, whereas in practice, the modes are quantised in the azimuthal direction. We anticipate that for cases in which the most unstable azimuthal wavenumber is large, the model will offer a better bound than for slower injection rates when only the lowest modes are unstable.

To proceed, we first explore the evolution of the upper bound as a function of time during the injection, from the case $\Lambda \sim \Lambda^\dagger$ to the case $\Lambda \gg \Lambda^\dagger$. The only parameters which govern the optimal flow rate are Λ and R_0 , however, σ_{\max} additionally depends on the viscosity ratio V . In figure 3.4(a), the bound is shown with broken lines for two cases in which $V = 0$ and $R_0 = 0.2$: $\Lambda = \Lambda^\dagger$ (black) and $\Lambda = 3\Lambda^\dagger$ (blue) as labelled. The solid lines correspond to four cases in which $V = 0.1$ and $R_0 = 0.2$: $\Lambda = \Lambda^\dagger$ (black), $\Lambda = 3\Lambda^\dagger$ (blue), $\Lambda = 10\Lambda^\dagger$ (green) and $\Lambda = 30\Lambda^\dagger$ (red).

It is seen that in the case $V = 0$, the upper bound on growth rate is initially zero and with $\Lambda = \Lambda^\dagger$ this remains the case throughout the injection duration since it is the neutrally stable solution. With $\Lambda = 3\Lambda^\dagger$, the instability gradually develops with

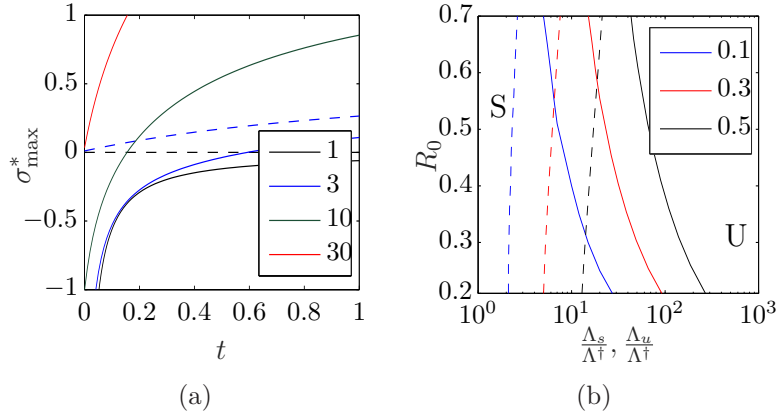


Fig. 3.4 (a) The evolution of the upper bound of growth rate, σ_{\max}^* , for $V = 0$ (broken lines), $V = 0.1$ (solid lines), $R_0 = 0.2$ and a series of values of $\frac{\Lambda}{\Lambda^\dagger}$ that increases from the bottom of the figure upwards. (b) A regime diagram for the conditions $\sigma_{\max}^* < 0 \forall t$ (broken lines; region S) and $\sigma_{\max}^* > 0 \forall t$ (solid lines, region U) for a series of values of V increasing from left to right (as labelled).

time. In the case $V = 0.1$, when $\Lambda = \Lambda^\dagger$ the bound is in fact stable throughout the injection period, whereas with $\Lambda = 3\Lambda^\dagger$, the bound is initially stable, but eventually becomes unstable just before all the fluid has been injected. As the value of Λ gradually increases, the bound becomes unstable at progressively earlier times until eventually it is unstable as soon as the injection commences. If we extrapolate from these results, it follows that for each initial radius R_0 there is a critical value of Λ , above which the bound is always unstable (Λ_u , solid lines), and a second critical value of Λ below which the bound is always stable (Λ_s , dashed lines). These values are shown in figure 3.4(b). Curves are given for viscosity ratios of 0.1 (blue), 0.3 (red) and 0.5 (black). For a given radius, the critical value of Λ below which the modes are always stable increases with the viscosity ratio owing to the reduced viscous destabilisation of the front. Similarly, the critical value of Λ for which the modes are always unstable increases with the viscosity ratio.

The number of discrete modes that become unstable during the course of the injection can be calculated from the evolution of the continuous bound n_{\max} (3.15). This is shown for the optimal injection case in figure 3.5(a) where $R_0 = 0.1$. For $\Lambda = \Lambda^\dagger$ (black line), the most unstable mode is fixed to $n_{\max} = 1$ for the duration of

the injection and the line coincides with the x -axis, as discussed. For $\Lambda = 3\Lambda^\dagger$ (blue line), initially mode 1 is the most unstable, but at the end of the injection mode 2 is the most unstable, whereas for $\Lambda = 10\Lambda^\dagger$, once again initially mode 1 is the most unstable, but at the end of the injection mode 4 has the largest growth rate. For $\Lambda = 100\Lambda^\dagger$ (green line) mode 2 is the most unstable at early times, while the most unstable mode at the end of the injection is mode 13 (not shown). Similarly, for $\Lambda = 1000\Lambda^\dagger$ (purple line), initially mode 4 is the most unstable, whereas the most unstable mode at the end of injection has now increased to mode 42. As the value of Λ increases, the discrete azimuthal mode that is initially the most unstable has a larger wavenumber and furthermore the span of different modes that become the most unstable during injection increases too. We now investigate the evolution of these discrete modes ($n = 2, 3, \dots$).

The coloured lines in figures 3.5(b-d) show the evolution of the growth rates of the discrete modes $n = 2, 3, \dots$ during the injection period for the case of injection at a constant rate. The upper bound σ_{\max} is included as the thick black line. The three figures (b-d) correspond to the cases $\Lambda = 3\Lambda^\dagger$ (panel b), $\Lambda = 10\Lambda^\dagger$ (panel c) and $\Lambda = 100\Lambda^\dagger$ (panel d). For comparison, in figure 3.5(e-g) we show the evolution of the growth rates of the discrete modes for the case in which the injection follows the optimal injection rate, the solution of (3.20). Panels (e-g) correspond to the same values of Λ as in panels (b-d). In the final three panels, (h-j), we present the amplitude of each of the discrete modes as a function of time for the case in which the injection follows the optimal injection rate.

When $\Lambda = 3\Lambda^\dagger$, mode 2 is the only mode to become unstable for both the constant (b) and optimal (e) injection flow rate profiles. In the case of constant injection, the bound on growth rate is initially large, then decreases to zero, and subsequently rebounds to a local maximum before decaying away. The bound is initially large on account of a non-physical mode, $n < 1$, that causes the interfacial tension term to become positive in the dispersion relation (3.14). The growth rate of mode 2 becomes positive during the flow but does not become as large as the bound, even at the end

of the injection. In the case of optimal injection, the bound monotonically increases from near zero to a final value larger than that of the constant injection case. Once again mode 2 is the only mode to become unstable during the flow, but in the optimal injection case the magnitude of the growth rate is equal to the bound σ_{\max} at the end of the injection. The amplitude of mode 2 at the end of the flow is small (of the order 10^{-1}) because the late-stage growth of the mode is insufficient to overcome the early time decay whilst the mode is stabilised by interfacial tension.

Where $\Lambda = 10\Lambda^\dagger$, the bound σ_{\max} in the constant injection case (c) initially increases, but after reaching a maximum it gradually decreases with time. The maximum in growth rate is larger and earlier in time than for $\Lambda = 3\Lambda^\dagger$. Mode 2 becomes unstable at an early time, with modes 3 and 4 following over the course of injection. The growth rate of each of the modes reaches a maximum value then decays away, leading to a cascade to higher modes. In the case of optimal injection (f), the bound on growth rate is once again initially small and then increases monotonically. The onset of instability of mode 2 is delayed relative to the constant injection case and features a smaller maximum than the constant injection case. The onset of instability of modes 3 and 4 is also delayed, but the maxima are larger in growth rate than the constant injection case. In contrast to the constant injection case, mode 5 becomes unstable during the flow. Figure 3.5(i) illustrates that the amplitude of mode 2 at the end of the injection phase is greater than the initial value, owing to the dominance of the instability at the later stages of injection, even though it is initially stable. However, the amplitudes of modes 3-5 do decay to smaller values.

For the case $\Lambda = 100\Lambda^\dagger$, in the constant injection case (d), the bound on growth rate is initially very large, then monotonically decreases for the duration of the flow and closely follows the locus of the mode that is the most unstable at that time. Mode 2 (bold orange line) is initially unstable, and also monotonically decreases in growth rate. Modes 6-16 behave like the lower modes when $\Lambda = 10\Lambda^\dagger$, insofar as they become unstable during the flow, reach a maximum in growth rate and then subsequently decay. Mode 11 is highlighted with a bold purple line. Curiously, the maximum in growth

rate of a discrete mode can occur before it becomes tangential to the bounding curve σ_{\max} . When the fluid is injected with the optimal injection rate, (g), the bound on growth rate is initially non-zero but nonetheless considerably smaller than the constant injection case. Mode 2 is initially unstable. The growth rate increases to a maximum coincident with the bound σ_{\max} , before decreasing as the radius increases further. Modes 3-22 all become unstable during the injection. The behaviour of each mode follows the same pattern of increasing towards the maximum growth rate and then decaying as the radius increases to larger values. However, owing to the fact that many of the modes are initially stable, the modes with larger azimuthal wavenumber, which spend a smaller fraction of the injection period being unstable than stable, finish with an amplitude smaller than unity. Only modes 2-4 feature overall growth during the injection.

As the value of Λ increases, the number of different modes that become unstable increases and the bound $-\sigma_{\max}$ becomes a better approximation of the locus of the most unstable mode for both the constant and optimal injection cases. There are two factors that appear to contribute to stabilisation: i) the large initial growth rates featured in the case of constant injection are mitigated by slower flow at early times in the optimal case and ii) a larger number of modes become unstable in the optimal case, giving each mode relatively less time to grow.

Figure 3.6 is a comparison of the final amplitude as computed from integrating the bound $-\sigma_{\max}^*$ (grey lines) – and the largest final amplitude of any discrete mode (black lines) as the total time of injection is reduced, *i.e.* as the value of Λ is increased for parameters $V = 0$ and $R_0 = 0.1$. This figure also compares the amplitudes resulting from constant injection (solid lines) and optimal injection (broken lines). The discrete-mode curves are not smooth. The overestimation of the final amplitude as computed by integrating the bound of all modes as compared to the actual growth rate of each individual mode can be seen by comparing the grey and black lines. The overall stabilisation gained by optimal injection can be seen by comparing the broken and solid lines. The effect of stabilisation is more pronounced when considering each mode

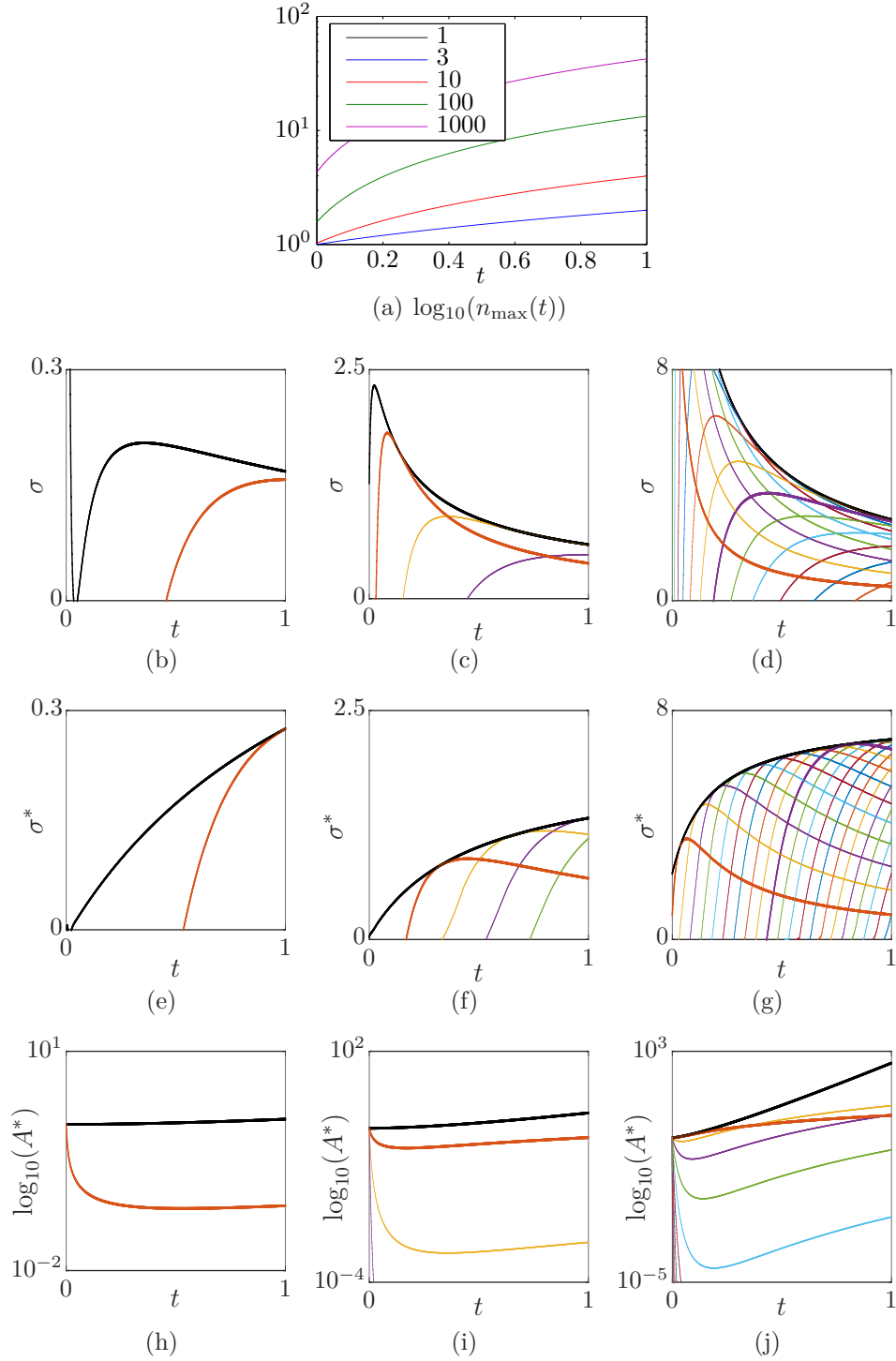


Fig. 3.5 (a) The evolution of the most unstable mode n_{\max} for $R_0 = 0.1$ and a series of $\frac{\Lambda}{\Lambda^\dagger}$ that increases from the bottom of the page upward. (b-g) The growth rate of discrete modes n for a constant injection rate (2nd row) and the optimal injection rate (3rd row) for $V = 0$, $R_0 = 0.1$ and $\Lambda = 3\Lambda^\dagger$ (left column), $\Lambda = 10\Lambda^\dagger$ (centre column) and $\Lambda = 100\Lambda^\dagger$ (right column). The mode number increases from the LHS to the RHS of the figures. (h-j) The amplitude of perturbations following the optimal injection rate. Initially, the lowest modes have the largest amplitude. Mode 2 (11) is highlighted with thick line in orange (purple). The growth-rate bound derived from treating n as a continuous variable is shown as the thick black line.

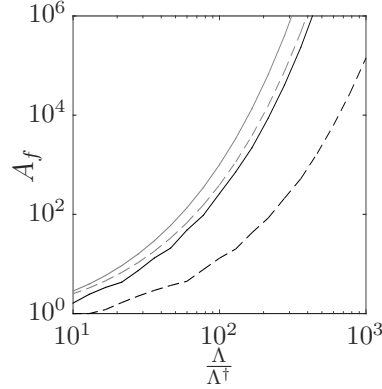


Fig. 3.6 The final amplitude varying with $\frac{\Lambda}{\Lambda_f}$ for $V = 0$, $R_0 = 0.1$ for constant injection (solid lines) and optimal injection (broken lines) computed with discrete modes (black) and a continuous series of modes (grey).

individually, and – as the curves are seen to diverge – the benefit of optimal injection becomes larger as the total injection time is reduced.

3.4.2 Effect of a Gradual Increase in Viscosity

As for the uni-directional flow problem, when the viscosity of the injected fluid gradually increases with time, we expect that the optimal flow solution will involve an increase in the flow rate with time relative to the case of a constant viscosity. The parameter $\Lambda = \frac{(1-V)}{2\tau}$ is no-longer a constant but varies with the change in viscosity between $\Lambda_0 = \frac{(1-V_0)}{2\tau}$ and $\Lambda_f = \frac{(1-V_f)}{2\tau}$. If the duration of the flow t_f is small, or interfacial tension T relatively weak given the duration of the flow, then, assuming $1 - V = \mathcal{O}(1)$, we can write $\tau \rightarrow 0$. In this case, expanding (3.19) in powers of τ whilst assuming all other variables remain $\mathcal{O}(1)$, leads to

$$(5 + V)\dot{V}\dot{R} - (1 - V^2)\ddot{R} = 0, \quad (3.26)$$

which has the solution

$$\dot{R} = (1 - R_0)\Omega \frac{(1 + V(t))^2}{(1 - V(t))^3}. \quad (3.27)$$

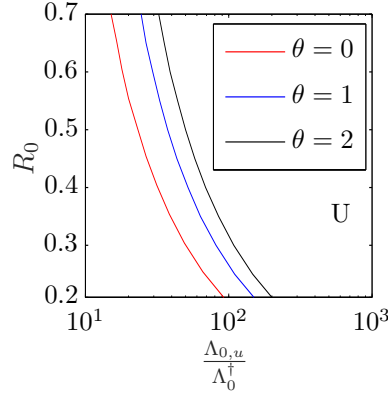


Fig. 3.7 The critical value of Λ_0 , above which the system is always unstable for the gelling case in which $V_0 = 0.3$ and $V_f = 0.5$. A series of values of gelling rate, θ , is shown.

This closely corresponds to the rectilinear case (3.9). To explore this behaviour, we use the same example of a gelling process as previously described using equation (3.13). In an analogous fashion to figure 3.4(b), for a given initial radius there is a particular value $\Lambda_{0,u}$ such that if $\Lambda_0 > \Lambda_{0,u}$ then the bound σ_{\max}^* is unstable for the duration of the flow. In figure 3.7, we present this critical value, $\Lambda_{0,u}$, for $V_0 = 0.3$ and $V_f = 0.5$. The critical value of Λ_0 for the non-gelling case, $\theta = 0$ (red), can be recognised from figure 3.4(b). In the gelling case, $\theta = 1$ (blue), the critical value $\Lambda_{0,u}$ is larger than for the non-gelling case since the growth rate can be negative at any stage of the flow. In the faster-gelling case, $\theta = 2$, the critical value $\Lambda_{0,u}$ is larger still.

Figure 3.8 shows how the optimal flow rate $Q^*(t)$ varies for a series of increasing gelling rates, θ , for parameters $V_0 = 0$, $V_f = 0.5$, $\Lambda_f = 1250$ and $R_0 = 0.35$. The left-hand panel compares the optimal flow rates when the viscosity change is slow relative to the injection duration, $\theta \lesssim 1$, whereas the right-hand panel corresponds to faster gelling, $\theta \gtrsim 1$. For the constant viscosity case, $\theta = 0$, the optimal injection profile analogous to the result of Dias et al. (2012), equation (3.25), is shown in figures 3.8(a) and (b) as broken lines. For a very slow gelling rate, $\theta = 0.1$ (red line), the optimal flow rate is initially smaller than the non-gelling case but then involves injecting with a larger injection rate than the non-gelling case at later times. This may be understood in terms of the system optimising the benefits of the higher viscosity at later times in

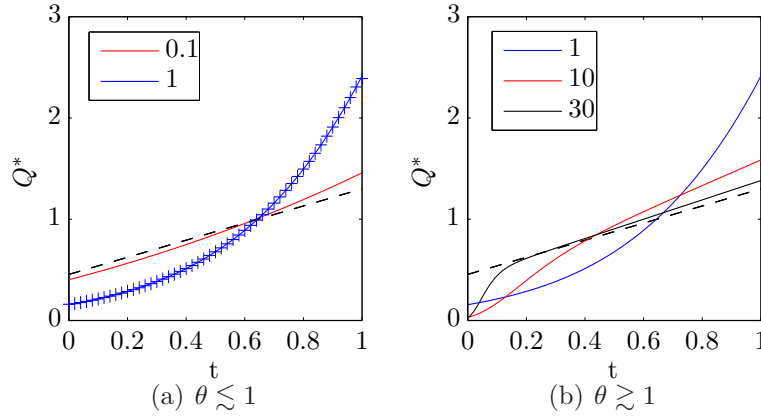


Fig. 3.8 The optimal flow rate, $Q^*(t)$, for a series of different gelling rates θ for $R_0 = 0.35$, $V_0 = 0$, $\Lambda_f = 1250$ and $V_f = 0.9$ found using (3.27) (solid lines) and the invariant viscosity case (broken line). In (a), the timescale of viscosity change compared to the flow is small, whereas in (b) it is large. In (a) the numerical solution to (3.19) is shown (crosses).

the injection process. As θ increases to the value for which the time scale of gelling and injection, t_f , are matched, $\theta = 1$ (blue line), these features become more pronounced. We also note that full numerical solution of the ODE (3.19) (crosses in figure 3.8(a)) and the asymptotic solution (3.27) (solid line) agree in this limit of a small total injection time, or large Λ_f . Turning to the right-hand panel, for $\theta = 10$ (red line), the optimal flow rate is more akin to the non-gelling case at late times, however, initially the flow rate is approximately zero. For $\theta = 30$ (black line; right-hand panel), the optimal flow rate is again initially approximately zero, and subsequently closely follows the non-gelling case since the viscosity ratio is effectively the final value, V_f , for the duration of the flow.

Figure 3.9 explores the benefit of injecting with the optimal flow rates shown in figure 3.8 at the end of the injection by illustrating the amplitudes of the discrete modes, $n = 2, 3, \dots$. In the absence of gelling, $\theta = 0$ (grey lines), the optimal injection solution (broken line) shows a smaller peak in amplitude of any of these modes than the constant injection case (solid line); this illustrates the benefit of optimal injection as discussed in §3.4.1. For $\theta = 1$ (black lines), the gelling leads to a reduction in the final maximum amplitude with constant injection since the adverse viscosity gradients

are reduced, and deploying the optimal injection strategy leads to further stabilisation. The variation of the magnitude of these maxima as the rate of gelling, θ , increases is shown in figure 3.9(b). As the rate of gelling increases, the amplitudes decrease to a smaller plateau. The amplitude of each mode at the end of the injection period when deploying the optimal injection rate solution is consistently smaller than those associated with using a constant injection rate and the ratio of these two values, which may be interpreted as a measure of the benefit of deploying the optimal injection strategy, is plotted in figure 3.9(c) (blue line). As with unidirectional flow, it can be seen that the benefit of using the optimal flow rate is largest when the time scale of gelling is similar to that of the flow, $\theta \approx 1$. Also, as the overall injection rate increases, the benefit of deploying the optimal injection rate is greater still, as illustrated for example with the case $\Lambda_f = 2500$ (black line).

3.5 Injection of a Shear-Thinning Fluid

In this section, we generalise the results of §3.3 to describe the injection of a fluid that exhibits shear-thinning rheology. We adopt a power-law model to describe shear-thinning:

$$\phi = k_1 \dot{\gamma}^m, \quad (3.28)$$

where ϕ is the shear stress, $\dot{\gamma}$ is the strain rate and k_1 and m are empirical fitting parameters known as the consistency index and flow behaviour index respectively. As pointed out by Mora and Manna (2009), the unperturbed interface velocity features zero shear at the centreline in Poiseuille flow. However, the power-law model we have adopted (3.28) neglects the Newtonian plateau in viscosity that might be seen at low shear rates. We shall discuss why this is necessary in the next paragraph. The Newtonian plateau is described in more detail by Martyushev et al. (2015). By ignoring it, they show how the power-law model modifies the Hele-Shaw flow equation (3.1) to become

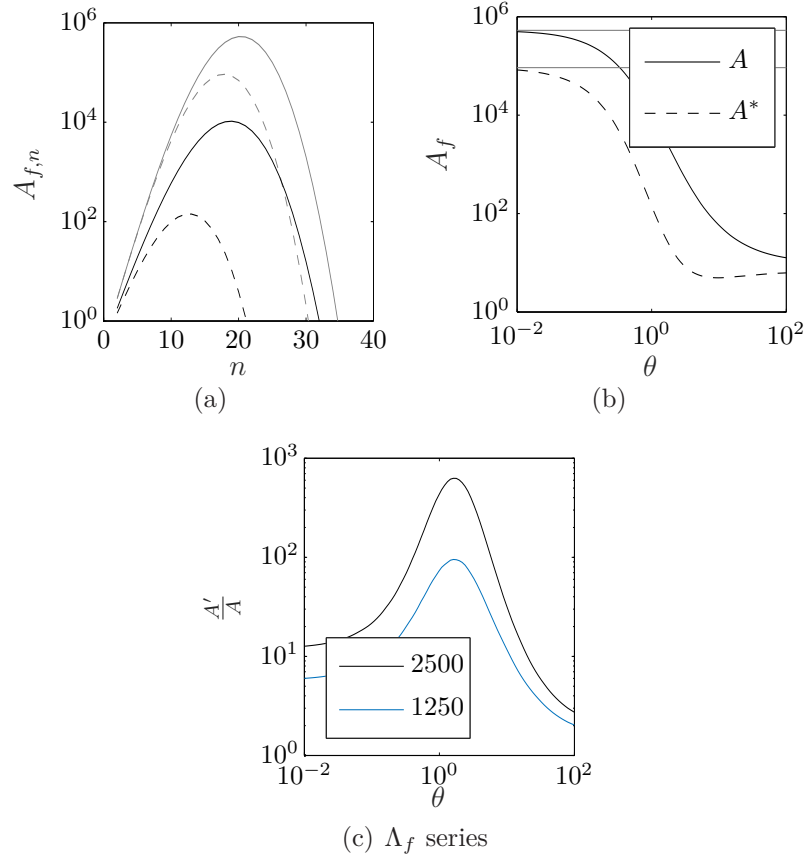


Fig. 3.9 (a) The final amplitude of each mode n for the viscosity invariant case ($\theta = 0$, grey lines), for a constant flow rate (solid lines) and the equivalent optimal flow rate (broken lines) where $V_0 = 0$, $V_f = 0.5$, $\Lambda_f = 1250$ and $R_0 = 0.35$. A gelling example is also shown ($\theta = 1$, black). (b) The variation of both maximum amplitudes with θ . (c) The ratio of the constant to optimal injection final amplitude plotted against θ for two values of Λ_f .

$$\mathbf{u} = -\frac{m}{2m+1} \left(\frac{|\nabla p|}{k_1} \right)^{1/m} \left(\frac{b}{2} \right)^{(m+1)/m} \frac{\nabla p}{|\nabla p|}. \quad (3.29)$$

Ghannam and Esmail (1998) have shown that this provides a reasonable representation of the behaviour of Polyacrylamide (PAA) over a large range of shear rates. If it were desired to incorporate the low-shear Newtonian plateau, a model such as the Carreau model (Carreau et al., 1979) could be used. There may additionally exist an infinite-shear Newtonian plateau, in which case the Cross model (Cross, 1965) could be used. However, following the analysis of Mora and Manna (2009) for a Carreau fluid, we note that it is not possible to explicitly write the pressure gradient as a function of the mean velocity, which leads to it not being possible to write the dispersion relation in this way. A fully numerical treatment would therefore be required to proceed with the optimisation and account for the low-shear Newtonian plateau.

To proceed, we now explore the growth rates of sinusoidal perturbations to the interface. Mora and Manna (2009) derive the dispersion relation for the displacement of one generalised Newtonian fluid by another (their equation 35), which we re-express here:

$$\sigma = \frac{k(p_{x,1} - p_{x,2} - k^2 T)}{\sqrt{\frac{p_{x,1}}{U} \frac{dp_{x,1}}{dU}} + \sqrt{\frac{p_{x,2}}{U} \frac{dp_{x,2}}{dU}}}, \quad (3.30)$$

where $p_{x,i}$ is the pressure gradient in the displacing ($i = 1$) and displaced ($i = 2$) fluids respectively. Following their analysis, but treating the displaced fluid as Newtonian (3.1) while using (3.29) to describe the shear-thinning rheology of the injected fluid, leads to the dispersion relation

$$\sigma = \frac{kU \left(1 - \frac{k_1}{\mu_2} \left(\frac{2m+1}{m} \right)^m \frac{b^2}{12} \left(\frac{2}{b} \right)^{m+1} U^{m-1} \right) - \tau k^3}{1 + \frac{k_1}{\mu_2} \left(\frac{2m+1}{m} \right)^m \frac{b^2}{12} \left(\frac{2}{b} \right)^{m+1} \sqrt{m} U^{m-1}}. \quad (3.31)$$

Following the method in §3.3.1, we proceed by making (3.31) nondimensional. Scaling lengths with x_f and time with t_f gives

$$\hat{\sigma} = \frac{\hat{k}\hat{U}(1 - \hat{\nu}\hat{U}^{m-1}) - \tau\hat{k}^3}{1 + \hat{\nu}\sqrt{m}\hat{U}^{m-1}}, \quad (3.32)$$

where $\hat{\nu} = \frac{k_1}{\mu_2} \left(\frac{x_f}{t_f}\right)^{m-1} \left(\frac{2m+1}{m}\right)^m \frac{b^2}{12} \left(\frac{2}{b}\right)^{m+1}$ and $\tau = \frac{b^2 T t_f}{12 \mu_2 x_f^3}$. The hat notation is henceforth dropped. The most unstable wavenumber, k_{\max} , with the largest growth rate σ_{\max} is given by

$$k_{\max} = \sqrt{\frac{(1 - \nu U^{m-1})U}{3\tau}}, \quad (3.33)$$

where

$$\sigma_{\max} = \frac{2}{3\sqrt{3\tau}} \frac{((1 - \nu U^{m-1})U)^{3/2}}{(1 + \nu\sqrt{m}U^{m-1})}. \quad (3.34)$$

Ghannam and Esmail (1998) observed that over the range of concentrations of PAA $0.25\% < C_{\text{PAA,wt}} < 1\%$, the flow behaviour index of the polymer solution, m , was constant with the value $m = 0.5$, whereas the consistency index, k_1 , increased from 410 to 1800 mPa s^{0.5}. Thus, we investigate the case in which $k_1(t)$ varies with changes in concentration following the release of polymer from an encapsulant but m is constant. Generally, however, we note that either m or k_1 might vary with the polymer concentration. For direct comparison to §3.3, we suppose that $\nu(t)$ has the same functional form as $V(t)$ in (3.13). In this case, we note that under the condition of constant flow, $U = 1$, the pressure gradient, $p_{x,1}$, would be the same if the displacing fluid was Newtonian – with viscosity μ_1 – or non-Newtonian, with the value of k_1 prescribed by the functional form of ν . The evolution of the perturbation amplitude, $A^{\sqrt{\tau}} = e^{\int \sqrt{\tau} \sigma_{\max} dt}$, during an injection process with a constant flow rate is shown with the solid lines in figure 3.10 for $V_0 = 0.01$, $V_f = 0.9$ and $\theta = 10$. For reference, we include the Newtonian case (black), and a series of shear-thinning cases: $m = 0.99$ (blue), $m = 0.95$ (red) and $m = 0.78$ (yellow). The figure illustrates that the effect of shear-thinning is to cause a small increase in the amplitude of perturbations when the unperturbed pressure gradients are the same as in the Newtonian case. We now seek

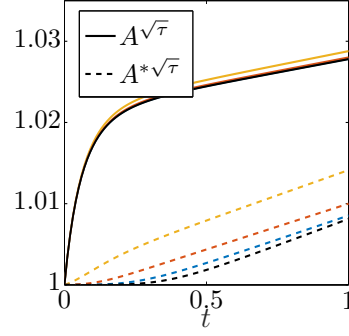


Fig. 3.10 Evolution of amplitudes for a shear-thinning fluid in which the apparent viscosity ratio varies according to $V_0 = 0.01$, $V_f = 0.9$ and $\theta = 10$ for constant injection ($U = 1$; solid lines) and a series of values of m that decreases from the Newtonian case ($m = 1$; black) at bottom of the figure upwards: $m = 0.99$ (blue), $m = 0.95$ (red) and $m = 0.78$ (yellow). Also included are the evolution of amplitudes in the case of optimal injection (*cf.* figure 3.11(a)) broken lines).

to minimise the final amplitude of perturbations in the case in which a finite volume of fluid is injected in finite time.

Following the previous sections, substitution of (3.34) into (3.7) leads to the scalar ODE for $U(t)$

$$\nu(t)^4 U(t)^{5m-1} \sum_{i=1}^5 \left[\nu(t)^{-i} U(t)^{-i(m-1)} \left(\Xi(m)_{i1} \dot{\nu}(t) U(t) + \Xi(m)_{i2} \nu(t) \dot{U}(t) \right) \right] = 0, \quad (3.35)$$

where $\Xi(m) =$

$$\begin{pmatrix} -m(2+m) & -m^2(2+m) \\ -10\sqrt{m} - 5m - 2m^{3/2} + 2m^2 & 2(m - \sqrt{m})(m^2 - 4m - 10\sqrt{m} - 4) \\ -\sqrt{m}(-14 - \sqrt{m} + 8m + 4m^{3/2}) & -\sqrt{m}(4 + 9\sqrt{m} - 24m - 7m^{3/2} + 8m^2 + 4m^{5/2}) \\ (3 + 2\sqrt{m})(1 + 2m) & 2\sqrt{m}(2m^2 + 3m^{3/2} - 5) \\ 0 & -3 \end{pmatrix}.$$

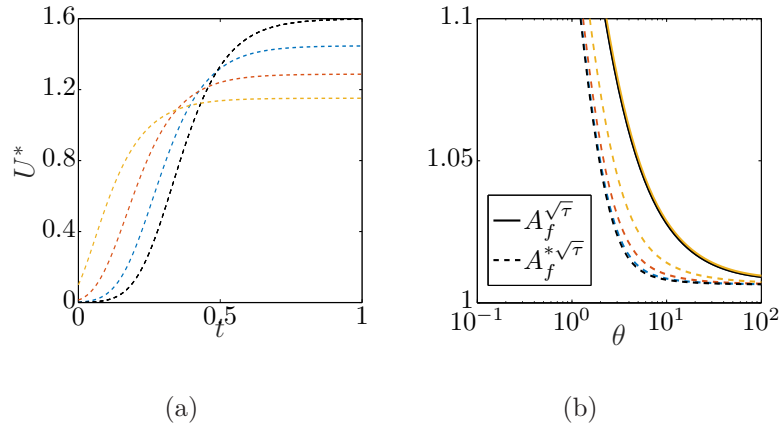


Fig. 3.11 Injection with $V_f = 0.9$. (a) Optimal injection flow rate profiles. (b) Variation of the final amplitude with gelling speed parameter θ for constant injection (solid lines) and optimal injection (broken lines). The values of m in the cases of shear thinning correspond to those in figure 3.10.

The solution of (3.35) is shown in figure 3.11(a) for $m = 1$ (black broken line, *cf.* figure 3.1(b)) and a series of decreasing values of m : $m = 0.99$ (blue), $m = 0.95$ (red) and $m = 0.78$ (yellow) and the variation of $\nu(t)$ defined by (3.13).

When the injection rate is optimal, the proportion of fluid injected later in the flow is reduced compared to the Newtonian case. This is interpreted to be a response to the shear-thinning that would be enhanced with a faster flow rate and which would lead to a more unstable front at later times. This is analogous to the modification of the optimal injection profile for air invading a non-gelling power law fluid in an axisymmetric geometry described by Fontana et al. (2014). The broken lines in figure 3.10 show the evolution of the largest amplitude, $A_f^{\sqrt{\tau}}$, resulting from injection with a variable injection rate as shown in figure 3.11(a). As the flow behaviour index decreases, the final amplitude increases owing to the greater impact of the shear thinning. Figure 3.11(b) shows the variation of the final amplitude with the gelling speed, θ , after the optimal injection as shown in figure 3.11(a) (broken lines) in comparison to the case of constant injection (solid lines). The black lines — which correspond to Newtonian flow — can be recognised from figure 3.2(b), which should be referred to in order to see the behaviour at large or small values of θ where the lines converge

(since if there is effectively no viscosity change then constant injection is optimal). The effect of shear-thinning is to reduce the degree of suppression of the amplitude. For example, for $\theta = 5$ and $m = 0.78$, the degree to which the amplitude is suppressed is approximately halved as compared to the Newtonian case.

3.6 Discussion

In this chapter we have explored the use of the Euler-Lagrange variational framework to find the particular injection rate which leads to a minimisation of the growth of the modes in the Saffman-Taylor instability. We first explored the problem in a rectilinear geometry and found that if the viscosity of the injected fluid gradually increases with time, then it is optimal to increase the injection rate gradually with time, so that more of the injection occurs during the period when the system is more stable.

In a radial geometry the problem is more complex since the azimuthal modes are quantized and the curvature of the interface tends to stabilize the system. As the radius increases, with a constant injection rate, the system becomes unstable to progressively higher modes leading to a shift in the mode of highest amplitude as a function of time. This leads to a difference in the optimal injection strategy depending on the average injection rate over time. With a relatively slow mean injection rate, the optimal strategy involves a gradual decrease in the injection rate with time, consistently with earlier predictions (Beeson-Jones and Woods, 2015; Cardoso and Woods, 1995), whereas with a faster injection rate, the optimal strategy involves a gradual increase in the injection rate with time (Dias et al., 2012), so that less time is spent at conditions near the maximum growth rate of each mode. In this way, the overall amplitude of the perturbations can be reduced.

In the radial system, if the viscosity of the injected fluid gradually increases with time, then the variational calculus suggests that the optimal injection rate should increase at a faster rate with time than the optimal rate in the constant viscosity case, so that more of the fluid is injected once its viscosity has increased. This involves

commencing the injection more slowly but then gradually building up the injection rate with time beyond the case of constant viscosity.

Although these results are based on linear stability theory, they point to the significant benefits of controlling the injection rate in order to control the growth of viscous instability and of the merits in optimising the deployment of a polymer if the injected fluid is changing in viscosity with time. There are several interesting developments of this approach which merit further analysis. First, in some cases it may be that there is a background level of noise, and in this case, the amplitude of each mode would remain at least as large as this noise threshold for all time. It would be fascinating to explore the effect of such a forcing on the present problem. Secondly, the present analysis only explores the linear phase of the growth of an instability. In many cases, the instability may grow to have nonlinear effects, and it is not clear how the optimal injection strategy should evolve once the instability has become nonlinear. To this end, Huang and Chen (2015) and Chen and Yan (2017) have shown that injection with a linearly increasing injection rate can suppress instability as the amplitude increases into the nonlinear regime for flow both in a Hele-Shaw cell and a porous medium. However, it is not clear whether a variable injection rate will influence the ultimate development of a fractal pattern of fingering (*e.g.* Praud and Swinney (2005)), and this would be of interest to explore in future work.

Chapter 4

The dynamics and control of late-stage viscous fingering

4.1 Summary

The nonlinear evolution of patterns formed during the injection of an inviscid fluid into a viscous fluid in a Hele-Shaw cell is analysed through annularly averaged saturation distributions. The displacement begins from close to the injection point rather than at a large distance from it. Three injection conditions are considered: constant flow rate, linearly increasing flow rate and constant inlet pressure. For comparison, we perform a series of off-lattice Diffusion Limited Aggregation (DLA) numerical simulations. We show how the saturation distributions can be divided into a growing region, where pattern development is concentrated, and a frozen region in which there is almost no growth. For viscous fingering, there is additionally a fully saturated region in the vicinity of the inlet. In the frozen region, the saturation approximately varies according to the fractal dimension $\mathcal{D} = 1.70$. In the growing region, the saturation decreases linearly with radius until reaching zero at the outer edge of the pattern and also depends on \mathcal{D} . For DLA, the maximum radial extent of the pattern is 1.54 ± 0.08 times larger than that of the frozen region throughout development. For VF, this ratio is found to be 1.40 ± 0.07 following a period of evolution. This observation

provides a basis to predict the evolution of the radii of the pattern. The extents of the overall pattern and the frozen region relative to the extent of the inner-most fully-saturated region are found to be approximately independent of the injection scheme and correspond to those values for DLA. However, the extent of the fully-saturated region does depend on the injection scheme.

4.2 Introduction

4.2.1 Viscous Fingering and the Confinement of Growth

When water is used to displace oil during the recovery of oil from subsurface oil reservoirs, the interface between the fluids can become subject to viscous fingering (VF). In VF, fingers of the less viscous fluid invade the more viscous fluid (Hill, 1952; Saffman and Taylor, 1958). The problem of predicting the behaviour of the interface has been approached by a variety of methods including the theoretical (Saffman and Taylor, 1958), the experimental (McCloud and Maher, 1995) and the computational (Li et al., 2007). Whilst a number of studies have explored porous media flows, the Hele-Shaw cell is commonly used as a simplified analogue to porous media to make progress in understanding the basic mechanisms of VF (Homsy, 1987). Whilst the stability of an interface can be found from linear stability analysis (LSA; Saffman and Taylor (1958)), as the instability develops the fingers become large in amplitude and nonlinear calculations are needed in order to determine the shape of fingers. The behaviour of nonlinear fingers in a Hele-Shaw cell is controlled by the geometry of the confinement imposed by the cell. Lajeunesse and Couder (2000) explored the impact of the confinement. If, for example, the finger is a significant width of a rectilinear channel, confinement is strong and one finger with a stable shape forms (Saffman and Taylor, 1958). The shape of that finger is well understood (Tanveer, 1987). When the confinement is weak, the shape of the finger is unstable and the tip-splitting instability occurs. This tip-splitting behaviour is seen in an axisymmetric geometry (Couder, 1988), in which the fingers behave as if they are in virtual wedge-shaped

cells (Thomé et al., 1989). The nature of heavily branched nonlinear viscous fingering is too complex for the exact shape of fingers to be determined, thus bulk properties are used to describe the pattern. As we shall describe, the fractal dimension – \mathcal{D} – is one such bulk property. However, reports of the fractal dimension in the literature are inconsistent. Before going into more detail on the various reports of the fractal dimension as applied to viscous fingering, we shall first describe what a fractal object is and the various methods of determination of the fractal dimension.

4.2.2 Fractal Objects, Diffusion Limited Aggregation and the Determination of the Fractal Dimension

If one were to measure the area of a square with a number of measuring squares, N , then if the side length of the measuring squares, ϵ , is halved, the number of squares needed to cover that space would quadruple according to the relationship $N \sim \epsilon^{-2}$. This is because the object is two dimensional. In contrast, the Sierpinski gasket set is comprised of an equilateral triangle that is then recursively subdivided into three equally-sized smaller equilateral triangles (Meakin, 1998). If this shape's area were to be measured with a number of measuring triangles, N , of side length ϵ , then as the length of the measuring triangle is halved, it would be found that three times the number are required to most precisely measure the area. This finding would follow the relationship $N \sim \epsilon^{-\log(3)/\log(2)}$. In comparison to the square, the spatial dimension is fractional and is therefore referred to as a fractal dimension. In this context, the fractal dimension is defined as \mathcal{D} in the relationship

$$N \sim \epsilon^{-\mathcal{D}}. \quad (4.1)$$

The box-counting method is one method of determining the fractal dimension of a pattern (Foroutan-pour et al., 1999). In the box-counting algorithm, the number of boxes, N , of a particular size, ϵ , required to cover (or cover the edges of) an object is determined. Then, the side length of the boxes is decreased, and the new number of

boxes required to cover the shape is determined. The box-counting fractal dimension is found by evaluating $-\text{dlog}(N)/\text{dlog}(\epsilon)$. In the cases of the Sierpinski gasket and the square, this dimension would be measured at all length scales since they are infinitely self-similar sets. In contrast, in real-world objects, as the measuring boxes become smaller than the smallest length scale present in the object, such self similarity will cease. Real-world objects may be described as fractal if they have a consistent fractal dimension – as measured in this way – over a range of length scales. One example of a self-similar fractal object is that which results from Diffusion Limited Aggregation (DLA), a computational process that gives rise to a consistent fractal dimension down to the smallest length scales present in the simulation, as we shall now discuss.

In DLA, a particle is released and randomly walks until it collides with and then sticks to a growing cluster of the particle's predecessors, at which point the next particle is released (Witten and Sander, 1981). The process can produce patterns that are strikingly similar in appearance to VF (Praud and Swinney (2005)). Daccord et al. (1986) describe the mathematical connections between DLA and viscous fingering as follows. In the case that the fluids are incompressible and the displacing fluid is of negligible viscosity, then the pressure field, \mathbf{p} , in the displaced fluid obeys a Laplace equation, $\nabla^2 \mathbf{p} = 0$. In an analogous fashion, the local probability field of the randomly-walking particle in DLA obeys this equation. Mathiesen et al. (2006) further explore mathematical similarities between the two processes, and find them to belong to the same "scaling universality class". Praud and Swinney (2005) highlight the various methods that have been used to simulate DLA and list the fractal dimension measurements. The most precise two results they mention are from the work of Ossadnik (1991) and Davidovitch et al. (2000), who used an off-lattice simulation and conformal map theory to find $\mathcal{D} = 1.712 \pm 0.003$ and $\mathcal{D} = 1.713 \pm 0.003$ respectively. Witten and Sander (1981) stated that the number of particles, N_p , enclosed by a radius R is

$$N_p \sim R^{\mathcal{D}}. \quad (4.2)$$

This is closely related to (4.1) since it is also a law that describes how the measured pattern area varies with the scale of observation in self-similar objects. Witten and Sander (1981) showed that DLA obeys this law and therefore that the aggregate is a fractal object. On account of the connections to VF, attention has been given to assess the fractal dimension of VF. We shall now introduce the main methods to evaluate the fractal dimension, before going on to discuss studies that applied these methods to VF.

A variety of different methods have been established to estimate the fractal dimension, including: (i) the box-counting method (Foroutan-pour et al., 1999), as mentioned before, (ii) correlation-correlation (used by Witten and Sander (1981)), (iii) comparing the radius of gyration of the pattern to the area (used by May and Maher (1989)) and (iv) comparing the density, N_p/R^2 , of the pattern to the total area (used by Chen (1989)). In the case of the patterns formed in their experiments, Praud and Swinney (2005) found that methods (i) and (ii) are equivalent, whereas (ii) and (iii) were found to be approximately equivalent by Daccord et al. (1986). Method (iv) has not explicitly been checked for consistency with the other methods, and has only directly been used by Chen (1989). This method follows from (4.2) if a particle in DLA is equivalent to a small unit of area in VF. We shall proceed by assuming that these methods are at least approximately equivalent, although there will be more discussion on this subject later in the chapter. We will now give a brief overview of three key studies that have investigated the weakly confined VF regime (Chen, 1989; May and Maher, 1989; Praud and Swinney, 2005). We shall discuss the work done to characterise the final VF pattern, before going on to discuss dynamical aspects.

4.2.3 The Fractal Dimension of Viscous Fingering Patterns

May and Maher (1989) investigated weakly confined VF patterns in the case of a constant injection flow rate, whereas Praud and Swinney (2005) investigated the case of a constant inlet pressure, which leads to a gradually increasing injection flow rate. In both cases, the value of \mathcal{D} was found. Praud and Swinney (2005) injected air at very

large flow rates, to the extent that an asymptotic pattern formed. Praud and Swinney (2005) used the box-counting method to measure the patterns' fractal dimension as $\mathcal{D} = 1.70 \pm 0.02$ across all the experiments over a decade of box sizes. This finding is consistent with the fractal dimension found by Ossadnik (1991) for DLA. Praud and Swinney (2005) state that it is only in this asymptotic case of a very large flow rate that the value of \mathcal{D} is expected to converge to this value. Praud and Swinney (2005) also stipulated that the wavelength of the instability must be constant during the injection in order that the system converge to a DLA-like fractal dimension. This condition was met in their experiments since the constant pressure condition gives rise to an approximately constant tip velocity (Thomé et al., 1989), and therefore a constant wavelength of instability. To compare these findings to those of May and Maher (1989), we define the non-dimensional flow rate:

$$C = \frac{\mu Q}{\sigma b}, \quad (4.3)$$

where μ is the viscosity of the displaced fluid, Q is the injection flow rate, σ is the interfacial tension and b is the plate separation. May and Maher (1989) investigated the range of flow rates $0 < C < 60$ whereas Praud and Swinney (2005) investigated $100 < \bar{C} < 700$, where \bar{C} is the mean flow rate. May and Maher (1989) found the value of the fractal dimension of the fingering pattern was 1.71 ± 0.04 for their experiments with injection flow rates in the range $10 < C < 40$. This is inconsistent with the claim of Praud and Swinney (2005), that very large flow rates, C , are required to bring about this value of the fractal dimension and surprising since at such modest flow rates the action of surface tension in shaping the fingers is apparent by inspection of the patterns. Furthermore, with this constant injection flux, the tip velocity gradually slows: it is not constant. In the range of injection flow rates $40 < C < 60$, May and Maher (1989) found the fractal dimension slowly increased to the value $\mathcal{D} = 1.79 \pm 0.04$. We note that May and Maher (1989) measured the fractal dimension by comparing the radius of gyration to the area of the pattern, and assumed that the pattern was fractal on account of the power-law relationship between these two properties.

Like May and Maher (1989), Chen (1989) investigated the case of constant injection flow rate. He defined the pattern density, at a certain radius, as the fraction of the total area contained in that radius that is occupied by air. The fractal dimension was found by measuring the gradient of the region in which there was a linear relation between log-density and log-radius. It was stated that a number of generations of tip splitting are required to bring about fractal behaviour, and this explained why only the experiment with the largest flow rate, $C = 19$, exhibited a linear region in the density-radius plot. For this experiment, he found from successive plots that the fractal dimension decreased from $\mathcal{D} = 1.9$ to $\mathcal{D} = 1.8$ over the course of the injection. This is inconsistent with the data of May and Maher (1989), who found the fractal dimension to be 1.71 ± 0.04 for this value of C . Furthermore, the observation that the dimension evolves with time is inconsistent with the observation of Praud and Swinney (2005) that growth of the pattern is concentrated at the tips whilst the inner portion of the pattern is frozen, and provides a channel for the fluid to reach the outer growing part of the domain. Chen (1989) found a scaling law for the time evolution of the overall radius of the pattern, but he did not attempt to describe the extent of the fractal region or the behaviour of the mass distribution at larger radii.

In summary, all these previous studies were centred on the description of viscous fingers in terms of a fractal dimension of the fingering pattern and the results are inconsistent. The rate of advance of the leading edge of the fingering pattern, the variation of the saturation in this leading part of the flow, and the relation between the radius of the leading edge and the radius of the region in which the fingers follow a fractal dimension has had much less analysis. This forms the main content of this chapter. To this end, we re-analyse the published data and we carry out a series of new experiments. In the case of constant pressure injection, Praud and Swinney (2005) kindly shared the time series from their experiments with us, and so we have examined this data as well.

The third interesting class of inlet condition corresponding to a linearly increasing injection rate is motivated by the work of Dias et al. (2012). By applying the constraint

of injecting a finite volume of fluid in a finite time, Dias et al. (2012) used variational calculus to find the injection flow rate profile that minimises the final amplitude of perturbations as predicted by linear stability analysis. The result of this calculation was an injection flow rate that linearly increased in time. Injecting in this manner was demonstrated to be an effective means of suppressing the growth of the instability. However, the examples shown in Dias et al. (2012) involved the displacement starting from a radius at some distance from the central inlet. If the starting radius is very small all modes are predicted to be initially stable by linear stability analysis. It has been observed that the first mode to become unstable controls the initial growth whereas if the starting radius is larger a number of modes are linearly unstable and it is the one with the highest growth rate that controls the shape (Martyushev et al., 2015). The optimal injection flow rate profile for a very small initial radius is described in the paper of Dias et al. (2012). Whilst the optimum is not necessarily a linearly increasing profile in this case, it is nonetheless of interest to compare the mass distribution that results from such a displacement to the other injection rates to assess the degree to which the instability is suppressed by this means when the initial radius is very small and the fingers undergo tip splitting. Bischofberger et al. (2015) provided us with data to add to our own for this inlet condition.

Finally we have carried out a similar analysis of the mass distribution of the patterns that arise in DLA given the previously mentioned similarities. We perform DLA calculations and compare results with the new analysis of laboratory experiments.

4.2.4 Chapter Outline

In §4.3, we give an overview of the new laboratory experiments we carried out to model pattern evolution for the constant and linearly increasing injection flow rates. We also include the data shared with us by Praud and Swinney (2005). In §4.4 we illustrate the experimental patterns formed. Subsequently, we find and compare the mass distributions for the various VF experiments and seek a universal model. We then go on to perform a series of off-lattice diffusion limited aggregation calculations

in §4.4.4 for comparison. In §4.5 we attempt to put our results in the context of other VF studies. Finally, in §4.6 we draw some conclusions.

4.3 Experiments

4.3.1 Apparatus, Experimental Conditions and Protocol

In our constant flow rate and linearly increasing ("ramped") flow rate experiments, air was injected into rapeseed oil in a float glass Hele-Shaw cell. The top plate was 1 cm thick and 60 cm in diameter and the bottom plate was 1 cm thick and 55 cm in diameter. Float glass was chosen as the process of toughening glass deforms it, and this was seen to affect early (not included) experiments. The physical properties of the rapeseed oil is shown in table 4.1. Viscosity was measured using a Bohlin CS-50 rheometer, and surface tension with a Kruss DSA 100 tensiometer. Following the experimental design of May and Maher (1989), the gap width was set with three positioning micrometers. Air was injected through a 1 cm hole in the centre of the top plate via two syringe pumps (World Precision Instruments AL1000-220). The Hele-Shaw cell was immersed in a reservoir of rapeseed oil. Experiments labelled C1-C3 and R1-R3 were performed by us with this apparatus. The top plate was painted white to help visualisation, and the pattern was filmed with a Canon D90 digital camera from underneath such that the view was not obstructed by delivery tubes.

Experiments from Praud and Swinney (2005) are included in table 4.1 (keys P1-P3). Praud and Swinney (2005) performed constant pressure experiments and achieved non-dimensional flow rates at least an order of magnitude larger than other studies, by using 6 cm thick optically polished glass to attain a uniform 0.127 mm gap. This thickness prevented deflection even at the large values of forcing involved in their experiments. They injected air into silicone oil.

Also included are two previously unpublished experiments provided to us by Bischofberger et al. (2015) (keys C4 and R4). Those authors used two glass plates of thickness 1.9 cm and radius 14 cm.

Table 4.1 Experimental setup. Experiments C1-C3 and R1-R3 were performed by the authors of this chapter, whereas P1-P3 were performed by Praud and Swinney (2005) and C4 and R4 were performed by Bischofberger et al. (2015).

Type	Key	b [mm]	ΔP [atm]	Fluids	μ [Pa s]	σ [N/m]
Constant flow	C1	1.5		air/rapeseed oil	0.050	0.03
Constant flow	C2	1.5		air/rapeseed oil	0.050	0.03
Constant flow	C3	1.0		air/rapeseed oil	0.050	0.03
Constant flow	C4	0.254		water/silicone oil	0.297	0.027
Constant pressure	P1	0.127	0.25	air/silicone oil	0.345	0.021
Constant pressure	P2	0.127	0.50	air/silicone oil	0.345	0.021
Constant pressure	P3	0.127	1.25	air/silicone oil	0.345	0.021
Ramped flow	R1	1.5		air/rapeseed oil	0.050	0.03
Ramped flow	R2	1.0		air/rapeseed oil	0.050	0.03
Ramped flow	R3	1.0		air/rapeseed oil	0.050	0.03
Ramped flow	R4	0.127		water/silicone oil	0.847	0.027

4.4 Results

In this section, we present the measured areal flow rates and then go on to describe and compare the patterns formed. We then develop a mass distribution model for these patterns. Finally, we perform a series of DLA simulations and compare the mass distribution to viscous fingering.

4.4.1 Measured Flow Rates

A MATLAB script was written for this project to detect the boundaries of the evolving pattern and extract properties such as the area enclosed and furthest distance to a finger tip. The sequence of MATLAB functions used are included in an appendix to this chapter (§4.7). The boundary detection was monitored at each step.

Figure 4.1 shows the evolution of the pattern area over the course of the experiments. In each case, we use least-squares regression to fit the data to a power-law relation, $A = A_1 t^{A'}$, shown as the broken black lines. The measured values of A_1 and A' are shown in table 4.2 with 95% confidence intervals shown in brackets. The injection flow rate is determined from this best-fit line as $Q = dA/dt = \beta t^\alpha$. The values of β and α are also shown in table 4.2. Table 4.2 also shows the time-averaged measured

Table 4.2 Measured area and flow rate.

Key	A_1 [cm ² /s ^{4'}]	A'	β [cm ² /s ^(1+α)]	α	\bar{Q} [cm ² /s]	\bar{Q}_p [cm ² /s]	\bar{C}
C1	112(109,114)	1.00 (0.99, 1.01)	110	0.0	112	110	12
C2	186(184,188)	0.97 (0.96, 0.97)	180	0.0	183	180	21
C3	245(241, 249)	0.95 (0.92, 0.97)	230	0.0	236	230	40
C4	7.97(7.94, 8.00)	1.00 (1.00, 1.01)	8.0	0.0	8.0	8.0	35
P1	1.81(1.69,1.93)	1.50 (1.47, 1.53)	2.7	0.5	6.5	(-)	110
P2	5.20(4.90, 1.39)	1.43 (1.34, 1.46)	7.4	0.4	11	(-)	180
P3	16.9(16.6,17.1)	1.60 (1.57, 1.62)	27	0.6	27	(-)	440
R1	10.2(9.5,10.9)	2.10 (2.05, 2.15)	21	1.1	69	70	7.8
R2	28.6(27.0,30.1)	1.83 (1.78, 1.87)	52	0.8	87	85	14
R3	26.2(24.0,28.4)	2.01 (1.94, 2.08)	52	0.9	95	110	16
R4	0.27(0.28,0.28)	2.02 (2.01, 2.02)	0.55	1.0	2.8	(-)	69

flow rate, \bar{Q} , and the time-averaged flow rate with which the injection pumps were programmed, \bar{Q}_p , in the cases that it is known. Finally, we present the nondimensional flow rate. The value of C is constant for the constant flow rate experiments, whereas a mean value – \bar{C} , based on \bar{Q} – is presented for the experiments that feature a gradually changing flow rate.

For the experiments with a constant flow rate, the variation of area is approximately linear. However, for the experiments with larger flow rates, the time exponent becomes progressively smaller than 1, suggesting there is either a degree of plate lift or air compression in these cases. Experiments C1 and C4 show excellent agreement with a linear fit. The agreement between the measured and programmed time-averaged flow rates is good (within 3%) in all cases.

Figure 4.1(b) relates to the experiments of Praud and Swinney (2005) in which air was injected at constant pressure. The best-fit lines suggest an approximate power-law time dependence of flow rate, with $\alpha = 0.5 \pm 0.1$. The programmed flow rates are unknown.

The experiments featuring a linearly increasing flow rate are shown in figure 4.1(c). The variation of pattern area is approximately parabolic. In experiment R3 there is

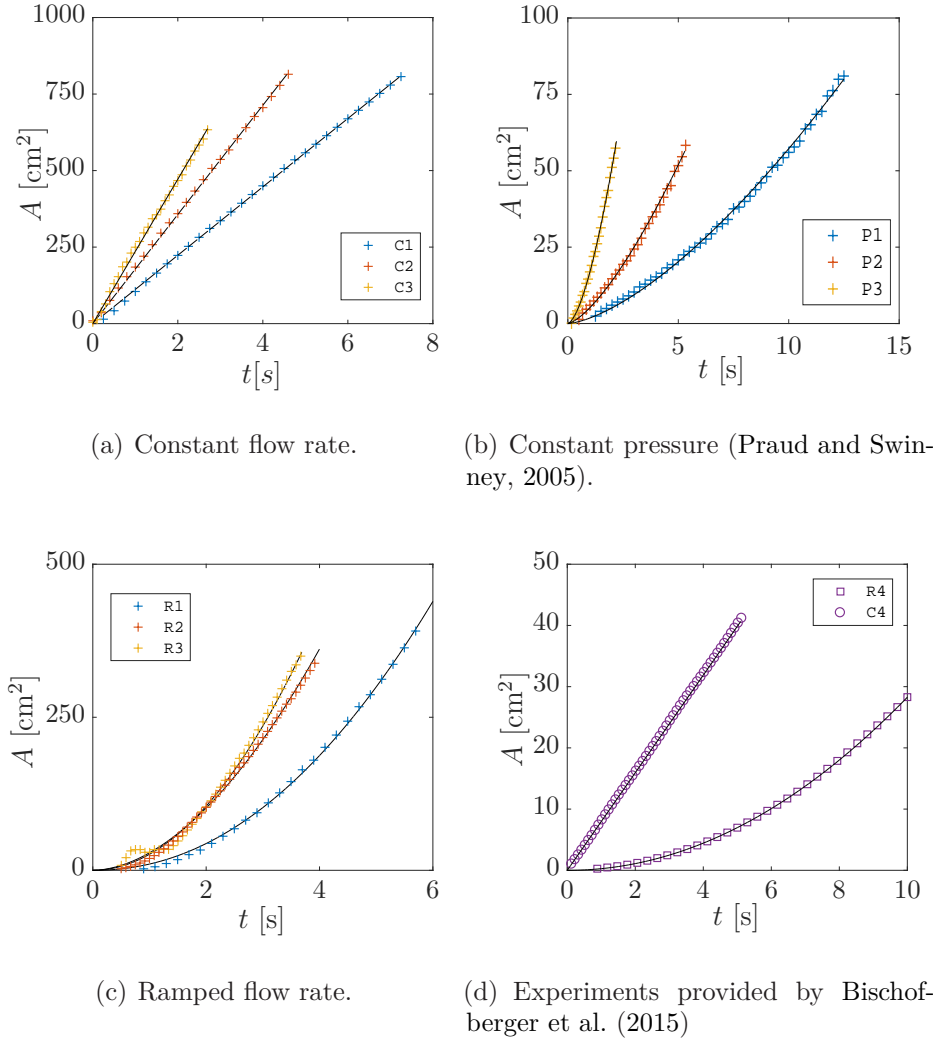


Fig. 4.1 The evolution of the pattern area, A .

considerable deviation (14%) in the measured flow rates from the programmed value, suggesting that plate lift is more severe than in other cases.

4.4.2 VF Pattern Formation

Figure 4.2 illustrates the development of the viscous fingering pattern for a selection of experiments. As was first noted by Paterson (1981), the bases of the fingers – at the bottom of fjords between fingers – become stationary. Conversely, finger growth occurs at the tips. Imperfect tip splitting is observed. This is where one branch grows

at the expense of the other branch, rather than permitting the growth of two long-lived structures (Lajeunesse and Couder, 2000). In the case of the constant flow experiments (top row), there is a larger number of thinner fingers for C3 as compared to C1 and C2, which both feature similar patterns. This could be on account of quantization; that the difference in the value of C is not sufficient to make the next integer mode the most unstable at the time nonlinear growth begins to dominate.

The patterns for the high forcing, constant pressure experiments of Praud and Swinney (2005) (middle row) show a highly branched structure. The width of the fingers appears approximately constant throughout each pattern.

The ramped flow experiments (bottom row) are a return to the less forced patterns; fingers are wider and there are fewer tip-splitting events. The radial extent of the patterns is approximately half that of the constant flow series since the large flow rates involved towards the end of experiments with larger patterns led to plate deformation. The patterns for R2 and R3 are similar and feature a larger number of thinner fingers as compared to the R1 case, for which there is also a large central region that has no fingers.

4.4.3 An Empirical Saturation Model

We define the saturation, $S(R)$, as the fractional area of an annulus at radius R that is taken up by the pattern. The radial variation of S is plotted as a time series in figure 4.3 for three experiments: the constant flow rate experiment for which $C = 12$ (C1), the Praud and Swinney (2005) experiment for which $\Delta P = 0.25$ atm (P1) and the ramped experiment for which $\bar{C} = 14$ (R2). At each time, there is a small inner fully saturated region, outside of which S gradually decreases. At a particular radius, R_{fr} , there is an adjustment from the gradual decrease of S with radius to a region in which there is a steeper and approximately linear decrease with radius until reaching the point $S = 0$. This corresponds to the edge of the growing pattern. For radii smaller than R_{fr} the profile is fixed in time, thus R_{fr} approximately delimits a frozen region

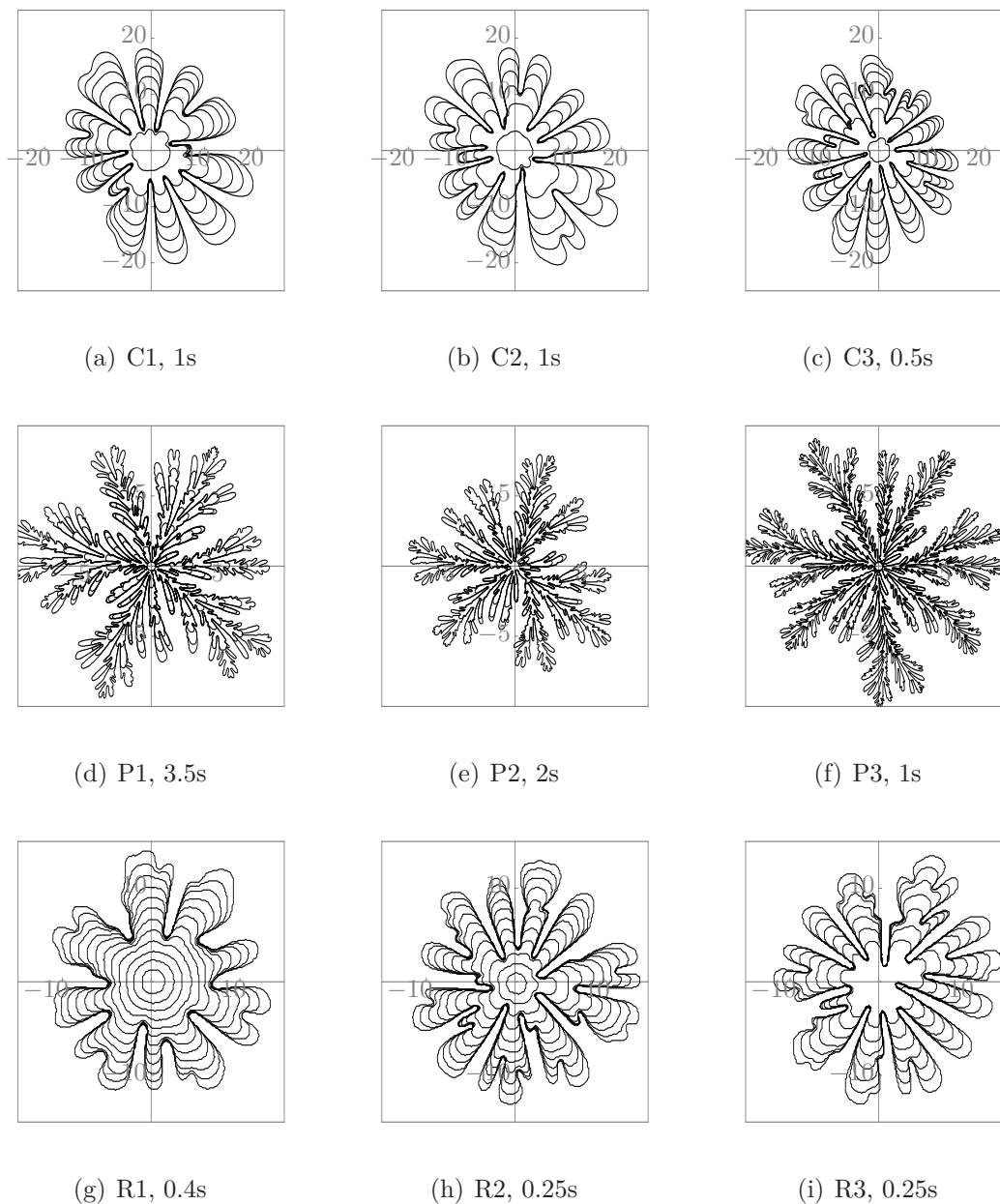


Fig. 4.2 VF pattern development time series for the experiment keys and time intervals, δt , as shown in the captions. Scales in [cm].

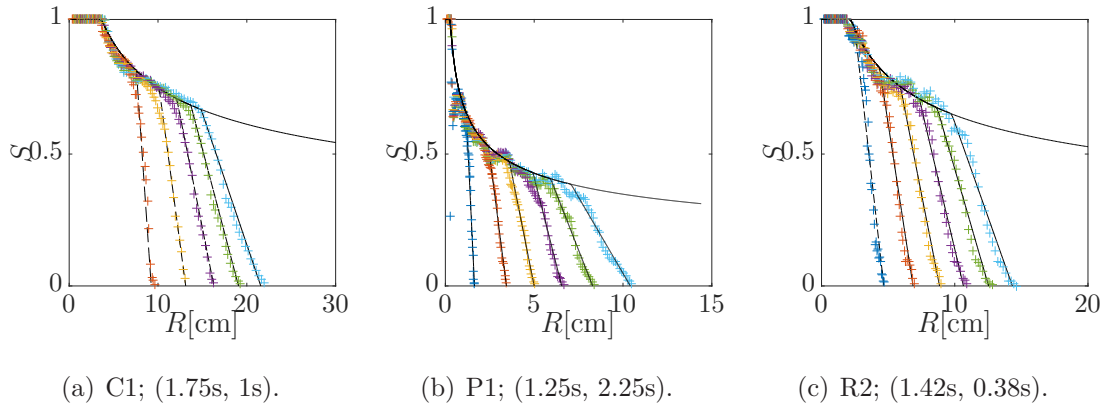


Fig. 4.3 The evolution of saturation for three different examples of inlet condition with the model (4.5) fitted (black lines). The time series are evenly-spaced in time and are shown starting at an initial time t_i at intervals Δt , with these values as shown in the captions as $(t_i, \Delta t)$.

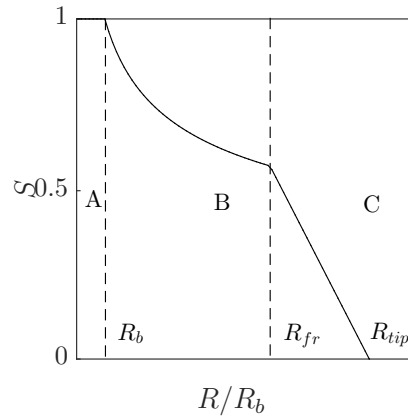


Fig. 4.4 Schematic of the saturation profile.

from an outer region of growth. Figure 4.4 is a schematic of this profile with the fully saturated, frozen and growing regions labelled as A, B and C respectively.

In §4.2.2 we introduced (4.2), which describes the number of particles contained by a radius, R , in a DLA cluster (a fractal object). If – analogous to DLA – viscous fingering also produces fractal patterns then, given (4.2), one expects the saturation profile to be given by

$$S_{fr} = \left(\frac{R}{R_b} \right)^{D-2}. \quad (4.4)$$

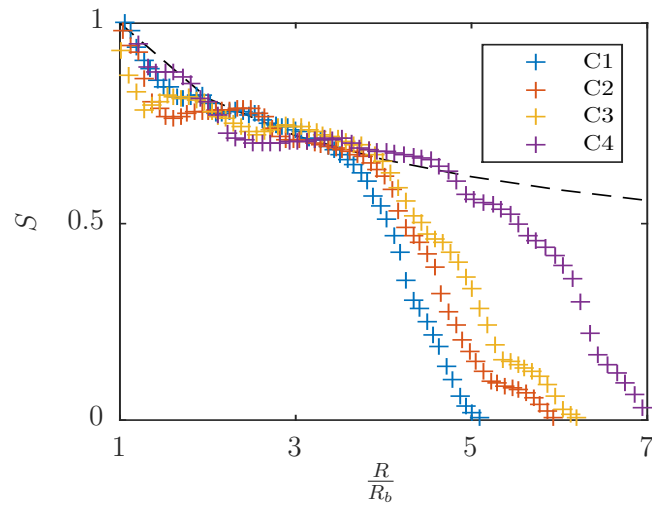
In (4.4), R_b is a fitting parameter which approximately corresponds to the radius of the finger bases, such that $S = 1$ when $R = R_b$. The upper black line in figure 4.3 is a fit of (4.4) with the fractal dimension $\mathcal{D} = 1.70$, the value for viscous fingering found by Praud and Swinney (2005). The complete empirical DLA saturation model is:

$$S(R, t) = \begin{cases} 1, & \text{for } 0 < R \leq R_b \\ \left(\frac{R}{R_b}\right)^{\mathcal{D}-2}, & \text{for } R_b < R \leq R_{fr}(t) \\ \left(\frac{R_{fr}}{R_b}\right)^{\mathcal{D}-2} \frac{R_{tip}(t) - R}{R_{tip}(t) - R_{fr}(t)}, & \text{for } R_{fr}(t) < R < R_{tip}(t) \\ 0, & \text{otherwise.} \end{cases} \quad (4.5)$$

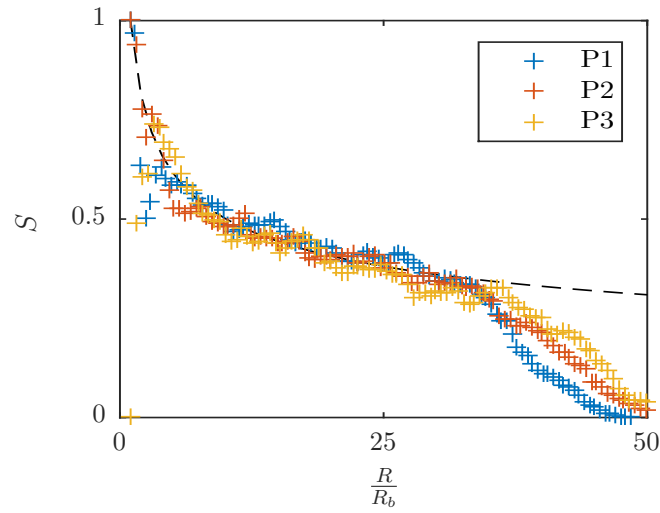
The empirical model appears to fit approximately for each of the experiments shown in figure 4.3, despite differences in the appearances of the patterns and injection conditions. Figure 4.5 shows one time profile from every experiment in this chapter: (a) the constant flow rate experiments, (b) the Praud and Swinney (2005) experiments and (c) the ramped experiments. Table 4.3 also lists the root-mean-squared-error (RMSE) between the data and the model, with $\mathcal{D} = 1.70$ in the frozen region ($RMSE_{fr}$). It is typically around 5% in this region.

The model appears to provide a good fit across almost all of these experiments. The largest $RMSE_{fr}$ is experiment R1. It can be seen from figure 4.5(c) that the approximation is poorer in this case. It is at a lower flow rate and there are fewer splitting events compared to the other patterns. This suggests that tip splitting gives rise to the gradual decrease in saturation that fits the frozen region of the model. In most experiments, there is a dip in S below S_{fr} at small radii; this could be attributed to the shape of the fjord bases. In figure 4.5(a) there is a kink in the saturation at the tip for the C2 and C3 experiments; this could be a result of the finite size of the cell or tips widening ahead of the next generation of splitting.

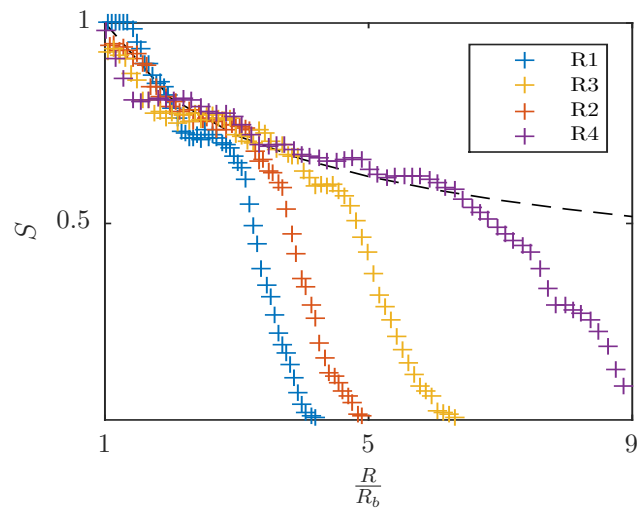
We will now explore the values of R_b , $R_{tip}(t)$ and $R_{fr}(t)$. They are found by fitting the model (4.5). The variation of the fitting parameter R_b in the various experiments is shown scaled with the gap thickness b and varying with \bar{C} in figure 4.6.



(a) Constant flow rate injection: C1-C4 (from left to right).



(b) Constant pressure injection: P1-P3 (from left to right).



(c) Ramped flow rate injection: R1-R3 (from left to right).

Fig. 4.5 The final saturation profile across experiments. In all figures, the broken line is (4.4) with $\mathcal{D} = 1.70$.

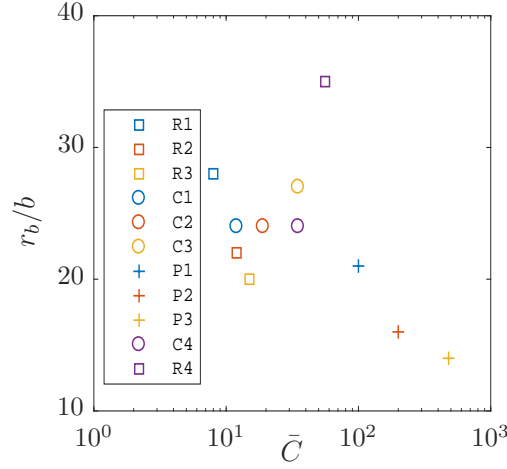


Fig. 4.6 Variation of the fitting parameter R_b with \bar{C} . The experiment key number increases from left to right.

The value of R_b/b declines for the ramped experiments and the constant pressure experiments, whereas for the constant flow rate experiments it appears to be approximately constant. It could be that it is cut-off by the presence of the inlet tube for these experiments. The value of R_b/b is much greater for the experiment R4, provided by Bischofberger et al. (2015), than for the other ramped-flow experiments.

Turning to R_{tip} and R_{fr} , one measure of the structure of the growing pattern is the ratio R_{tip}/R_{fr} , the evolution of which is shown as a function of R_{tip}/b in figure 4.7. The left panel corresponds to the constant flow rate experiments, the centre panel corresponds to the Praud and Swinney (2005) experiments and the right panel corresponds to the ramped experiments. Praud and Swinney (2005) measured the largest angles that could be made between points on the growing, leading edge of the pattern and termed these the unscreened angles. They observed the distribution of these unscreened angles collapse with R_{tip}/b across their experiments. Following their observation, we plot the variation of the ratio R_{tip}/R_{fr} with the quantity R_{tip}/b .

For the Praud and Swinney (2005) data (figure 4.7(b)), there is convergence of R_{tip}/R_{fr} across experiments at around $R_{tip}/b = (R_{tip}/b)_c = 400$, which corresponds to the unscreened angle distribution reaching an asymptotic shape at this radius (*c.f.*

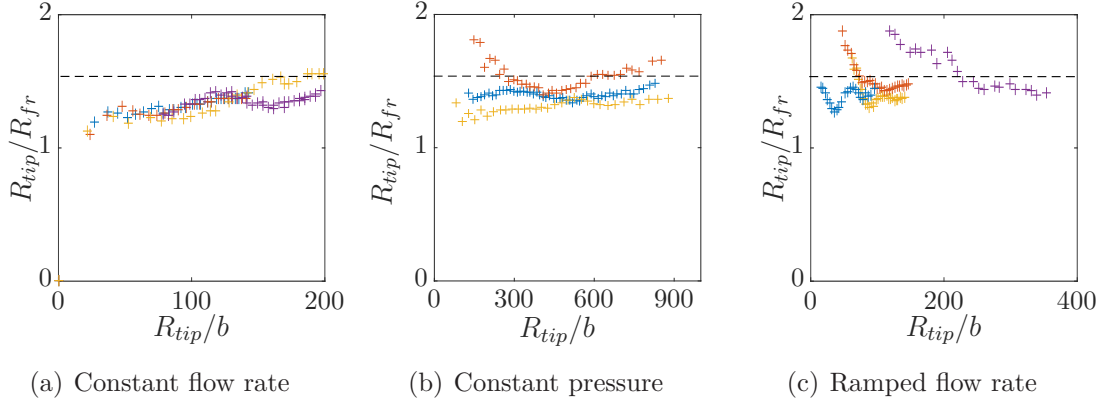


Fig. 4.7 The evolution of the ratio R_{tip}/R_{fr} varying with R_{tip}/b for the injection profiles as labelled (*c.f.* figure 4.5 for legend keys).

Praud and Swinney (2005) Fig. 12), although experiment R2 subsequently diverges somewhat. We define $(R_{tip}/R_{fr})_{\infty}$ as the mean value of R_{tip}/R_{fr} after the tip radius has reached $(R_{tip}/b)_c$. In figure 4.7(b), the value of this ratio is approximately 1.4 throughout the experiments. The values of these measures are summarised in table 4.3 for the different experiments, where the standard deviation of $(R_{tip}/R_{fr})_{\infty}$ is also shown.

In the case of constant flow (figure 4.7(a)), the ratio R_{tip}/R_{fr} builds throughout experiments with $C = 12$ (C1) and $C = 21$ (C2), but appears to reach a plateau at approximately $(R_{tip}/b)_c = 100$ for the experiments with $C = 40$ and $C = 35$ (C3 and C4 respectively). It would be useful to have more later stage data to confirm the asymptotic value since experiments C3 and C4 feature somewhat different values of $(R_{tip}/R_{fr})_{\infty}$.

Figure 4.7(c) shows that for the ramped flow rate experiments, the ratio R_{tip}/R_{fr} tends to a value at around 1.4 for the $\bar{C} = 12$ and $\bar{C} = 15$ experiments (R2 and R3), which collapse with R_{tip}/b at approximately $R_{tip}/R_{fr} = (R_{tip}/b)_c = 100$, whereas the $\bar{C} = 7.6$ (R1) experiment is approximately at this ratio throughout. This ratio also converges to a value of approximately 1.4 for the experiment in which $\bar{C} = 68$ (R4).

The collapse of data with R_{tip}/b in figure 4.7 might be because an asymptotic state is reached in a time that depends on the evolution of the pressure field in the displaced

Table 4.3 The error in the frozen region, $RMSE_{fr}$, and shape parameters of the model.

Key	$RMSE_{fr}$	$(R_{tip}/b)_c$	$(R_{tip}/R_{fr})_\infty$
C1	0.03	100	n/a
C2	0.04	100	n/a
C3	0.05	100	1.53 ± 0.02
C4	0.04	100	1.37 ± 0.05
P1	0.04	400	1.37 ± 0.02
P2	0.03	400	1.45 ± 0.05
P3	0.05	400	1.29 ± 0.04
R1	0.07	100	1.44 ± 0.03
R2	0.03	100	1.33 ± 0.03
R3	0.03	100	1.35 ± 0.02
R4	0.03	200	1.45 ± 0.03

fluid, and thus depends on the radius of the Hele-Shaw cell used. This is supported by the observation that $(R_{tip}/b)_c$ is consistent across experiments performed in the same cell with the same fluids, noting that Bischofberger et al. (2015) used the same cell but different fluids in C4 and R4. The ratio $(R_{tip}/R_{fr})_\infty$ is similar across experiments. We define Γ as the mean value from these experiments and find $\Gamma = 1.40$ with a standard deviation of 0.07. We proceed by exploring the hypothesis that this is a constant, universal to viscous fingering.

The saturation profile in the linear region can now be rewritten as

$$S(R, t) = \left(\frac{R_{fr}}{R_b}\right)^{\mathcal{D}-2} \frac{\Gamma - R/R_{fr}}{\Gamma - 1}, \quad (4.6)$$

for $R_{fr}(t) < R < \Gamma R_{fr}(t)$. The model for saturation can be integrated to give the total injected volume. If the volume of the small central fully saturated region, $0 < R < R_b$, is neglected, the integration gives

$$\begin{aligned} \int_0^t Q dt' &= \int_0^{R_{fr}} \left(\frac{R}{R_b}\right)^{\mathcal{D}-2} 2\pi R dR + \int_{R_{fr}}^{\Gamma R_{fr}} \left(\frac{R_{fr}}{R_b}\right)^{\mathcal{D}-2} \frac{\Gamma - R/R_{fr}}{\Gamma - 1} 2\pi R dR \\ &= \frac{\beta t^{1+\alpha}}{1+\alpha} \end{aligned} \quad (4.7)$$

We nondimensionalise with the radius and time at which the linear stability analysis predicts mode 2 first becomes unstable, *i.e.* when viscous destabilisation first overcomes the surface tension of the fluid:

$$t_0 = \left(\left(\frac{\pi(1+\alpha)}{\beta} \right) \left(\frac{b^2\sigma}{\mu\beta} \right)^2 \right)^{1/(3\alpha+1)}, \quad (4.8)$$

$$R_0 = \left(\frac{\beta}{\pi(1+\alpha)} \right)^{\alpha/(3\alpha+1)} \left(\frac{b^2\sigma}{\mu\beta} \right)^{(\alpha+1)/(3\alpha+1)}. \quad (4.9)$$

Performing the integration in (4.7) gives

$$\frac{R_{fr}}{R_0} = K \left(\frac{t}{t_0} \right)^{\frac{1+\alpha}{\mathcal{D}}}, \quad (4.10)$$

$$\text{where } K = \left(\frac{\mathcal{D}\Gamma R_b^{\mathcal{D}-2}\beta t_0^{1+\alpha}}{2\pi(\Gamma + \mathcal{D}(\Gamma - 1)(\Gamma^3 - \Gamma - 1))R_0^{\mathcal{D}}(1+\alpha)} \right)^{(1/\mathcal{D})}.$$

Equation (4.10) predicts the evolution in time of the frozen radius, R_{fr} , by assuming $R_{tip} = \Gamma R_{fr}$. In figure 4.8, we compare the evolution of these radii with the prediction (4.10), shown as the broken line and displayed as text. The evolution of R_{tip} is shown in the left hand column and R_{fr} is shown in the right hand column. The top row corresponds to the constant injection flow rate experiments, the middle to the constant pressure experiments, and the bottom row to the ramped injection experiments.

For the constant flow experiments, (a)-(b), the predictions of R_{tip} and R_{fr} are approximately consistent with the data, whereas the prediction of R_{fr} is only consistent for experiments C3 and C4, *i.e.* the experiments for which the ratio R_{tip}/R_{fr} appeared to reach an asymptotic state (*c.f.* figure 4.7). For the less forced experiments (C1 and C2), the values of R_{tip} and R_{fr} are initially greater than would be predicted and decreases to below the line of prediction.

Figure (c) shows that R_{tip} approximately evolves with a time exponent of 1.0 for P1-P3, consistent with statement that constant pressure injection gives rise to a constant

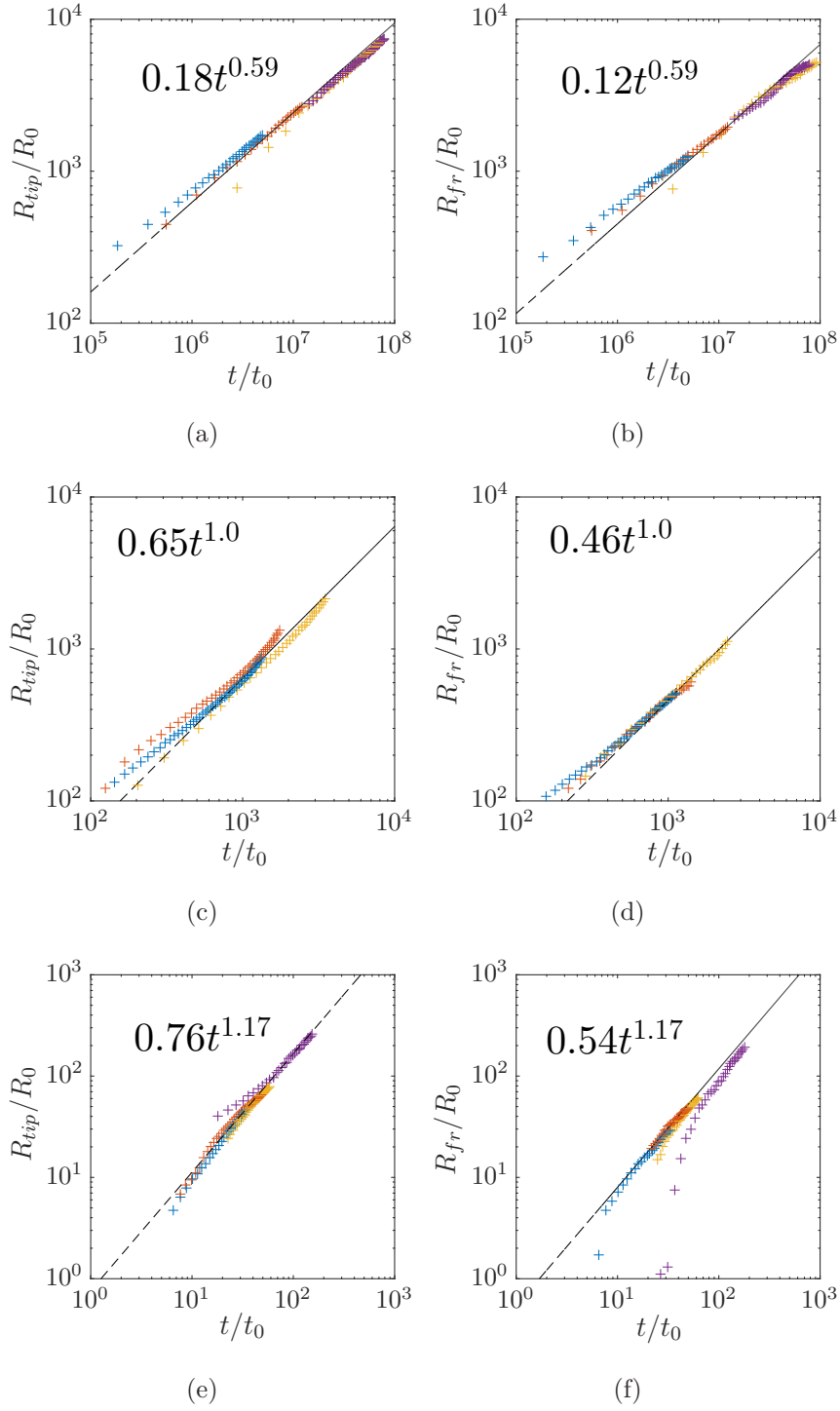


Fig. 4.8 The evolution of the radii R_{tip} (left column) and R_{fr} (right column). Top row: constant injection, middle row: constant pressure, bottom row: ramped injection (*c.f.* figure 4.5 for legend keys; the experiment key number increases from bottom left to top right).

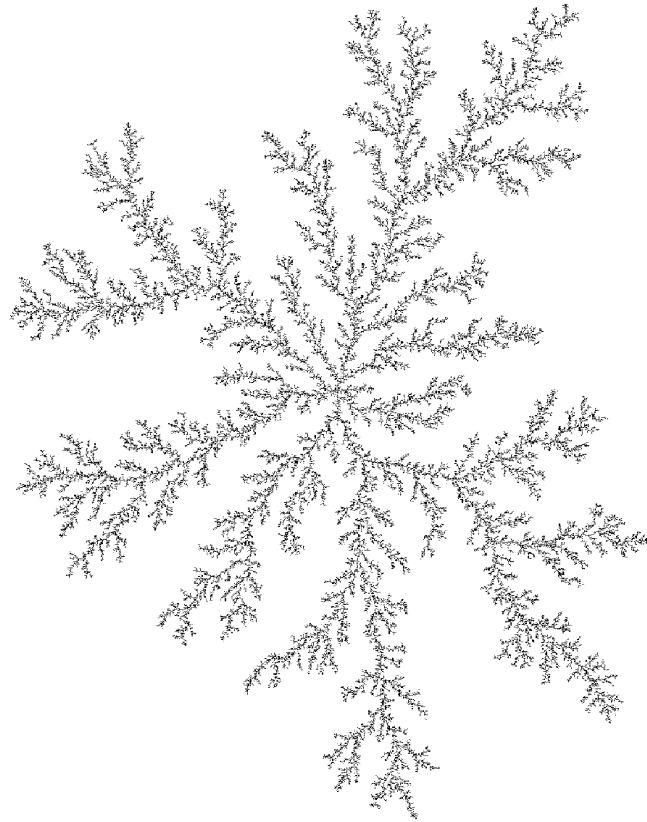
tip velocity (Praud and Swinney, 2005). Figure (d) shows that R_{fr} also approximately evolves with this time exponent.

For the ramped flow rate experiments, (e)-(f), the data approximately agree with the prediction for the tip radius, R_{tip} , whereas for the inner radius, R_{fr} , the series for which $\bar{C} = 69$ (R4) agrees with the predicted power-law dependence only at later stages of pattern growth and remains still somewhat low.

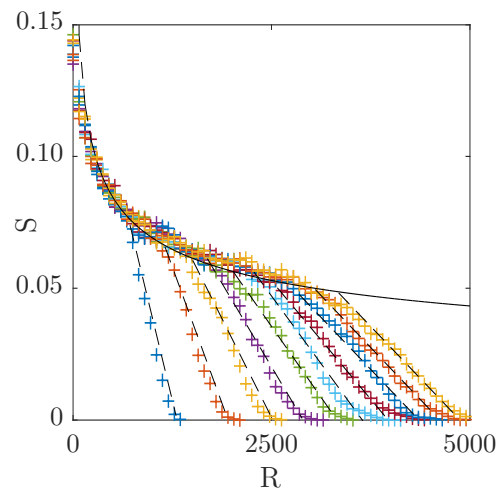
These empirical predictions are derived from assuming the saturation profile is universal. Indeed, it can be seen from (4.7) that the final radii R_{tip} and R_{fr} are functions of the volume injected alone and not the specific injection history if it is valid that the pattern properties $(R_{tip}/R_{fr})_{\infty}$ and \mathcal{D} are consistent across experiments. Before comparing the final values of these radii across experiments, we will first analyse the saturation distribution of a series of Diffusion Limited Aggregation simulations in order to include those results in the comparison too.

4.4.4 Comparison to Diffusion Limited Aggregation

Our aim is to quantitatively compare the growth of viscous instability patterns with that of a Diffusion Limited Aggregation (DLA) cluster. A DLA cluster was simulated using the algorithm developed by Kuijpers et al. (2014). The authors of that study shared their C++ code with us, although it required some bug fixes to compile. We used an overall grid size of 20,000 px, a "distance matrix" grid size of 50 px and a minimum step size of 1 px. The particles were 1 px in radius. Ten clusters were grown, with the number of particles released ranging from 10^5 to 10^6 in equal increments. The final pattern of a 10^6 particle cluster is shown in figure 4.9(a). The radial saturation profile was computed by counting the number of particle centres that fell within a specified range of radii. Figure 4.9(b) shows the resulting distribution, computed using a radial step size of ten times the radius of particles. The mean of seven repeats of the saturation profile of each size is shown, as the saturation profile from a single pattern featured significant noise.



(a)



(b)

Fig. 4.9 (a) A DLA cluster of 10^5 particles. (b) The radial saturation profiles of DLA clusters of size ranging from 10^5 to 10^6 particles in ten equal increments. The simulation to produce each cluster size was repeated seven times, and that shown is the mean saturation of all repeats.

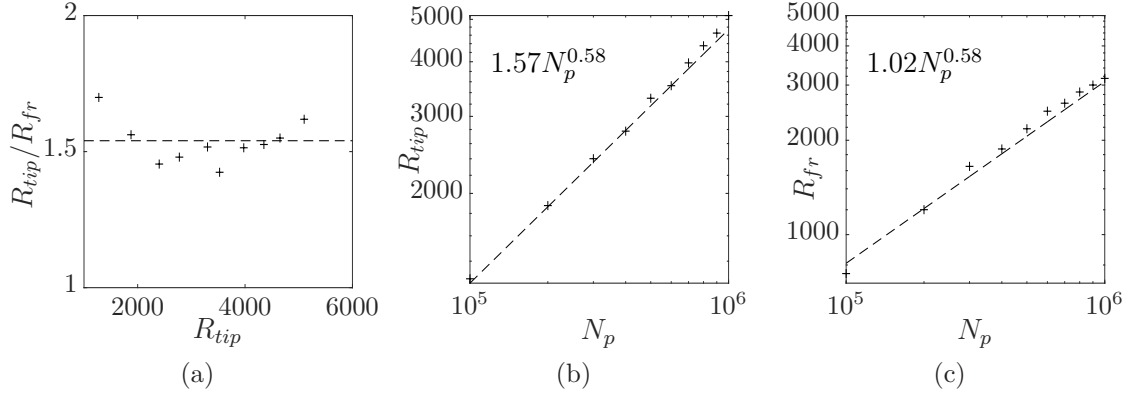


Fig. 4.10 Evolution of (a) the ratio R_{tip}/R_{fr} , (b) R_{tip} and (c) R_{fr} as a function of the number of particles released.

As with viscous fingering, the saturation distribution features a frozen region in which the variation gradually declines and an outer region in which the saturation linearly decreases to zero. In viscous fingering, a base region was observed in which the pattern was fully saturated. This region is absent in these DLA simulations. In the frozen region, $R < R_{fr}$, the saturation distribution varies according to $S = (R/R_b)^{\mathcal{D}-2}$. The variation shows excellent agreement with the fractal dimension reported by Osadnik (1991), $\mathcal{D} = 1.71$, shown as the broken black line, which validates the DLA algorithm we used. Interestingly, the value of R_b – the fitting parameter that defines the base of the saturation distribution in the frozen region – is 0.1. Therefore, it is not until a radius of ten particle radii from the centre of the cluster that the saturation distribution follows the fractal variation.

Following our analysis for viscous fingering, we find the ratio and values of the radii R_{tip} and R_{fr} in figure 4.10.

Figure 4.10(a) shows that R_{tip}/R_{fr} is approximately constant over the range $100 < R_{tip} < 400$. The mean of this ratio is $\Gamma_{DLA} = 1.54$, with standard deviation 0.08. This value is greater than the value for viscous fingering, $\Gamma = 1.40 \pm 0.07$; however, the values are not inconsistent. Figures 4.10(b) and 4.10(c) show that R_{tip} and R_{fr} follow power laws with the same exponent, $N_p^{0.58}$, which is a rearrangement of (4.2), *i.e.* $R_{tip} \sim N_p^{1/\mathcal{D}}$. We shall now compare these results to those of viscous fingering. In

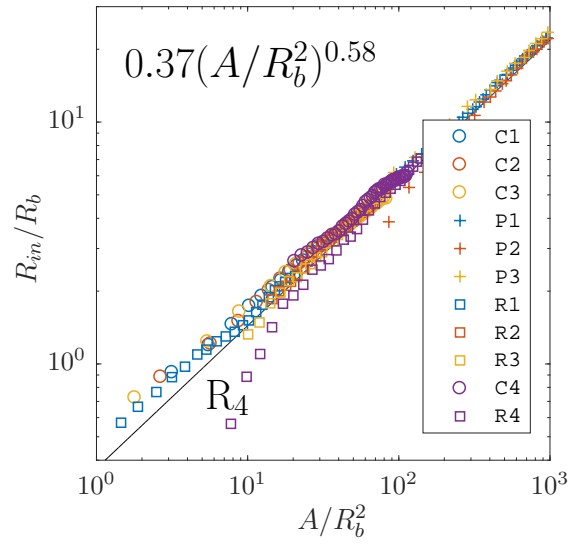
the last section, the evolution of the values of R_{tip} and R_{fr} approximately collapsed when those radii were scaled with R_0 and time with t_0 . These quantities respectively correspond to the radius and time at which linear stability theory predicts that the interface becomes unstable. These constants do not exist for DLA, so instead we choose to scale R_{tip} and R_{fr} with the only scale of length present, R_b . The results are shown in figure 4.11, where the values are shown as a function of the scaled area of the pattern, A/R_b^2 . The broken black lines correspond to the lines of best fit for DLA for R_{tip} (figure 4.11(b)) and R_{fr} (figure 4.11(a)), whereas the data points correspond to those radii for various viscous fingering experiments.

The agreement between the experiments and the simulations is remarkably good, despite the noted differences in the values of \mathcal{D} and $(R_{tip}/R_{fr})_\infty$. Experiment R4 is an exception – the radii only agree with the DLA values at later stages in the flow. That the agreement in figure 4.11 is better than when lengths and time were scaled with R_0 and t_0 is probably on account of experimental uncertainty in those constants. Aside from experiment R4 at early times, to a close approximation the saturation profile is fully defined by \mathcal{D} , $(R_{tip}/R_{fr})_\infty$ and R_b , and only the latter – R_b – depends on the injection history (see figure 4.6). Otherwise, the saturation profiles for viscous fingering are independent of injection history and approximately the same as for DLA.

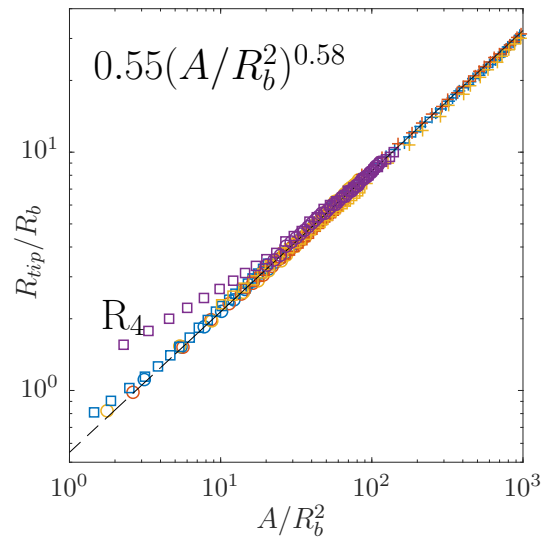
4.5 Discussion

In the experiments presented for which the flow rate is sufficiently high, the variation of saturation in the frozen region is seen to give approximate agreement with that variation in DLA. We will now discuss the conditions under which such behaviour is expected and briefly analyse a number of patterns from other studies in the literature. Finally, we will discuss the methods of measuring the fractal dimension.

Praud and Swinney (2005) suggested a necessary but not sufficient prerequisite for VF and DLA to agree in fractal dimension is that the smallest length scale – the wavelength of instability as predicted by linear stability analysis ($\lambda_{LSA} = \pi b \sqrt{\sigma/(\mu U_{tip})}$)



(a)



(b)

Fig. 4.11 Comparison of the radii R_{in} (a) and R_{tip} (b) for the viscous fingering experiments (points) and DLA (broken lines).

– is constant throughout the pattern during growth, just as the diameter of random walkers in a growing DLA cluster is unchanging. For VF, they stated that λ_{LSA} is constant if the tip velocity is constant. In fact, if λ_{LSA} is on the scale of the plate separation – b – then the actual wavelength of the VF pattern – λ – becomes a fixed multiple of b rather than following λ_{LSA} (Dias and Miranda, 2013b; Kim et al., 2009; Maxworthy, 1989). Indeed, in the case of miscible displacements, for which surface tension is altogether absent so $\lambda_{LSA} \rightarrow 0$, the width of fingers is fixed by viscous dissipation effects to $\lambda \sim 4b$ (Paterson, 1985). Figure 4.12(a) shows the evolution of the tip velocity on the left hand axis and the capillary number, $Ca = U_{tip}\mu/\sigma$, on the right hand axis for the Praud and Swinney (2005) data. Figure 4.12(a) shows that U_{tip} is indeed approximately constant (until the end of the flow when boundary effects become important). However, it is also true that $\lambda_{LSA}/b = \pi/\sqrt{Ca}$ ranges from just 4 to 10, so it is quite possible that the pattern is in the regime where the wavelength of the pattern is fixed by the plate separation and is independent of the tip velocity. This is further supported by the similarity of the patterns across the Praud and Swinney (2005) experiments. Indeed, in figure 4.2, the complexity of the patterns and the width of the fingers do not appear to change considerably for the different inlet conditions. In this regime, it is quite possible that any inlet condition (constant or linearly increasing) could give rise to the same pattern; so long as a threshold tip velocity is maintained it need not be constant for the unstable wavelength, λ , to be fixed.

We now turn to the constant flow rate experiments of this study. The evolution of U_{tip} and Ca for the constant-flow experiments is shown in 4.12(b) for experiments C1 (blue), C2 (red) and C3 (yellow). The value of λ_{LSA}/b ranges from 10 to 20, so the patterns are probably not in a regime where the finger width is controlled by the plate separation alone. The tip decelerates, violating the condition that λ_{LSA} need be constant. Therefore, DLA-like fractal behaviour is not expected by the arguments introduced above, and yet figure 4.5 shows that the variation in the frozen region is reasonably well approximated by $\mathcal{D} = 1.70$, typically within 5% (see table 4.3). Before

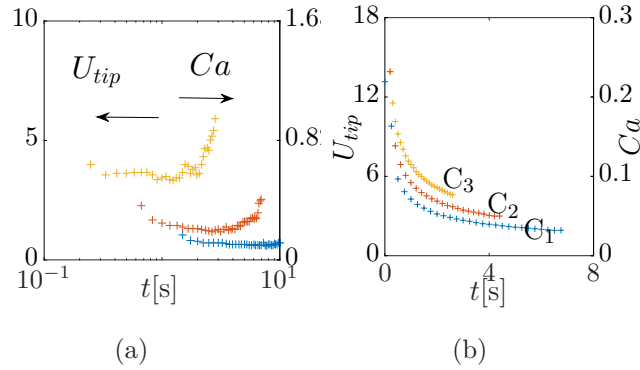


Fig. 4.12 The evolution of U_{tip} [cm/s] (left axis) and Ca (right axis). (a) Praud and Swinney (2005) experiments (bottom to top: P1 to P3). (b) Constant flow rate experiments C1-C3.

addressing this, we turn to other constant flow rate experiments to see if they too are well approximated by the saturation profile for $\mathcal{D} = 1.70$. Figure 4.13 compares the saturation profiles of the final patterns in a variety of constant flow rate studies to the DLA profile (black broken lines).

The saturation profile for the VF pattern illustrated in May and Maher (1989) is included in figure 4.13 as the black series. By comparing the radius of gyration to the area of the pattern, May and Maher (1989) reported a fractal dimension of $\mathcal{D} = 1.8$ for this experiment. It can be seen from the figure that the variation in the frozen region is not inconsistent with $\mathcal{D} = 1.70$, however the frozen region is not very well established. Thus, it could be that the variations in the measured fractal dimension seen in May and Maher (1989) are found because the patterns are yet to reach an asymptotic state in which a more substantial proportion of the pattern is frozen, rather than simply because the injection is of constant flow rate, as suggested by Praud and Swinney (2005). The Thomé et al. (1989) series (yellow) is for a pattern in which the tip splitting is perfect (each splitting event leads to two long-lived structures) and it too gives fair agreement with the DLA saturation profile in the frozen region. Lajeunesse and Couder (2000) present a low flow rate, perfect tip-splitting pattern (blue) and a high flow rate, imperfect tip-splitting pattern (red). The former pattern is very similar to that of May and Maher (1989) – agreement is modest and limited to a

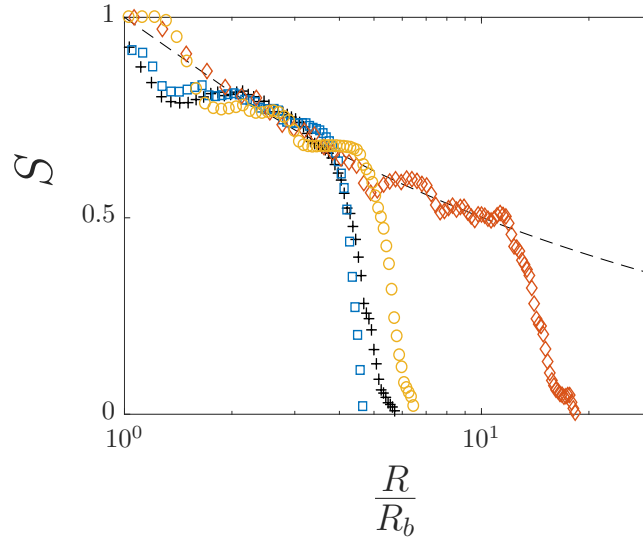


Fig. 4.13 Saturation profiles for the final patterns of May and Maher (1989) (+), Thomé et al. (1989) (o), and Lajeunesse and Couder (2000) (their fig. 17(a) - (boxes) and (fig 17.(b) - (diamonds))).

smaller internal area – whereas in the latter the agreement is more compelling and over a larger range of radii.

One possible conclusion is that the condition for the saturation to approximately vary according to DLA is simply that there are many tip splitting events. This appears to be approximately true even in cases where surface tension acts to widen the fingers as the interface slows.

This suggests that the growing region creates a systematic error in the measurement of the fractal dimension. In figure 4.14, we show the results of the box counting algorithm when applied overall (blue), to the shape that results from masking the growing region (yellow) and to the shape that results from masking the frozen region (red) for (a) the Praud and Swinney (2005) $\Delta P = 1.25$ atm experiment (key: P3) and (b) the constant flow $C = 21$ experiment (C2). In figure 4.14(a), we plot the box-counting fractal dimension, $-\text{dlog}(N)/\text{dlog}(\epsilon)$, against box size ϵ , where ϵ is scaled with ϵ_0 , the resolution of the image (given in the captions). The measurement of \mathcal{D} is approximately constant over the scales $10^0 < \epsilon < 10^2$, with $\mathcal{D} = 1.70 \pm 0.02$, and this indicates self similarity on those scales for the overall shape (blue). When the growing region is masked and the box-counting algorithm is applied to the frozen region alone

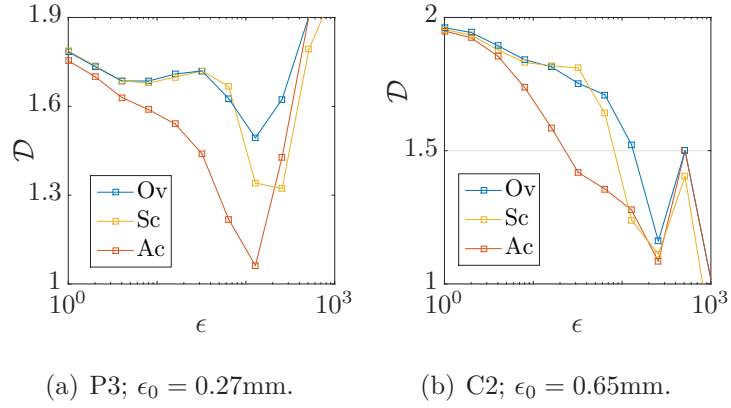


Fig. 4.14 The box counting algorithm applied to different regions of two final VF patterns. From the top series to the bottom: Ov = Overall, Sc = Screened (frozen) and Ac = Active (growth).

(yellow), the measurement is much the same. This is a naive method, since masking the growing region will have an effect on the fractal dimension of the frozen shape as the tips of the fingers near the edge are trimmed, but it nonetheless indicates that for the patterns presented in Praud and Swinney (2005), the box-counting measurement of the fractal dimension is not significantly perturbed by the growing region. This is on account of the large size of the frozen region and the large number of tip-splitting events within it dominating the overall measurement. In contrast, in the final pattern of experiment C2, the measurement of the fractal dimension monotonically decreases indicating that the shape is not self-similar on those length scales and is therefore not a fractal object. Thus, it is quite remarkable that – despite the lack of self similarity – the measured values of R_{tip} approximately agree with the model's predictions, which were based on the fractal dimension for viscous fingering found by Praud and Swinney (2005). Figure 4.14(b) also shows that the result of the box counting method is different when considering the overall pattern rather than the frozen region alone for this less complex pattern.

As a final note, the study of Chen (1989) was mentioned in the introduction, as he also measured the fractal dimension of viscous fingering from the pattern's mass distribution (using the patterns' density, $D(R)$, where $D(R) = \int_0^R 2\pi R S(R) dR$). We have not further discussed the data of Chen (1989) since his density-radius plots

evolved in time at all radii, *i.e.* the frozen region in fact exhibited growth. In that study, the plate separation was 6/10 that of the Praud and Swinney (2005) experiment and the glass 11 times thinner, so it is possible that there was some degree of flexion even though the flow rate is slower than in the Praud and Swinney (2005) experiments.

4.6 Conclusions

In this chapter, we have performed a series of new viscous fingering experiments, re-analysed viscous fingering experiments in the literature and reproduced simulations of Diffusion Limited Aggregation (DLA). We have explored a novel approach to analysing the patterns that form, which reveals features that have not previously been reported. This approach is to find the fraction of the area covered by the fingers in small annuli at all radii, *i.e.* the distribution of saturation of the pattern.

Across all patterns, the evolution of the saturation profile confirms that growth is concentrated at the extremities of the pattern, as has previously been noted. However, the analysis of this chapter has found that there is a well-defined evolving radius, the frozen radius, inside of which the pattern is static and outside of which – in the growth region – the variation of saturation is approximately linear.

The viscous fingering experiments included a set of experiments involving a moderately large constant flow rate, a set of high flow rate experiments involving a constant pressure injection performed by Praud and Swinney (2005) and a set of moderate flow rate "ramped" experiments, in which the flow rate linearly increased. A constant flow rate experiment and a ramped experiment provided by Bischofberger et al. (2015) were also analysed. In all cases, the flow rate was sufficient to induce the tip-splitting instability.

The viscous fingering experiments featured similar saturation profiles to DLA: there were seen to be a frozen region, in which the saturation decreased approximately according to $\mathcal{D} = 1.70$ (to within 5%), and a growth region with linear saturation variation. However, in addition to these radii, in viscous fingering there is additionally

a fully-saturated inner region at radii smaller than the bases of the fingers, that is unseen in DLA. It was generally found that, following a period of development, the outer and inner radii evolve in approximately constant ratio (1.40 with standard deviation 0.07), except in the two slower experiments with constant injection, in which this ratio evolved throughout pattern development. This observation was used to predict that the outer and inner radii of the pattern evolve proportional to $t^{(1+\alpha)/\mathcal{D}}$, where α is the time exponent of the injection flow rate. The data gave approximate agreement with this prediction when the radii and time were scaled with R_0 and t_0 . These constants are the radius and time at which the linear stability theory prediction of the growth rate of mode 2 first becomes positive.

In the DLA simulations, the saturation in the frozen region was seen to vary in good agreement with the fractal dimension that has previously been reported for DLA, $\mathcal{D} = 1.71$ (Ossadnik, 1991). The saturation distribution also reveals that the outer and inner radii of the growing region evolve in approximately constant ratio (1.54 ± 0.08) throughout development.

When the inner and outer radii were scaled with radius of the finger bases and shown varying with the total area of the pattern, the radii in viscous fingering were shown to approximately agree with the values from DLA.

These findings lead to the overall conclusion that in unstable situations – where the nonlinear development of viscous fingering dominates and the tip-splitting instability arises – when injecting fluid with different flow-rate profiles the only difference in the saturation distribution is the extent of the fully-saturated region.

Finally, it was noted that in large and complex patterns that feature self similarity, measuring the fractal dimension of the overall pattern by the box counting method gives a good estimate of the fractal dimension as can be used to predict the saturation distribution. In contrast, in simple patterns that feature only a few generations of tip splitting and lack self similarity, the box-counting method would not be useful for predicting the saturation distribution.

4.7 Appendix

Table 4.4 The image processing MATLAB functions used and a brief description thereof.

VideoReader	Extracts each frame from a movie.
im2bw	Converts frame to a binary image according to the appropriate threshold value (found by trial-and-error).
bwareaopen	Removes any objects smaller than a threshold number of pixels (found by trial-and-error).
Ifill	Fills any holes in the remaining large object.
bwboundaries	Detects the edge of the pattern.
regionprops	Determines pattern properties such as area and perimeter.

Chapter 5

Conclusions

This chapter is split into two sections. §5.1 lists the main contributions to research that have been made from the work in this thesis and §5.2 lists some research ideas that would draw on this thesis.

5.1 Main contributions

The stability of the interface between two immiscible fluids as one is injected into the other from a point source in a two dimensional axisymmetric Hele-Shaw cell was explored. Linear stability analysis of the interface identified that for a specific mode, n , there is a critical viscosity ratio, V_c , required to ensure the absolute stability of that azimuthal mode (§2.3.2). For viscosity ratios less adverse than the critical value, V_c , the azimuthal mode is stable to all injection flow rates, Q . All modes $m < n$ are also stable under such flow conditions. However, higher order modes may still be unstable. We also showed that for a given viscosity ratio, there is a critical flow rate, $Q^*(t)$, such that all modes are stable. This is possible owing to the balance between the gradual stretching of the interface, interfacial tension and viscous destabilisation.

Building on this theory, the case in which a second fluid is injected following injection of the first fluid was also analysed. The two are injected in sequence leading to the formation of a radially spreading annulus of the first injected fluid. The stability

of the annulus depends on the radial extent of the annulus relative to the outer radius of the annulus. If the radial extent of the annulus is large then the growth rates of instability on the leading and trailing interfaces can be considered in isolation (§2.4.1). Generally however, there is coupling of the two interfaces. If the fluid in the annulus is of intermediate viscosity as compared to the bounding fluids then for each azimuthal mode, n , analogously to the single interface case there exists a critical viscosity ratio of the bounding fluids, $V_{\text{upper}}(n)$. For less adverse viscosity ratios the system is stable to that particular azimuthal mode for all injection flow rates, Q , and at all times. There exists another critical viscosity ratio, $V_{\text{lower}}(n)$, below which that particular azimuthal mode is not absolutely stable throughout the injection. For intermediate viscosity ratios, $V_{\text{lower}}(n) < V < V_{\text{upper}}(n)$, that azimuthal mode may be absolutely stable initially but at some later time it becomes unstable on account of the coupling of instability on the interfaces. In an analogous fashion to the single interface case, the balance between destabilising and stabilising effects gives rise to an azimuthal mode which features the largest growth rate in the system (§2.4.3) and this most unstable mode gives rise to an injection flow rate, $Q^*(t)$, such that if $Q < Q^*(t)$ then the interface is dynamically stable (§2.5). Given the viscosities of the bounding fluids, a method was found for choosing the viscosity of the intermediate fluid that minimises the total duration of the dynamically stable injection of the annulus.

In a rectilinear geometry, it may be of interest to determine the injection rate, $U(t)$, such that if a finite volume of fluid is to be injected in a finite time, then the magnitude of any instability of the interface is minimised (§3.3.1). This particular injection rate is found using variational calculus. It is shown that the optimal flow rate strategy is a constant flow rate in the case of an injected fluid with constant viscosity. This analysis is generalised to explore the effect of changes in viscosity of the injected liquid as a function of time. In the case that the viscosity of the injected fluid gradually increases with time, it is found that the optimal injection strategy is adjusted so as to lead to the injection of more fluid later in the flow following the increase in viscosity. It is demonstrated that this strategy can lead to substantial

suppression of instability compared to the case of a constant injection rate (§3.3.2). In the case of an axisymmetric geometry, there are a series of discrete modes. If instead, we assume there is a continuous series of modes, then we can follow a similar analysis and find a time evolving injection rate, $Q(t)$, that minimises the final amplitude of instability (§3.4.1). If the injection rate is sufficiently low, the hypothetical growth rate of instability associated with this continuous bound can be dynamically stabilised by evolving the injection rate according to $Q \sim t^{-1/3}$. In contrast, if the injection is relatively rapid then the optimal injection flow rate is linear in time, $Q \sim t$, a limit found by Dias et al. (2012). In the case of an axisymmetric displacement in which the injected fluid gradually increases in viscosity, the optimal injection flow rate involves injecting more of the fluid following the increase in viscosity than in the constant injection case (§3.4.2).

In many cases of industrial interest, shear-thinning fluids are involved in displacements in thin channels. We have generalised the analysis to consider the minimisation of instability when a finite volume of shear-thinning fluid is injected in a finite time. In the case of the displacement of a shear-thinning fluid in a rectilinear geometry, the optimal injection flow rate involves injecting less fluid later in the flow than in the Newtonian case (§3.5).

In the final part of the thesis, we have examined the nonlinear growth of the viscous fingering instability, and in particular tried to assess how the fingering pattern grows in time. To this end we have analysed the saturation, S , of the fingering pattern as a function of the radius, R , where the saturation is the azimuthal average of the area covered by the fingers of injected fluid. We have found that with the development of a nonlinear fingering regime, there are three main regions: an inner fully saturated region, an intermediate frozen region which is fixed in time, but whose leading edge grows in time, and a growing nose region in which the saturation linearly decreases to zero. The nose region advances radially with time, and in this region the saturation at each point increases with time. The intermediate region has a saturation which follows the law $S \sim R^{-0.30}$ for the experiments. These observations were found for

new experiments in which the injection flow rate was constant or linearly increased and also for a previously published set of data for which the inlet pressure was held constant. After a period of evolution, the radius of the intermediate region is approximately $2/3$ the radius of the overall pattern in all cases. This allowed prediction of the evolution of the radii. It is of interest that these results are largely independent of the injection history. Unlike the linearly stability problem in which we have found optimal injection rates with time, the nonlinear problem seems to evolve largely independently of the specific injection rate. We have also performed numerical calculations of the Diffusion Limited Aggregation (DLA) system and found very similar saturation distributions. The extents of both the tip radius and the frozen zone radius relative to the fully-saturated radius was shown to be approximately the same across all viscous fingering experiments and DLA for a given pattern area.

5.2 Further Work

This thesis has explored the benefits of varying the flow rate during injection of a continuous stream of polymer that is gradually undergoing a change in viscosity. However, towards the end of such an injection in the field, it may be desirable to clean up the well by following the polymer injection with water. Thus, it would be of interest to combine the principles developed in chapters 2 and 3, and explore the benefits of modifying the injection flow rate in the case of the injection of a finite mass of polymer laden fluid and a finite mass of water in series in a finite time. The case of the intermediate polymer laden fluid gradually undergoing a change in viscosity could also be explored. This problem would be complicated by the presence of both the global and local modes of instability. Gorell and Homsy (1983) found the optimal spatial distribution of the concentration of polymer to minimise fingering in the intermediate fluid of a three fluid rectilinear system when the injection flow rate was constant. It would be interesting to find this distribution in an axisymmetric geometry and, draw-

ing on ideas from chapters 2 and 3, explore what potential there is to further suppress instability by varying the injection flow rate in this case.

We have made use of the Hele-Shaw flow analogy to flow in porous media, having acknowledged the limitations of this analogy. Whilst Chen and Yan (2017) have explored the impact of the Dias et al. (2012) variational calculus framework towards minimising instability in porous media, it was a computational treatment and it would be fascinating to explore these principles in a series of porous media experiments. Chen and Yan (2017) also found that the linearly increasing injection rate did not lead to suppression of instability in the case of heterogeneity of the porous medium. A non-uniform gap width in the cross section of a Hele-Shaw cell is analogous to a heterogeneous porous medium. Viscous fingering in such a cell was explored by Woods and Mingotti (2016), and it would be interesting to explore the potential of varying the injection flow rate towards suppressing instability in this case.

The two geometries in which we have investigated flow in this thesis have been the axisymmetric and the rectilinear. It would be of interest to generalise what has been found to source-sink flows, such as the five-spot geometry.

References

- Al-Housseiny, T. T. and Stone, H. A. (2013). Controlling viscous fingering in tapered Hele-Shaw cells. *Physics of Fluids*, 25:092102.
- Bataille, J. (1968). Stabilité d'un écoulement radial non miscible. *Revue Institute Petrole*, 23:1349–1364.
- Batista, C., Dias, E. O., and Miranda, J. A. (2016). Hamiltonian formulation towards minimization of viscous fluid fingering. *Physical Review E*, 94(1):013109.
- Beeson-Jones, T. H. and Woods, A. W. (2015). On the selection of viscosity to suppress the Saffman Taylor instability in a radially spreading annulus. *Journal of Fluid Mechanics*, 782:127–143.
- Beeson-Jones, T. H. and Woods, A. W. (2017). Control of viscous instability by variation of injection rate in a fluid with time-dependent rheology. *Journal of Fluid Mechanics*, 829:214–235.
- Bischofberger, I., Ramachandran, R., and Nagel, S. R. (2015). An island of stability in a sea of fingers: emergent large-scale features of the viscous flow instability. *Soft Matter*, 11(345):7428.
- Brenner, E. A., Kessler, D., Levine, H., and Rappel, W. (1990). Selection of the Viscous Finger in the 90° Geometry. *Europhysics Letters*, 13(2):161–166.
- Callan-Jones, A. C., Joanny, J. F., and Prost, J. (2008). Viscous-fingering-like instability of cell fragments. *Physical Review Letters*, 100(25):258016.
- Cardoso, S. S. S. and Woods, A. W. (1995). The formation of drops through viscous instability. *Journal of Fluid Mechanics*, 289:351–378.
- Carreau, P., DeKee, D., and Daroux, M. (1979). An analysis of the viscous behaviour of polymeric solutions. *Canadian Journal of Chemical Engineering*, 57:135–140.
- Casademunt, J. (2004). Viscous fingering as a paradigm of interfacial pattern formation: Recent results and new challenges. *Chaos*, 14(3):809–824.
- Chen, C. Y. and Yan, P. Y. (2017). Radial flows in heterogeneous porous media with a linear injection scheme. *Computers and Fluids*, 142:30–36.
- Chen, J.-D. (1989). Growth of radial viscous fingers in a Hele-Shaw cell. *Journal of Fluid Mechanics*, 201:223–242.

- Chouke, R. L., van Meurs, P., and van der Poel, C. (1959). The instability of slow, immiscible, viscous liquid-liquid displacements in permeable media. *Petroleum Transactions, AIME*, 216:188–194.
- Combescot, R. and Ben Amar, M. (1991). Selection of Saffman-Taylor Fingers in the Sector Geometry. *Physical Review Letters*, 67(4):453–456.
- Couder, Y. (1988). Viscous Fingering in a Circular Geometry. In Stanley, H. E. and Ostrowsky, N., editors, *Random Fluctuations and Pattern Growth*, pages 75–81. Kluwer Academic Publishers, Dordrecht.
- Cross, M. M. (1965). Rheology of non-Newtonian fluids: A new flow equation for pseudoplastic systems. *Journal of Colloid Science*, 20(5):417–437.
- Daccord, G., Nittmann, J., and Stanley, H. E. (1986). Radial Viscous Fingers and Diffusion-Limited Aggregation: Fractal Dimension and Growth Sites. *Physical Review Letters*, 56(4):336–339.
- Davidovitch, B., Levermann, A., and Procaccia, I. (2000). Convergent calculation of the asymptotic dimension of diffusion limited aggregates: Scaling and renormalization of small clusters. *Phys. Rev. E*, 62:R5919–R5922.
- Dias, E. O., Alvarez-Lacalle, E., Carvalho, M., and Miranda, J. (2012). Minimization of Viscous Fluid Fingering: A Variational Scheme for Optimal Flow Rates. *Physical Review Letters*, 109(14):144502.
- Dias, E. O. and Miranda, J. (2013a). Taper-induced control of viscous fingering in variable-gap hele-shaw flows. *Physical Review E*, 87:053015.
- Dias, E. O. and Miranda, J. A. (2010). Control of radial fingering patterns: A weakly nonlinear approach. *Physical Review E*, 81(1):016312.
- Dias, E. O. and Miranda, J. A. (2013b). Wavelength selection in Hele-Shaw flows: A maximum-amplitude criterion. *Physical Review E*, 88(1):013016.
- Dias, E. O., Parisio, F., and Miranda, J. A. (2010). Suppression of viscous fluid fingering: A piecewise-constant injection process. *Physical Review E*, 82(6):067301.
- Fontana, J. V., Dias, E. O., and Miranda, J. A. (2014). Controlling and minimizing fingering instabilities in non-Newtonian fluids. *Physical Review E*, 89(1):013016.
- Foroutan-pour, K., Dutilleul, P., and Smith, D. (1999). Advances in the implementation of the box-counting method of fractal dimension estimation. *Applied Mathematics and Computation*, 105(2-3):195–210.
- Ghannam, M. and Esmail, M. (1998). Rheological properties of aqueous polyacrylamide solutions. *Journal of Applied Polymer Science*, 69(8):1587–1597.
- Gin, C. and Daripa, P. (2015). Stability results for multi-layer radial hele-shaw and porous media flows. *Physics of Fluids*, 27:012101.

- Gorell, S. and Homsy, G. M. (1983). A theory of optimal policy of oil recovery by secondary displacement processes. *SIAM Journal on Applied Mathematics*, 43:79–98.
- Gun, W. J. and Routh, A. F. (2013). Microcapsule flow behaviour in porous media. *Chemical Engineering Science*, 102:309–314.
- Han, M. and Shi, L., Ye, M., and Ma, J. (1995). Crosslinking reaction of polyacrylamide with chromium(III). *Polymer Bulletin*, 35:109–113.
- Hele-Shaw, H. (1898). On the motion of a viscous fluid between two parallel plates. *Nature*, 58:34–36.
- Hill, S. (1952). Channeling in packed columns. *Chemical Engineering Science*, 1(6):247–253.
- Homsy, G. (1987). Viscous Fingering in Porous Media. *Annual Review of Fluid Mechanics*, 19:271–311.
- Huang, Y. S. and Chen, C. Y. (2015). A numerical study on radial Hele-Shaw flow: influence of fluid miscibility and injection scheme. *Computational Mechanics*, 55(2):407–420.
- Jha, B., Cueto-Felgueroso, L., and Juanes, R. (2011). Fluid Mixing from Viscous Fingering. *Physical Review Letters*, 106(19):194502.
- Kamal, M. S., Sultan, A. S., Al-Mubaiyedh, U. A., and Hussein, I. A. (2015). Review on Polymer Flooding: Rheology, Adsorption, Stability, and Field Applications of Various Polymer Systems. *Polymer Reviews*, 55(3):491–530.
- Kim, H., Funada, T., Joseph, D. D., and Homsy, G. M. (2009). Viscous potential flow analysis of radial fingering in a Hele-Shaw cell. *Physics of Fluids*, 21(7):074106.
- Korteweg, D. (1901). Sur La Forme Que Prennent Les Équations Du Mouvements Des Fluides Si L’on Tient Compte Des Forces Capillaires Causées Par Des Variations De Densité Considérables Mais Continues Et Sur La Théorie De La Capillarité Dans L’hypothèse D’une Variation Continue De La Densité. *Archives Néerlandaises des Sciences Exactes et Naturelles*, 6.
- Kuijpers, K. R., De Martín, L., and Van Ommen, J. R. (2014). Optimizing off-lattice Diffusion-Limited Aggregation. *Computer Physics Communications*, 185(3):841–846.
- Lajeunesse, E. and Couder, Y. (2000). On the tip-splitting instability of viscous fingers. *Journal of Fluid Mechanics*, 419:125–149.
- Lake, L. (1989). *Enhanced Oil Recovery*. Prentice Hall, Englewood Cliffs, NJ.
- Lee, K. E., Morad, N., Teng, T. T., and Poh, B. T. (2012). Kinetics and In Situ Rheological Behavior of Acrylamide Redox Polymerization. *Journal of Dispersion Science and Technology*, 33(3):387–395.

- Li, S., Lowengrub, J., Fontana, J., and Palfy-Muhoray, P. (2009). Control of Viscous Fingering Patterns in a Radial Hele-Shaw Cell. *Physical Review Letters*, 102:174501.
- Li, S., Lowengrub, J. S., and Leo, P. H. (2007). A rescaling scheme with application to the long-time simulation of viscous fingering in a Hele-Shaw cell. *Journal of Computational Physics*, 225(1):554–567.
- Lubkin, S. and Murray, J. (1995). A mechanism for early branching in lung morphogenesis. *Journal of Mathematical Biology*, 34(1):77–94.
- Makadia, H. K. and Siegel, S. J. (2011). Poly Lactic-co-Glycolic Acid (PLGA) as biodegradable controlled drug delivery carrier. *Polymers*, 3(3):1377–1397.
- Martyushev, L. M., Birzina, A. I., Konovalov, M., and Sergeev, A. (2015). Morphological stability of an interface between two non-Newtonian fluids moving in a Hele-Shaw cell. *Physical Review E*, 80:066306.
- Mathiesen, J., Procaccia, I., Swinney, H. L., and Thrasher, M. (2006). The universality class of diffusion-limited aggregation and viscous fingering. *Europhysics Letters (EPL)*, 76(2):257–263.
- Maxworthy, T. (1989). Experimental study of interface instability in a Hele-Shaw cell. *Physical Review A*, 39(11):5863–5866.
- May, S. E. and Maher, J. V. (1989). Fractal dimension of radial fingering patterns. *Physical Review A*, 40(3):1723–1726.
- McBirney, A. R. (1984). *Igneous Petrology*. Freeman, Cooper and Co., San Francisco.
- McCloud, K. V. and Maher, J. V. (1995). Experimental perturbations to Saffman-Taylor flow. *Physics Reports*, 260(3):139–185.
- Meakin, P. (1998). *Fractals, Scaling and Growth Far from Equilibrium*. Cambridge University Press, Cambridge.
- Miranda, J. A. and Widom, M. (1998). Radial fingering in a hele-shaw cell: a weakly nonlinear analysis. *Physica D: Nonlinear Phenomena*, 120:315–328.
- Mora, S. and Manna, M. (2009). Saffman-Taylor instability for generalized Newtonian fluids. *Physical Review E*, 80(1):016308.
- Mungan, N. (1971). Improved waterflooding through mobility control. *The Canadian Journal of Chemical Engineering*, 49(1):32–37.
- Nayfeh, A. H. (1972). Stability of liquid interfaces in porous media. *Physics of Fluids*, 15:1751–1754.
- Ossadnik, P. (1991). Multiscaling analysis of large-scale off-lattice dla. *Physica A: Statistical Mechanics and its Applications*, 176(3):454 – 462.
- Paraskeva, C. A., Charalambous, P. C., Stokka, L. E., Klepetsanis, P. G., Koutsoukos, P. G., Read, P., Ostvold, T., and Payatakes, A. C. (2000). Sandbed Consolidation with Mineral Precipitation. *Journal of Colloid and Interface Science*, 232:326–339.

- Parisio, F., Moraes, F., Miranda, J. A., and Widom, M. (2001). Saffman-Taylor problem on a sphere. *Physical Review E*, 63:036307.
- Park, C. and Homsy, G. (1984). Two-phase displacement in Hele Shaw cells : theory. *Journal of Fluid Mechanics*, 139:291–308.
- Paterson, L. (1981). Radial fingering in a Hele Shaw cell. *Journal of Fluid Mechanics*, 113:513–539.
- Paterson, L. (1985). Fingering with miscible fluids in a Hele Shaw cell. *Physics of Fluids*, 28(1):26–30.
- Perkins, T. and Johnston, O. (1969). A Study of Immiscible Fingering in Linear Models. *Society of Petroleum Engineers Journal*, 9(1):39–46.
- Pihler-Puzović, D., Illien, P., Heil, M., and Juel, A. (2012). Suppression of Complex Fingerlike Patterns at the Interface between Air and a Viscous Fluid by Elastic Membranes. *Physical Review Letters*, 108(7):074502.
- Pojman, J. A., Whitmore, C., Liria, M., Liveri, T., Lombardo, R., Marszalek, J., Parker, R., and Zoltowski, B. (2006). Evidence for the Existence of an Effective Interfacial Tension between Miscible Fluids : Isobutyric Acid-Water and 1-Butanol-Water in a Spinning-Drop Tensiometer. *Langmuir*, 22(6):2569–2577.
- Praud, O. and Swinney, H. L. (2005). Fractal dimension and unscreened angles measured for radial viscous fingering. *Physical Review E*, 72(1):011406.
- Saffman, P. G. and Taylor, G. I. (1958). The penetration of a fluid into a porous medium or hele-shaw cell containing a more viscous liquid. *Journal of Fluid Mechanics*, 245:312–329.
- Sorbie, K. (1991). *Polymer-Improved Oil Recovery*. CRC Press, Boca Raton, Florida.
- Talaghat, M. R., Esmailzadeh, F., and Mowla, D. (2009). Sand production control by chemical consolidation. *Journal of Petroleum Science and Engineering*, 67(1-2):34–40.
- Tanveer, S. (1987). Analytic theory for the linear stability of the Saffman–Taylor finger. *Physics of Fluids*, 30(8):2318–2329.
- Thomé, H., Rabaud, M., Hakim, V., and Couder, Y. (1989). The Saffman–Taylor instability: From the linear to the circular geometry. *Physics of Fluids A*, 1(2):224–240.
- Tran-viet, A., Routh, A., and Woods, A. (2014). Control of the Permeability of a Porous Media Using a Thermally Sensitive Polymer. *American Institute of Chemical Engineers*, 60(3):1193–1201.
- Wilson, S. D. R. (1990). The Taylor-Saffman problem for a non-Newtonian liquid. *Journal of Fluid Mechanics*, 220:413–425.
- Witten, T. and Sander, L. (1981). Diffusion-Limited Aggregation, a Kinetic Critical Phenomenon. *Physical Review Letters*, 47(19):1400–1403.

-
- Woods, A. W. (2015). *Flow in Porous Media*. Cambridge University Press, Cambridge.
- Woods, A. W. and Mingotti, N. (2016). Topographic viscous fingering : fluid – fluid displacement in a channel of non-uniform gap width. *Philosophical Transactions of the Royal Society A*, 374:20150427.
- Zheng, Z., Kim, H., and Stone, H. A. (2015). Controlling Viscous Fingering Using Time-Dependent Strategies. *Physical Review Letters*, 115(17):174501.